

An Abstract of the Dissertation of

Eric Antonissen for the degree of Doctor of Philosophy in Oceanography
presented on October 1, 1999.

Title: On the Evolution of the Western Equatorial Pacific Warm Pool
during the TOGA COARE IOP

Redacted for privacy

Abstract approved: _____

Adriana Huyer

Upper ocean temperature and salinity variability in the western equatorial Pacific warm pool has been the subject of considerable study because it is linked to important climate phenomena, e.g. El Niño-Southern Oscillation (ENSO) events. In this work, the evolution of the upper ocean in the western equatorial Pacific warm pool at 1.75°S, 156.0°E is investigated for the three ~20-day R/V Wecoma survey cruises made during the TOGA COARE IOP, Nov 1992 - Feb 1993. Three ocean layers are considered: the surface mixed layer (SML) in which density is within 0.01 kg m^{-3} of the surface density, a 50 m fixed depth layer, and the upper ocean layer (UOL) between the sea surface and the $\sigma_{\theta} = 22.0 \text{ kg m}^{-3}$ isopycnal. The average depths of the SML and UOL were 25 m and 77 m, respectively.

Episodes of sustained winds are important in predicting ocean heat and salt variability because the combination of strong currents together with even modest lateral gradients can result in sizable advective fluxes. On the second survey cruise, the near-equatorial oceanic response to a sustained westerly wind event generated strong meridional cooling that was somewhat compensated by warming associated with moderate to

was somewhat compensated by warming associated with moderate to strong equatorial downwelling of 10 to 20 m day⁻¹. Subsurface shear driven turbulence at ~2.1°S appears to be the genesis of at least one of the meridional fronts. Advection was the dominant term in the 50 m and UOL layer heat and salt budgets for this period.

The three cruise average heat advection estimates were not significantly different from zero. Salt advection, however, appears to be important in maintaining the warm pool salinity and suggests that ocean circulation is likely important in the long term budget. A somewhat surprising result was that the penetration of radiant energy below the base of the SML averaged -52 Wm⁻² and was the dominant flux term in the SML heat budget. For this same period, the net surface and turbulent heat fluxes averaged 14 Wm⁻² and -11 Wm⁻², respectively.

©Copyright by Eric Antonissen
October 1, 1999
All Rights Reserved

On the Evolution of the Western Equatorial Pacific Warm Pool during the
TOGA COARE IOP

by

Eric Antonissen

A Dissertation Submitted to

Oregon State University

In partial fulfillment of

the requirements for the degree of

Doctor of Philosophy

Completed October 1, 1999

Commencement June 2000

Doctor of Philosophy Dissertation of Eric Antonissen presented on October 1, 1999

Approved:

Redacted for privacy

Major Professor, representing Oceanography

Redacted for privacy

Dean of College of Oceanic and Atmospheric Sciences

Redacted for privacy

Dean of Graduate School

I understand that my dissertation will become part of the permanent collection of Oregon State University libraries. My signature below authorizes release of my dissertation to any reader upon request.

Redacted for privacy

Eric Antonissen, Author

Acknowledgments

I want to thank my thesis advisor, Professor Adriana (Jane) Huyer, for supporting and carefully reviewing my work and for graciously allowing me time off to assist my family during my father's medical crisis. I also greatly appreciate the courtesy that Jane has extended to me while working on my thesis in absentia from Oregon State University. I have benefited tremendously from the fact that she is a very careful and exacting scientist who demands as much from others as she does from herself.

I am indebted to Professor Steve Esbensen for providing valuable and thoughtful insights, timely feedback, and encouragement to consider the "bigger picture". I appreciate the assistance and support of Dr. Mike Kosro, Professor Roland Deszoeke, Professor Bob Miller, Professor Jim Moum, Professor Clayton Paulson, and Dr. Bill Smyth throughout the course of this work. I also would like to thank my graduate school representative, Civil Engineering Department Chairman Professor Wayne Huber, for his assistance and support. I would also like to recognize the numerous faculty members from the College of Oceanic and Atmospheric Sciences, the Department of Physics, and Professor Dave Bella from the Department of Civil Engineering who helped shape my personal and professional perspective.

I could not have completed this work without the friendship, dedication, and expertise of Bob O'Malley and Jane Fleischbein and it has been a pleasure to work with them. They have done an incredible job of working up the COARE Seasoar CTD data, the essential data for much of my work. I will always cherish the support and understanding they have given me and it is my hope that in return I have been as good a friend and co-worker to them. I deeply appreciate the friendship and support of

Table of Contents

	<u>Page</u>
1. General Introduction	1
2. On the Evolution of the Western Equatorial Pacific Warm Pool during the TOGA COARE IOP: Advection of Heat and Salt	6
2.1 Abstract	6
2.2 Introduction	7
2.3 Observations	12
2.3.1 Seasoar observations	12
2.3.2 R/V Moana Wave CTD data	16
2.3.3 Surface heat fluxes, rainfall, and winds	16
2.3.4 UOP mooring current data	18
2.3.5 Currents at surrounding platforms	19
2.4 Analytical Methods	20
2.4.1 Depths of integration	20
2.4.2 Construction of horizontal temperature and salinity gradients	23
2.4.3 Construction of vertical temperature and salinity gradients	26
2.4.4. Horizontal flow field	27
2.4.5. Vertical velocity	37
2.4.6 Horizontal and vertical advection	46
2.5 Advection Estimates of Heat and Salt	54
2.5.1 W9211A: 14 to 30 November, 1992	54
2.5.2 W9211B: 21 December 1992 to 8 January, 1993	61
2.5.3 W9211C: 28 January to 14 February, 1993	64
2.5.4 Overall advection means for the IOP surveys	67
2.6 Discussion/Conclusions	69

Table of Contents (continued)

	<u>Page</u>
4 General Conclusions	134
Bibliography	139
Appendices	147

List of Figures

<u>Figure</u>		<u>Page</u>
2.1.a	The location of the TOGA COARE sampling domain showing location of islands and principal stationary ships (reproduced from the TCIPPO Operations Summary, 1993).	13
2.1.b	An expanded view of the center of the Intensive Flux Array, showing the butterfly pattern sampled repeatedly by Wecoma and the location of the stationary platforms used in this study:	14
2.2	Time series of wind stress, rainfall, surface layer depths, and upper ocean currents at the center of the IFA.	22
2.3	Time series of hourly SML depth estimated from R/V Moana Wave (solid line) and Seasoar (triangles) at the butterfly intersection (top), and at all Seasoar grid points (second row).	24
2.4	Time series of hourly UOL depth estimated from R/V Moana Wave (solid line) and Seasoar (triangles) at the butterfly intersection (top), and at all Seasoar grid points (second row).	25
2.5	Meridional temperature profiles with 130-km regression lines, at nominal bin depths of 9 m and 50 m for W9211B.	30
2.6.	Large-scale (130 km) gradients of temperature and salinity, in units of °C/100 km and psu/100 km respectively, as a function of time and depth (m).	31
2.7	Significance level of the slope of the 130 km regression line.	32
2.8	Time-depth distributions of the 95% bootstrap error estimates for the 130 km regression fits.	33
2.9	Low passed (32 hr) temperature and salinity distributions with SML and UOL depths superimposed.	34
2.10	Low passed (32 hour) zonal currents from PCM-N, UOP, S2, R/V Xiangyanghong #5, and R/V Shiyan #3.	35

List of Figures (Continued)

<u>Figure</u>	<u>Page</u>
2.11 Low passed (32 hour) meridional currents from PCM-N, UOP, S2, R/V Xiangyanghong #5, and the R/V Shiyan #3.	36
2.12a Squared correlation coefficients for zonal currents from 32 hour filtered data.	39
2.12b Squared correlation coefficients for meridional currents from 32 hour filtered data.	40
2.13a Orientation, magnitude, and the percent variance explained by each of the first four modes (EOF1-4) of the Complex Empirical Orthogonal Function eigenvectors at 40, 50, 60, and 70 m for each of the current platform sites for W9211A.	41
2.13b Orientation, magnitude, and the percent variance explained by each of the first four modes (EOF1-4) of the Complex Empirical Orthogonal Function eigenvectors at 40, 50, 60, and 70 m for each of the current platform sites for W9211B.	42
2.13c Orientation, magnitude, and the percent variance explained by each of the first four modes (EOF1-4) of the Complex Empirical Orthogonal Function eigenvectors at 40, 50, 60, and 70 m for each of the current platform sites for W9211C.	42
2.14 Time and depth distributions of vertical velocity (w), meridional divergence ($\partial v / \partial y$) between PCM-N and S2, and the zonal divergence ($\partial u / \partial x$) between Shiyan 3 and Xiangyanghong #5.	44
2.15a Time series of vertical velocity at the base of the UOL estimated from divergence and from the time derivative of the 32 hour low passed UOL depth, i.e. $-\partial h / \partial t$ (solid line).	48
2.15b Average vertical velocity profiles.	49
2.16 Vertical distributions of horizontal heat advection per unit depth (Wm^{-3}) and its error, both estimated from the large scale gradients, with SML and UOL depths superimposed.	50

List of Figures (Continued)

<u>Figure</u>		<u>Page</u>
2.17	Vertical distributions of meridional and zonal heat advection per unit depth (Wm^{-3}), estimated from large scale gradients, with SML and UOL depths superimposed.	51
2.18	Vertical distributions of horizontal salt advection per unit depth ($psu\ hr^{-1}\ m^{-2}$) and its error, both estimated from the large scale gradients, with SML and UOL depths superimposed.	52
2.19	Vertical distributions of meridional and zonal salt advection per unit depth ($psu\ hr^{-1}\ m^{-2}$), estimated from large scale gradients, with SML and UOL depths superimposed.	53
2.20	Vertical heat advection time series for the 50 m layer and UOL.	57
2.21	Vertical salt advection time series for the 50 m layer and UOL.	58
2.22	Time Series of Seasoar SST (0-2 m) from 1 sec data, upper 50 m heat content ($\int \rho c_p T dz$), Seasoar SSS (0-2 m) time series, and upper 50 m layer average salinity, ($1/50m \int S dz$).	59
3.1a	The location of the TOGA COARE sampling domain showing location of islands and principal stationary ships (reproduced from the TCIPPO Operations Summary, 1993).	80
3.1.b	An expanded view of the center of the Intensive Flux Array, showing the butterfly pattern sampled repeatedly by R/V Wecoma and the location of the stationary platforms used in this study:	81
3.2	Time series of wind stress, rainfall, SML depth, UOL depth, SML. 50 m layer, and UOL temperature and salinity.	84
3.3	Hourly 50 m layer temperature (upper panels) and salinity (lower panels) from the R/V Wecoma (squares) and R/V Moana Wave (solid black).	85
3.4a	Time-latitude and time-longitude plots of the 50 m layer salinity from Wecoma for W9211A.	86

List of Figures (Continued)

<u>Figure</u>		<u>Page</u>
3.4b	Time-latitude and time-longitude plots of the 50 m layer salinity from Wecoma for W9211B.	87
3.4c	Time-latitude and time-longitude plots of the 50 m layer salinity from Wecoma for W9211C.	88
3.5	Hourly averaged surface heat fluxes from UOP mooring.	95
3.6	The 50 m layer heat budget:	107
3.7	The 50 m layer salt budget in terms of equivalent freshwater fluxes.	108
3.8	Frequency dependence of heat and salt storage for the SML during W9211A.	110
3.9	Frequency dependence of heat and salt storage for the SML during W9211B.	118
3.10	Meridional section distributions of Richardson number and shear squared (contours in units of 10^{-4} s^{-2}) estimated from Wecoma Seasoar density and ADCP data.	119
3.11a	Meridional section distributions of temperature estimated from Wecoma Seasoar data.	120
3.11b	Meridional section distributions of salinity estimated from Wecoma Seasoar data.	121
3.12	Frequency dependence of heat and salt storage for the SML during W9211C.	126

List of Tables

<u>Table</u>	<u>Page</u>
2.1 UOP mooring average heat fluxes, accumulated rainfall, and, rainfall-evaporation (P-E).	17
2.2 Average properties of surface layers: depth, layer interface temperature (T_h) and layer interface salinity (S_h).	29
2.3 Average heat advection (Wm^{-2}).	55
2.4 Cumulative freshwater advection (cm)	56
3.1 Surface heat flux comparisons between each platform and for each component of the surface flux	93
3.2 Comparison of the surface freshwater flux comparisons from each platform.	94
3.3.a SML heat storage rate: time difference vs. spectral approach.	102
3.3.b Freshwater storage rate: time difference vs. spectral approach (accumulation in cm).	102
3.4 Heat budget results (Wm^{-2}):	105
3.5 Freshwater budget results (cm):	106
3.6 Layer averages: depth, salinity, temperature	109

List of Appendices

<u>Appendix</u>		<u>Page</u>
A	Bootstrap Statistics	148
B	Advection Error Analysis	150
C	Spectral Method for Estimating Storage Terms	157
D	Heat and Salt Budget Error Analysis	162
E	Investigation of the Shipborne ADCP Direction Accuracy: Comparison of Moana Wave and WHOI UOP Mooring Current Data for the TOGA COARE IOP.	175

List of Appendix Figures

<u>Figure</u>	<u>Page</u>
D1. Summary heat budget box plot for W9211A.	167
D2. Summary heat budget box plot for W9211B.	168
D3. Summary heat budget box plot for W9211C.	169
D4. Summary heat budget box plot for three-cruise average.	170
D5. Summary freshwater budget box plot for W9211A	171
D6. Summary freshwater budget box plot for W9211A	172
D7. Summary freshwater budget box plot for W9211A	173
D8. Summary freshwater budget box plot for three-cruise average.	174
E1. Profiles of average zonal (U) and meridional (V) currents from the UOP mooring (solid) and the R/V Moana Wave (dashed).	188
E2. Profiles of average zonal differences (Delta U) and meridional differences (Delta V) for unrotated (upper panels) and rotated (lower panels) current vector components.	189

List of Appendix Tables

<u>Table</u>	<u>Page</u>
E1. Leg 1 moored ADCP/Ship ADCP correlation	190
E2. Leg 2 moored ADCP/Ship ADCP correlation	190
E3. Leg 1 moored VMCM/Ship ADCP correlation	191
E4. Leg 2 moored VMCM/Ship ADCP correlation	191

Dedication

To my mother and to the memory of my father.

On the Evolution of the Western Equatorial Pacific Warm Pool during the TOGA COARE IOP

Chapter 1

General Introduction

Catastrophic changes in global weather and ocean conditions associated with the El Niño Southern Oscillation (ENSO) cycle has focused substantial scientific effort to better understand the interaction between the sea surface temperature (SST) response of the western equatorial Pacific warm pool and changes in the tropical ocean and global atmosphere. The connection of warm pool SST variability to equatorial ocean conditions and global weather patterns has been recognized for almost three decades (Bjerknes, 1966; Bjerknes, 1969; Horel and Wallace, 1981; Rasmusson and Carpenter, 1983) and provided motivation for the Tropical Ocean-Global Atmosphere (TOGA, 1985-1995) research program. In particular, TOGA was designed to better understand the coupled ocean-atmosphere system of the western equatorial Pacific warm pool and the work presented in this dissertation represents a small contribution to that effort.

TOGA was intended to provide observational and modeling studies of the equatorial Pacific ocean and atmosphere with the goal of establishing an operational ENSO forecast system (Webster and Lukas, 1992). Considerable effort has been made to predict ENSO events but prognostic models of ENSO have been only modestly successful and have not demonstrated much improved predictive skill from an early model of Zebiak and Cane (1987). One reason why model simulations achieve only moderate success may be because reliable simulation of the heat exchange

processes has been difficult to verify due to large uncertainties in the fluxes (Webster and Lukas, 1992). To address this issue a Coupled Ocean-Atmosphere Response Experiment (COARE) was conducted, under the auspices of the TOGA program, to obtain oceanic and atmospheric observations over a two-year period (1992-1994). Included in COARE was an Intensive Observing Period (IOP) conducted from November 1992 to February 1993 by the international scientific community and involved numerous ships, aircraft, and other oceanographic and atmospheric instrumentation. The IOP was designed to make observations of the ocean and atmosphere from centimeter scale ocean microstructure measurements to ~ 1000 km scale atmospheric observations in a relatively simultaneous fashion (TCIPO, TOGA Ops. Summary, 1993). By design, the observations made during the IOP provide an opportunity to make good estimates of all of the terms in the heat and salt budgets over time scales of days to months and over spatial scales of tens to hundreds of kilometers.

Heat and freshwater budgets for three different upper ocean surface layers centered at 1.75°S , 156.0°E and spanning a spatial extent of ~ 100 km and a temporal scale of days to months are presented in this dissertation. The three ocean layers considered are the surface mixed layer (SML) defined by a density difference threshold of 0.01 kg m^{-3} (Moum et al., 1989; Brainerd and Gregg, 1994), a 50 m fixed depth layer, and an upper ocean layer above the 22.0 kg m^{-3} isopycnal (Smyth et al., 1996a). The SML is an active turbulent region of the upper ocean that readily responds to surface forcing. Feng et al. (1998) found remarkably good closure of heat and salt budget budgets for the 50 m and UOL layers (within 10 Wm^{-2} for the heat budgets) for a time period considered within this study using much of the same data. The essentially concurrent study reported here uses significantly different analytical methods for estimating the advective

terms and the rate of change in the storage of heat and salt for variable depth layers. This work, in part, provides some verification of the results of Feng et al. (1998) but the budget analysis is extended here to include the SML which is fundamental to understanding the processes that regulate SST and mediate the air-sea coupling. Our aim is to contribute to a better understanding of the warm pool heat and salt response and to the development of improved modeling capability of the western equatorial Pacific warm pool.

Chapter 2 presents direct estimates of the oceanic advective fluxes in the context of the oceanic and atmospheric forcing for each of the three R/V Wecoma survey cruises completed during the IOP. The advection term is often treated as a residual in ocean budget studies because its direct estimation is usually not possible from the available observations (Wijesekera and Gregg, 1996; Smyth et al., 1996a,b). If there are no errors in the other terms of the budget and the observations are spatially representative then the budget residual approach for estimating advection may be successful. The drawback of this approach, however, is that it does not resolve advective processes, i.e. vertical vs. horizontal; furthermore estimated surface and turbulent fluxes as well as the rate of change in heat or freshwater storage can have substantial uncertainties so that measurement error may incorrectly be attributed to advection. In this work, horizontal advection is estimated using upper ocean currents measured by the Upper Ocean Processes (UOP, Plueddemann, 1993) mooring and horizontal temperature and salinity gradients estimated from repeated meridional and zonal Seasoar CTD transects by R/V Wecoma. The mooring was centrally located near the intersection of the Wecoma transect lines. Vertical velocity was calculated from horizontal flow divergence from an array of ship and moored current observations using

simple Fourier filtering and, with a second approach, using complex Empirical Orthogonal Functions (EOFs) following Kundu and Allen (1976) to extract the coherent part of the flow field over the array. The vertical velocity and vertical gradients of temperature and salinity were integrated over each layer depth to estimate vertical advection.

In chapter 3, closure of the heat and freshwater budgets is attempted. Given the high frequency variability of the temperature, salinity, and layer depths the rate of change in heat and freshwater storage for the SML is calculated in two ways: in the time domain using conventional centered differences in time and in the spectral domain using an autocorrelation relation. One motivation for using the spectral approach is to overcome the inaccuracy of discrete time derivatives that occurs when the scale of temporal variability in the time series is comparable to the sampling time scale (Haltiner and Williams, 1982). The spectral approach gives a more accurate estimate when the data are relatively "noisy" but stationary and the temporal approach gives a better estimate when the data are relatively smooth. The spectral approach also provides information about the sign of the frequency response of the storage term, i.e. whether cooling or heating occurs at a given frequency.

These budget studies attempt to assess the balance between the rate of change in heat and salt storage and the sum of the individual flux terms in the budget: the turbulent flux estimates made from ocean microstructure observations near the central mooring (Wijesekera and Gregg, 1996; Smyth et al., 1996b), surface flux observations made over the study region (Weller and Anderson, 1996; Fairall et al., 1996; Paulson, pers. comm.), estimates of the penetrative radiation (Siegel et al., 1995; Ohlmann et al., 1996), and the advection estimates from chapter 2. Penetrative radiation appears as a

cooling term in the budget because it represents the fraction of incident surface radiant heat that penetrates through the base of the layer of interest.

The results of the heat budget studies indicate that for the SML, penetrative radiation is the dominant flux and acts to limit the heating rate. In other words, if the water was more opaque to incident radiant energy then the SST would be higher than what is observed provided the other forcing conditions remained unchanged. For the 50 m layer, advection, surface, and penetrative fluxes are almost equally important for the long term average but on less than one month time scales individual flux terms, such as the surface flux or advection, may dominate the budget. For the UOL, horizontal and vertical advection were often the dominant terms but tended to offset each other.

Heat advection was found to be an important component of the upper ocean budgets during and just following strong wind events. During and following a strong westerly wind event in December and January, Ekman layer dynamics associated with the northward turning of the Yoshida Jet were a dominant component of the flow field and advective response. The three-cruise average of heat advection in the SML, however, was not different than zero. Meridional heat advection generally had a larger magnitude and opposite sign to the zonal and vertical components. Salt advection was significant in the SML and 50 m layer and appears to be important in maintaining the warm pool salinity given that annual precipitation for the region exceeds evaporation by ~ 2 m (Philander, 1990). These findings suggest that ocean circulation (transport) may need to be well represented in model simulations of the warm pool thermohaline response.

Chapter 2

On the Evolution of the Western Equatorial Pacific Warm Pool during the TOGA COARE IOP: Advection of Heat and Salt

2.1 Abstract

Estimates of heat and salt advection in the upper ocean at 1.75°S, 156.0°E are presented for three ~20-day periods (14 to 30 Nov, 1992; 21 Dec to 8 Jan, 1993; 28 Jan to 14 Feb, 1993) during the TOGA COARE IOP, Nov 1992 - Feb 1993. We focus on the role of advection in modifying the heat and salt content on time scales of days to months and spatial scales of ~100 km. The study region was near the center of the western equatorial Pacific warm pool which has been noted for its role in El Niño-Southern Oscillation (ENSO) events. Heat and salt advection estimates are presented for three surface layers: the surface mixed layer (SML) in which density is within 0.01 kg m^{-3} of the surface density, a 50 m fixed-depth layer, and the upper ocean layer (UOL) between the surface and the $\sigma_{\theta} = 22.0 \text{ kg m}^{-3}$ isopycnal. The average depths of the SML and UOL were 25 m and 77 m, respectively.

Horizontal advection was calculated by combining temperature and salinity gradients estimated from repeated zonal and meridional Seasoar CTD sections with ocean current velocity measured at the intersection point. Vertical advection was calculated using vertical thermohaline gradients estimated from CTD profiles and vertical velocity estimated from horizontal divergence over an array of moorings and stationary ships. In all three layers, episodes of horizontal heat advection of more than $\pm 100 \text{ Wm}^{-2}$ and lasting 2 to 5 days occurred. During a period of sustained

westerly winds (Dec 21 to Jan 8) the average horizontal heat flux for the 50 m layer was estimated to be $-50 \pm 13 \text{ Wm}^{-2}$; meridional advection contributed -82 Wm^{-2} , zonal heat advection averaged 32 Wm^{-2} , and vertical heat advection was estimated at 28 Wm^{-2} . The overall average horizontal advective heat flux in the SML over the three surveys was small, $-3 \pm 5 \text{ Wm}^{-2}$, in agreement with previous studies. Horizontal salt (freshwater) advection amounted to a freshwater loss of about 25 cm and 50 cm from the SML and 50 m layer, respectively. Advection appears to be a significant component of the long term warm pool salt budget and can dominate the heat budget on time scales of several days.

2.2 Introduction

Quantifying the exchange of heat, moisture, and momentum between the ocean and atmosphere in the western equatorial Pacific warm pool is necessary to understand the processes that drive the El Niño-Southern Oscillation (ENSO) cycle (WCRP, 1990, Webster and Lukas, 1992). The purpose of this study is to describe heat and salt (freshwater) advection near the center of the Intensive Flux Array (IFA, Fig. 2.1a) for the three R/V Wecoma cruises made during the Intensive Observing Period (IOP, Nov 1992 to March 1993) of the Coupled Ocean-Atmospheric Response Experiment (COARE, 1992-1994). COARE was conducted as part of the Tropical Ocean Global Atmosphere (TOGA) program and was designed to better understand the coupling of the ocean-atmosphere system of the warm pool.

During the IOP several moorings and ships were deployed in the IFA including the central Upper Ocean Processes Group (UOP; Plueddemann, 1993) mooring at 1.75°S, 156.0°E which was equipped with surface meteorological sensors and subsurface temperature, salinity, and current sensors. In this work, we present heat and salt advection estimates at ~1.75°S, 156.0°E calculated using Seasoar CTD data from a moving ship, moored current data, and stationary ship CTD and current data for three ~ 20 day cruise periods: 14 to 30 Nov, 1992; 21 Dec to 8 Jan, 1993; 28 Jan to 14 Feb, 1993. Advection estimates were made for three different surface layers: the surface mixed layer (SML); in which the density is defined to be within 0.01 kg m^{-3} of the surface density (Moum et al, 1989; Brainerd and Gregg, 1995), a 50 m fixed-depth layer, and the upper ocean layer (UOL) between the surface and the $\sigma_{\theta} = 22.0 \text{ kg m}^{-3}$ isopycnal following Smyth et al. (1996a,b).

The annual net surface heat flux into the warm pool provides an estimated heating of 20 to 80 Wm^{-2} (Esbensen and Kushnir, 1981; Reed, 1985; Weare et al., 1981) and the annual turbulent heat loss from the upper ocean into the deeper ocean provides cooling at an estimated rate of -1 to -20 Wm^{-2} (Niiler and Stevenson, 1982; Godfrey and Lindstrom, 1989; Wijesekera and Gregg, 1995; Smyth et al., 1996b). If these estimates of the surface and turbulent fluxes are reliable then advection and/or penetrative radiation may be important in balancing the local heat budget. Siegel et al. (1995) found that penetrative radiation can be $\sim -10 \text{ Wm}^{-2}$ at 50 m and the loss of radiant heat is considerably higher for the SML which tends to be much shallower than 50 m especially during peaks in the shortwave radiation, i.e. mid-day. Heat advection in the upper ocean has historically been considered to be negligible compared to the surface and turbulent heat flux in the warm pool because sea surface temperature (SST) is

relatively homogeneous and thus lateral gradients are small (Niiler and Stevenson, 1982). Is advection an important component of the warm pool heat and salt budget? If it is, over what time and space scales does it contribute, and what are the dominant advective processes? Our work focuses on determining the importance of near equatorial heat and salt advection in the upper ocean of the warm pool for the R/V Wecoma IOP surveys on time scales of days to months and over horizontal space scales of 65 km to 130 km. We estimate the advective fluxes over these horizontal scales for a vertical column near the center of the Wecoma sampling region extending from the ocean surface at $z = 0$ to a depth $z = -h$ as noted above.

The vertically integrated heat budget equation is given by,

$$\begin{aligned} \rho c_p \int_{-h}^0 \frac{\partial T}{\partial t} dz = \\ - \rho c_p \int_{-h}^0 (\bar{u} \cdot \bar{\nabla} T) dz + Q_{heat} = - \rho c_p \int_{-h}^0 \left\{ \left(u \frac{\partial T}{\partial x} + v \frac{\partial T}{\partial y} \right) + w \frac{\partial T}{\partial z} \right\} dz + Q_{heat} \end{aligned} \quad (2.1)$$

where Q_{heat} represents the sum of penetrative radiation, turbulent heat, and surface flux contributions. We have separated the horizontal and vertical advection terms to more clearly acknowledge that we have estimated these terms using different methods. The left hand side of 2.1 represents the local rate of change in heat content that must be accounted for by the various fluxes including advection. The conventional right hand coordinate system with z positive upward has been used throughout this work. Similarly for the salt budget we have,

$$\begin{aligned} \int_{-h}^0 \frac{\partial S}{\partial t} dz = \\ - \int_{-h}^0 (\bar{u} \cdot \bar{\nabla} S) dz + Q_{salt} = - \int_{-h}^0 \left\{ \left(u \frac{\partial S}{\partial x} + v \frac{\partial S}{\partial y} \right) + w \frac{\partial S}{\partial z} \right\} dz + Q_{salt} \end{aligned} \quad (2.2)$$

where Q_{salt} represents the sum of turbulent and surface salt fluxes. We have ignored the variation of density, ρ ($=10^3 \text{ kg m}^{-3}$), and the variation of the specific heat of sea water, c_p ($=4 \times 10^3 \text{ J kg}^{-1} \text{ }^\circ\text{C}^{-1}$), and we have also ignored horizontal mixing, i.e. horizontal eddy diffusion is set equal to zero. Our focus in this work is on estimating the advective contributions, over time scales of days to weeks, to the local upper ocean budgets.

The formulation of the budgets given by Eqns. 2.1 and 2.2 is consistent with Smyth et al. (1996b) but we note that other authors (Feng et al., 1998; Cronin and McPhaden, 1997) have estimated advection and attempted to close upper ocean budgets for variable depth layers for COARE. These authors used a formulation of the upper ocean budget following Stevenson and Niiler (1983) which we show below for the heat budget only;

$$\begin{aligned} \rho c_p h \frac{\partial T_a}{\partial t} = \rho c_p \left(\int_{-h}^0 \frac{\partial T}{\partial t} dz - (T_a - T_{-h}) \frac{\partial h}{\partial t} \right) = \\ - \rho c_p \left\{ h u_a \cdot \bar{\nabla} T_a + \bar{\nabla} \cdot \int_{-h}^0 \bar{u}' T' dz + (T_a - T_{-h}) \left(u_{-h} \frac{\partial h}{\partial x} + v_{-h} \frac{\partial h}{\partial y} + w_{-h} + \frac{\partial h}{\partial t} \right) \right\} + Q_{heat} \end{aligned} \quad (2.3)$$

where the subscript 'a' refers to a vertical average over a depth h and the primes correspond to deviations from the vertical average, i.e. $T = T_a + T'$. This formulation is advantageous when the budget is estimated for a layer depth that follows a material surface because the entrainment term vanishes. For such a case, adiabatic terms are removed. Note that the left hand side of this equation is not, in general, equivalent to the total time rate of change in the layer's heat storage and represents only the change in heat storage associated with the layer's depth and the time rate of change of the average temperature. The rate of change in heat storage associated with the rate of change in the layer's depth is contained within the entrainment term which may not necessarily be zero.

If the entrainment term is not zero this formulation of the budget requires including terms that are difficult to estimate well from our data; specifically the lateral advection components of the entrainment flux,

$$\rho c_p (T_a - T_{-h}) \left(u_{-h} \frac{\partial h}{\partial x} + v_{-h} \frac{\partial h}{\partial y} \right),$$

and the divergence of the vertically averaged product of the vertically sheared velocity and vertically varying

temperature, $\vec{\nabla} \bullet \int_{-h}^0 (\vec{u}' T') dz$. Stevenson and Niiler (1983) considered an

upper ocean budget down to the depth of a material surface to remove adiabatic contributions by exploiting the fact that the entrainment flux is identically zero for a material surface and assumed that the divergence term involving \vec{u}' and T' above was small. In our study, the base of the SML and UOL are not strictly valid material surfaces though the base of the UOL may sometimes be a fairly good approximation.

For the SML, the vertical deviations of temperature are small, $< 0.03^\circ\text{C}$, and the advection terms in (2.1) and (2.3) become approximately

equivalent for the SML, $\int_{-h}^0 (\vec{u} \bullet \vec{\nabla} T) dz \approx h \vec{u}_a \bullet \vec{\nabla} T_a$. This is not the case for

the UOL and we are unable to accurately estimate the lateral variation of the UOL base due to tidal and other short-term fluctuations. The term representing the divergence of the product of the vertical variations in the

current and temperature in Eqn 2.3, i.e. $\vec{\nabla} \bullet \int_{-h}^0 (\vec{u}' T') dz$, is difficult to

accurately evaluate from our data and the gradient of the vertically integrated product will not, in general, be amenable to a simple linear estimator. Note that this term is a consequence of the formulation of the advective terms in (2.3) and is present in (2.1) but in a more direct way. Specifically, in our analysis we estimate the advection per unit depth,

which includes the vertical variation of \bar{u} and $\bar{\nabla}T$, and then compute the vertical integral over a depth h . The entrainment flux implicit in (2.1) and (2.2) is the result of the competing effects of turbulent mixing, penetrative radiation, vertical velocity, and the lateral advection of the layer depth; all of which must be considered when attempting to close the budget. In this paper (i.e. chapter 2), however, we will focus only on the advective response given by Equations (2.1) and (2.2) and defer discussion of the complete budget to a companion paper (i.e. chapter 3).

The remainder of this paper is organized as follows. In section 2 we summarize the observations used in our analysis. In section 3 we discuss the analytical methods used for calculating the horizontal and vertical advective fluxes. Section 4 summarizes the advection estimates for each Wecoma cruise and the three cruise average results. Section 5 contains a discussion and summary of our findings. Appendix A provides a review of bootstrap statistics and Appendix B details the error analysis for the advection estimate.

2.3 Observations

2.3.1 *Seasoar observations*

The R/V Wecoma sampled the upper ocean temperature and salinity fields in the IFA during the following periods (W9211A,B,C):

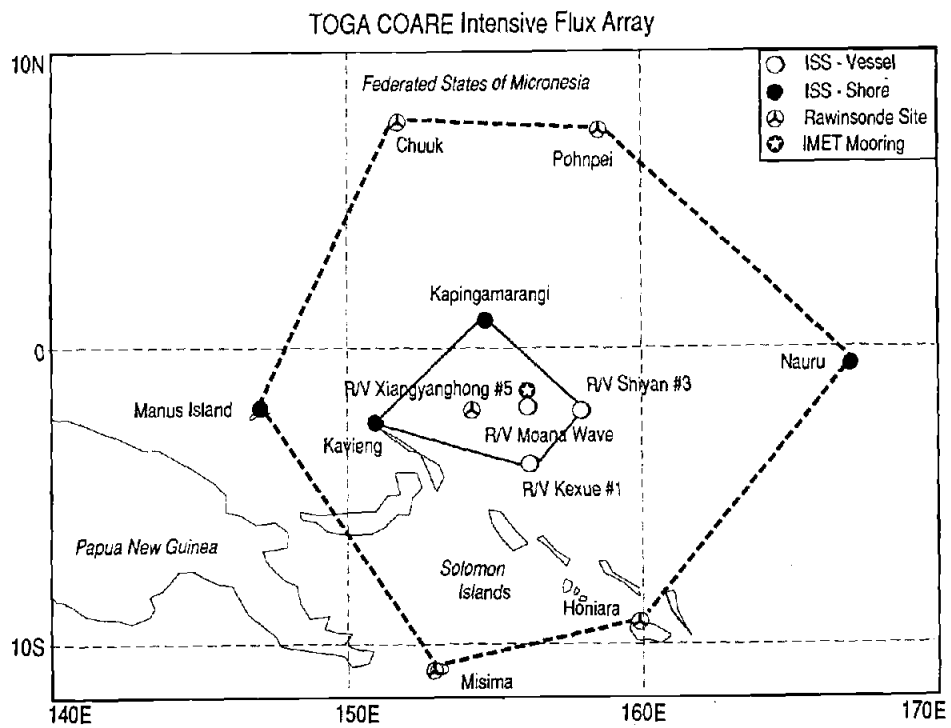


Figure 2.1a The location of the TOGA COARE sampling domain showing the location of islands and principal stationary ships (reproduced from the TCIP0 Operations Summary, 1993).

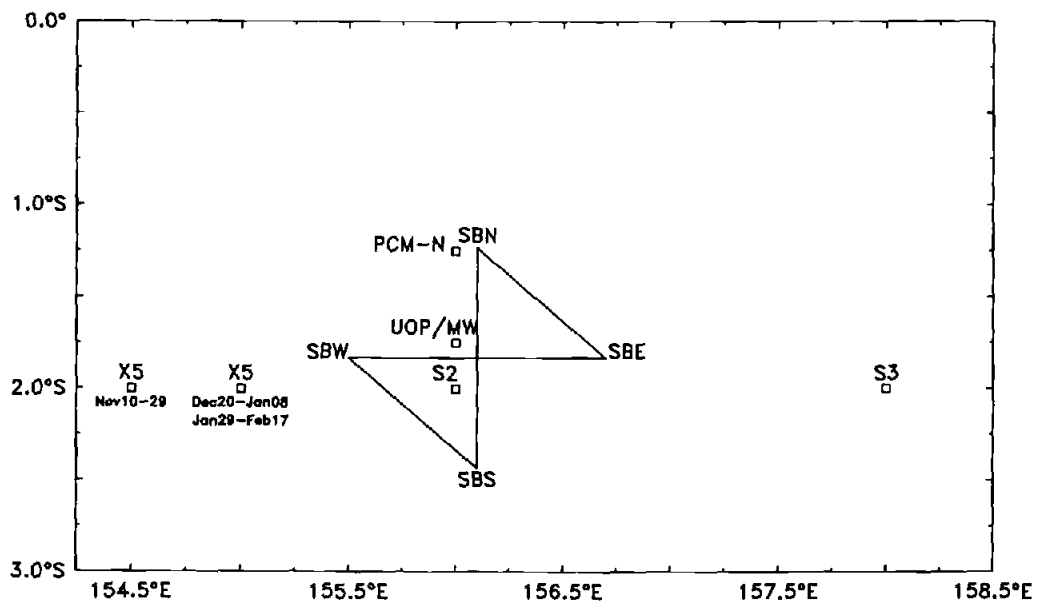


Figure 2.1b An expanded view of the center of the Intensive Flux Array, showing the butterfly pattern sampled repeatedly by R/V Wecoma and the location of the stationary platforms used in this study: UOP mooring, Profiling Current Meter mooring (PCM-N), the S2 mooring, R/V Moana Wave (MW), R/V Xiangyanghong#5 (X5), and R/V Shiyan#3 (S3).

13 Nov to 2 Dec 1992, 19 Dec 1992 to 10 Jan 1993, and 27 Jan to 15 Feb 1993 (Huyer et al., 1997). On each cruise, we used a towed undulating Seasoar system to sample the upper ocean thermohaline structure as continuously as possible along a simple butterfly pattern (Fig. 2.1b) with zonal and meridional sections extending 72 nautical miles (130 km). The usual tow speed was 7-8 knots (4 m s^{-1}) so that each meridional and zonal transect of the butterfly pattern was completed in ~ 10 hours and, when Seasoar operations were not interrupted, the entire pattern was completed in ~ 32 hours. The usual depth range was 0 to 280 m and the usual cycling period was 8-10 minutes. Seabird temperature and conductivity cells were mounted in the nose cone of the Seasoar vehicle and seawater was pumped through the cells from external ducts. A Seabird 9/11 CTD located in the interior of Seasoar transmitted raw 24 Hz conductivity, temperature, and pressure data to computers onboard ship. The raw data were merged with GPS time and position data and archived. The data were subsequently reprocessed as described in a series of data reports (Huyer et al., 1993; O'Malley et al., 1993; Huyer et al., 1994). The final processed Seasoar CTD data set consists of 1-sec averages of temperature and salinity; these data have a horizontal resolution of < 3 km and a vertical resolution of ~ 2 dbar. The temperature, salinity and pressure accuracy are estimated to be $\pm 0.01^\circ\text{C}$, ± 0.01 psu and ± 1 dbar, respectively (Huyer et al., 1993). Some partial Seasoar sections were completed using conventional CTD casts separated by 10 km (Huyer et al., 1997). For estimating layer depths and the heat/salt storage the temperature, salinity, and density data were gridded into hourly 4 m bins in the vertical. For the horizontal gradient calculations, we gridded the 1-sec temperature and salinity data along the

cardinal transects into 2 nm (~ 4 km) horizontal and nominally 8 m vertical bins using a triangular filter in the vertical with a 16 m base.

2.3.2 R/V Moana Wave CTD data

Three R/V Moana Wave cruises coincided approximately with the R/V Wecoma survey cruises. During the first two cruises (6 Nov to 6 Dec 1992; 17 Dec 1992 - 11 Jan 1993) Moana Wave remained within 10 km of the UOP mooring (Fig. 2.1b) while sampling the upper ocean thermohaline structure at 3 to 6 times per hour. On the third cruise sampling was much less frequent (4 - 5 times per day), and the ship remained near the UOP mooring only from 29 Jan to 5 Feb 1993. On the first Moana Wave cruise, the Advanced Microstructure Profiler (AMP) was used to measure the upper ocean temperature and salinity from 2.0 - 225 m (Wijesekera and Gregg, 1996). On the second cruise CHAMELEON was used to measure temperature and salinity from ~ 3.0 - 250 m (Smyth et al., 1996a,b). Both AMP and CHAMELEON have a vertical resolution of better than 0.1 m. The temperature, salinity, and density data were provided in hourly 4 m vertical bins.

2.3.3 Surface heat fluxes, rainfall, and winds

Rainfall, wind speed and direction, and other meteorological variables were measured from the UOP mooring and from each of the ships. The hourly surface heat fluxes from the UOP mooring (Table 2.1) were provided by R. Weller (WHOI) using the COARE 2.5b bulk flux

Table 2.1. UOP mooring average surface heat fluxes, cumulative rainfall, and cumulative rainfall - evaporation (P-E).

	W9211A	W9211B	W9211C	Three-cruise result
Average surface heat flux (Wm^{-2})	63	-22	-5	12
Cumulative rainfall (cm) [†]	7	42	20	69
Cumulative P-E (cm)	1	32	11	44

[†] Precipitation data from UOP mooring represents a blend from the UOP mooring, S2 mooring, R/V Moana Wave, and R/V Wecoma.

algorithm (Fairall et al., 1996). The winds from each platform were similar, indicating that the wind stress was relatively uniform over the region of interest. Daily averages of wind stress at the UOP mooring and a 24-hour running average rainfall from a multi-platform composite (Anderson et al., 1996) are shown in Fig. 2.2. Accumulated rainfall and evaporation are summarized in Table 2.1. The evaporative freshwater flux was calculated using the measured latent heat flux and assuming a latent heat of vaporization of 2.43 MJ kg^{-1} at 30°C .

2.3.4 UOP mooring current data

The UOP mooring near the butterfly intersection was equipped with Vector Measuring Current Meters (VMCM), an Acoustic Doppler Current Profiler (ADCP), conductivity and temperature sensors, and with meteorological instruments (Plueddemann et al., 1993, Anderson et al., 1996). The VMCM units recorded currents every 3.75 minutes and were originally located at depths of 5.15, 8.9, 13.0, 17.0, 31.5, 39.5, and 52.5 m. The downward looking RD Instruments (RDI) ADCP located at 20.5 m was operated at 153 kHz, with a 16 m pulse length and 8 m bins, and recorded a 1.33 minute average profile from an 80 ping ensemble every 15 minutes. The shallowest ADCP bin used in our analysis was located at 69 m. Following a mooring repair on 12 Dec 1992, all current meters were displaced downward by 2.3 m. The VMCM near 40 m failed after 5 Jan and a linear interpolation between the adjacent current meters was used to complete the 40 m time series. All current data were low passed with a 32-hour cutoff and projected onto the vertical Seasoar data grid (0.8 m, 9.1 m, 17.4 m,...) using direct extrapolation of the 5.15 m VMCM data up to the

0.8 m bin and using linear interpolation between sensors for the other depth bins. The filtered current data (Fig. 2.2) are considered to be accurate to within 2 cm sec^{-1} based on a comparison with Moana Wave ADCP data (Appendix E).

2.3.5 Currents at surrounding platforms

Currents were also measured at four locations surrounding the central mooring: a PCM mooring, the S2 ADCP mooring, and two stationary ships (Fig. 2.1b). The moored Profiling Current Meter (PCM-N) at 1.25°S , 156.0°E cycled vertically at $\sim 10 \text{ m min}^{-1}$ once every three hours to measure currents at 20-195 m from 25 Oct 1992 to 8 March 1993. The PCM data were smoothed with a 20 m triangular filter and provided in 5 m bins by C. Eriksen (Univ. Washington). There were significant sampling gaps above 40 m so we used data only from depths $\geq 40 \text{ m}$; a few short gaps above 60 m (< 30 hours) were filled by linear interpolation in time. The S2 mooring at 2°S , 156.0°E measured currents with an upward looking ADCP located at 227 m from 4 Nov to 15 Feb (Kaneko et al., 1993). The ADCP was operated at 153 kHz with an 8 m pulse width and 8 m bins (K. Kutsuwada, Univ. of Tokai, Japan) were processed into 10 m bins centered at 20 to 210 m. A few data spikes were replaced by linearly interpolating in time. The Peoples Republic of China (PRC) ship Shiyan #3 near 2°S , 158°E acquired ocean current data (Chen Rongyu, South China Sea Inst. of Oce.) from 11 to 150 m in 4 m bins during three periods (7 Nov to 11 Dec, 17 Dec to 21 Jan, 28 Jan to 17 Feb) with a hull mounted RDI ADCP. The ADCP was operated at 307 kHz using a 4 m transmit pulse and 4 m bins and the ship's heading was obtained using a Sperry Mark 37

gyrocompass. The PRC ship Xiangyanghong #5 measured currents (S. Pu, State Oceanic Admin.) from 20 - 420 m using a RDI ADCP while maintaining station at 2°S, 154.5°E (10 Nov to 30 Nov) and at 2°S, 155°E (20 Dec to 8 Jan, 29 Jan to 17 Feb). Heading information was obtained using a Type III synchro gyrocompass and the ADCP was operated at 153 kHz using an 8 m transmit pulse and 8 m bins. The PRC data sets were acquired from the NODC Hawaii Archive Center (P. Caldwell) and consisted of hourly values at 10 m intervals beginning at 20 m. A few short data gaps in the R/V Shiyang#3 and Xiangyanghong#5 ADCP data were filled by linear interpolation in time; only one data gap was larger than 24 hours (R/V Xiangyanghong#5, 35 hours from 31 Jan to 1 Feb). All of the current data were 32-hour filtered before calculating the flow divergence.

2.4 Analytical Methods

2.4.1 *Depths of integration*

We consider advection for three different surface layers: the surface mixed layer (SML), defined as the layer in which the potential density difference ($\Delta\sigma_\theta$) between the surface and the bottom of the layer does not exceed 0.01 kg m^{-3} (Moum et al., 1989; Brainerd et al., 1995); the constant-depth layer between the surface and the 50 m isopleth; and the upper ocean layer (UOL) between the surface and the $\sigma_\theta = 22.0 \text{ kg m}^{-3}$ isopycnal. The SML often has very high turbulent kinetic energy dissipation (Smyth et al., 1996a, b) and its depth, heat, and salt content respond rapidly and strongly

to local surface forcing (Fig. 2.2). Brainerd and Gregg (1995) found $\Delta\sigma_\theta = 0.01 \text{ kg m}^{-3}$ to be a good criterion for determining the depth of the layer in which there is active mixing and high dissipation. This criterion was applied to the density data from each cruise using the shallowest routinely available observation to define the surface density, viz., 2 m. The average depth of the SML was $\sim 26 \text{ m}$ (Table 2.2) but ranged from $< 3 \text{ m}$ to over 70 m (Fig. 2.2). The 50 m layer was generally shallower than the top of the thermocline and often deeper than the SML (Fig. 2.2, Table 2.2). Ocean models (e.g. Zebiak and Cane, 1987) often use the 50 m layer to represent the upper ocean mixed layer. The base of the UOL closely corresponds to the top of the thermocline (Huyer et al., 1997, their Figs. 24, 25) and this layer is always deeper than the SML and is usually deeper than 50 m; its average depth was $\sim 76 \text{ m}$ and the temperature at the interface was $28.14 \text{ }^\circ\text{C}$ (Table 2.2).

Hourly values of the SML depth (h_{sml}) and UOL depth (h_{uol}) were determined from high resolution density profiles obtained from the Moana Wave for both W9211A (courtesy H. Wijesekera) and W9211B (courtesy W. Smyth). For W9211C, h_{sml} and h_{uol} were estimated from individual Seasoar profiles with 2 dbar resolution and then hourly averaged. A few gaps in h_{sml} of less than 18 hours were filled with data obtained from the UOP mooring (courtesy S. Anderson, WHOI) and corresponding temporal gaps in the h_{uol} time series were filled with linear interpolation of the Seasoar data. A 31-hour Welch filter (Press et al., 1989) was used to obtain low-passed values of h_{sml} and a 32-hour FFT filter was used to obtain low-passed values of h_{uol} (Fig. 2.2).

Given the direct dependence of horizontal advection on layer depth we examined the degree of lateral inhomogeneity of the SML and UOL by comparing the hourly estimates from the Moana Wave with the hourly

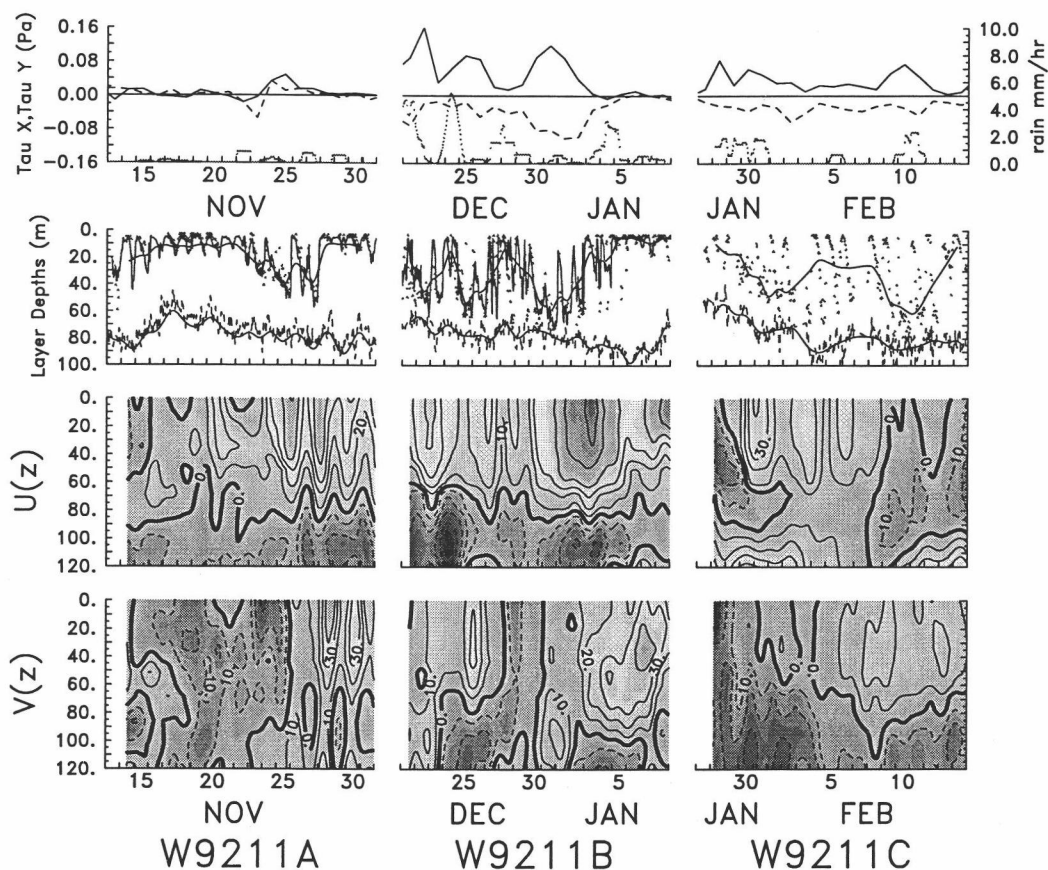


Figure 2.2 Time series of wind stress, rainfall, surface layer depths, and upper ocean currents at the center of the IFA. Top panel shows daily averages of zonal (solid) and meridional (dashed) wind stress at UOP mooring and 24-hour block averaged rainfall (dotted) made from a composite of rain data from Wecoma, Moana Wave, and the UOP mooring (Weller and Andersen, 1996). Second panel shows the depths of the SML and UOL: hourly values from Seasoar (dots) and MoanaWave (first the two cruises, jagged lines), and low-passed values (smooth curves, obtained from Moana Wave for first two cruises and from Seasoar profiles for the third cruise). The third and fourth panels show zonal and meridional components of the 32-hour low passed current measured at the UOP mooring.

values from the Wecoma for the first two cruises (Figs. 2.3, 2.4). The Wecoma and Moana Wave SML estimates suggest that the SML behaves fairly homogeneously across the butterfly (Fig. 2.3); correlation coefficients are significantly different from zero, and the mean differences, Δh , are small. The dependence of Δh on local time of day (Fig. 2.3) shows a relative minimum around local noon suggesting simply that diurnal heating was shoaling the layer everywhere but Δh showed no systematic dependence on platform separation. There are periods during W9211B when Δh is very large (> 30 m) and these are presumably due to salinity stratification induced by rainfall (Fig. 2.2) which was often patchy (Short et al., 1996). In general, however, h_{sml} was fairly homogeneous over the butterfly domain on time-scales of a few to several hours. The correlation coefficients indicate that h_{uol} was somewhat homogeneous (Fig. 2.4), though less so than h_{sml} ; differences in h_{uol} did not vary systematically with local time of day or platform separation distance.

2.4.2 Construction of horizontal temperature and salinity gradients

Data from the Seasoar surveys are used to construct time series of the horizontal gradients of the thermohaline field at the center of the butterfly pattern. Centered spatial gradient estimates are made for each meridional and zonal transect by fitting a line through the data for each depth bin along the transect (Fig. 2.5). The slope of the regression line is used as the gradient estimate for that depth bin. Least-squares fits were made over two length scales, 65 km and 130 km. The magnitude of the 65 km gradient estimate was usually larger than the 130 km estimate by 20 to 50% with sign differences only occurring when the magnitudes were small.

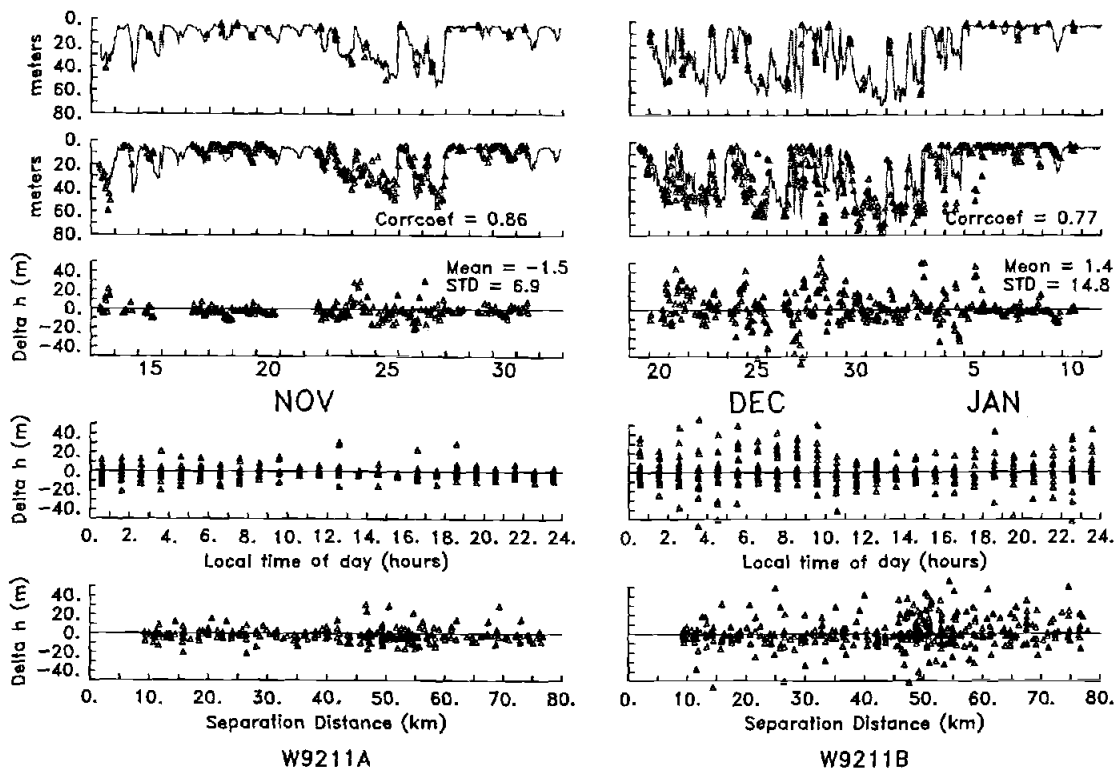


Figure 2.3 Time series of hourly SML depth estimated from R/V Moana Wave (solid line) and Seasoar (triangles) at the butterfly intersection (top), and at all Seasoar grid points (second row). Lower three rows show the depth differences plotted as a function of date/time, local time of day (GMT-10 hours), and lateral separation (km).

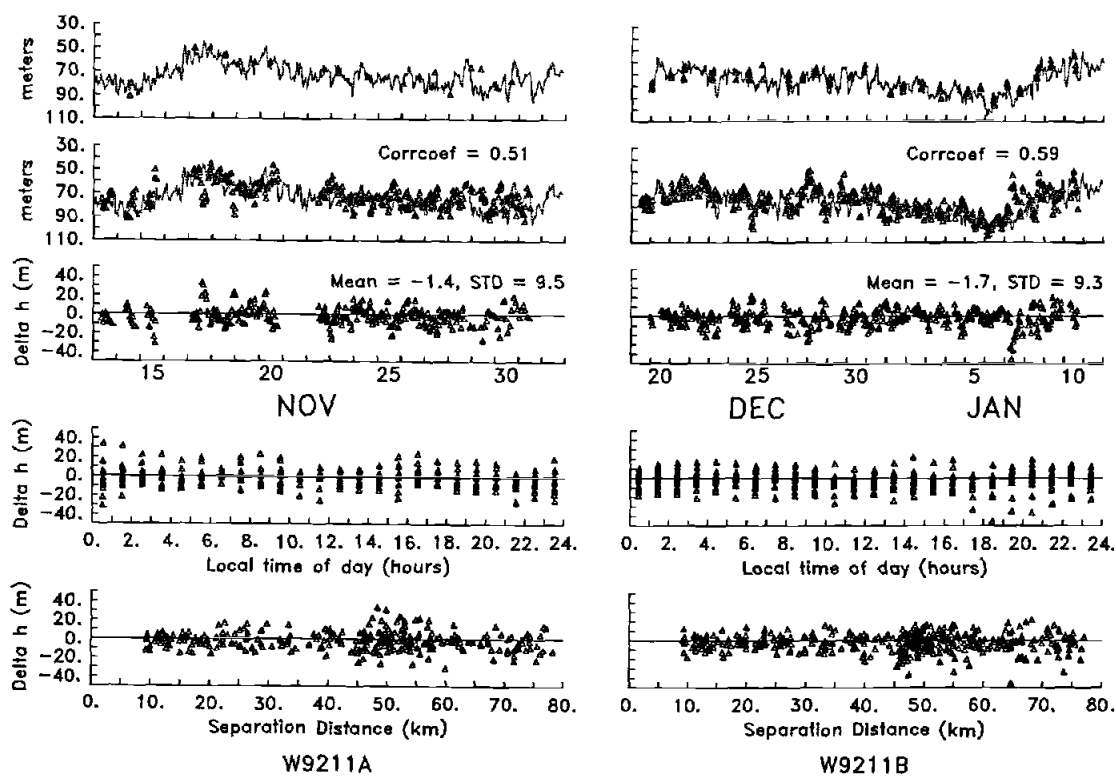


Figure 2.4 Time series of hourly UOL depth estimated from R/V Moana Wave (solid line) and Seasoar (triangles) at the butterfly intersection (top), and at all Seasoar grid points (second row). Lower three rows show the depth differences plotted as a function of date/time, local time of day (GMT-10 hours), and lateral separation (km).

For each survey period of about 20 days we obtained about 10 estimates of each component. Individual meridional and zonal estimates were separated by about 32 hours with the cross components staggered by about 16 hours. We used a conservative cubic spline (CSAKM.f, IMSL software routines, 1987) to interpolate the meridional and zonal gradient estimates to obtain hourly values of the horizontal gradient vector (Fig. 2.6).

The applicability of the linear fit to the individual transect data was estimated by calculating the significance of the correlation coefficient (Hamburg, 1977) using a student-t distribution with $n-2$ degrees of freedom. The value n is the effective degrees of freedom (Davis, 1976) and was estimated by dividing the number of horizontal grid cells used in the regression by the integral length scale (Tennekes and Lumley, 1972), also known as the decorrelation length scale. The integral length scales for both temperature and salinity were usually 2 to 4 horizontal gridcells (8-16 km) above the thermocline, but tended to be larger in the upper thermocline. The correlation coefficient was usually significant above the 90% significance level and often above the 95% significance level (Fig. 2.7). The 95% confidence intervals for the gradient were estimated using bootstrap statistics (Appendix A). The bootstrap confidence intervals (Fig. 2.8) are about twice as large as standard errors estimated from the student-t distribution with the same effective degrees of freedom.

2.4.3 Construction of vertical temperature and salinity gradients

Hourly values of 4 m binned (bin centers at 2, 6, 10 m,...) temperature and salinity from Moana Wave (W9211A,B) and Wecoma (W9211C) were center differenced vertically over 8 m to obtain estimates of

the vertical temperature and salinity gradients at 4 m intervals. A few gaps in the Seasoar sampling during W9211C were linearly interpolated in time. The vertical gradients were then 32-hour low-passed. For display purposes, the temperature and salinity profiles were separately filtered at 32-hours and are shown overlaid with the low-passed SML and UOL depths in Fig. 2.9.

2.4.4 Horizontal flow field

Given finite sampling in space and time, the presence of eddies, meanders, or strong horizontal shear could compromise the horizontal advection and vertical velocity estimates. Reliable calculations of these quantities require that the current is well represented at the location where horizontal advection is to be estimated and that the horizontal flow field is well resolved by the sampling array. We consider this question in two ways: (1) using simple correlation analysis of the currents and (2) using complex Empirical Orthogonal Function (EOF) analysis (Kundu and Allen, 1976) to resolve the spatially coherent flow field.

Time-depth distributions of the low passed currents measured at the various platforms (Figs. 2.10, 2.11) show that they are generally correlated. The temporal behavior and depth dependence of the currents was often very similar at all platforms, particularly during the strong wind burst period (W9211B). The three meridionally separated moorings (PCM-N, UOP, and S2) show very similar variations in both components, with zero contours appearing at approximately the same time and depth, and regions of positive and negative flow occurring at similar times and depths. The zonally (and more widely) separated current observations from Xiangyanghong#5 and Shiyang#3 are more weakly correlated except during

the sustained wind burst period (W9211B). These impressions are verified by correlation coefficient profiles between each of the platforms for each current component (Figs. 2.12a,b). During W9211A, the u and v components were generally poorly correlated but during W9211B the correlation of v for the PCM-N, UOP, and S2 is significant at all depths. The lower correlation of u may be due to the 4 Jan reversal of the near surface zonal current at PCM-N which did not occur at UOP and S2. During W9211C, both u and v above 80 m were strongly correlated between PCM-N, UOP, and S2 but not between the zonally separated stations.

We constructed complex EOF's using 32-hour low-passed data from each of the four platforms over the depth range of 40 m to 110 m to extract the coherent part of the flow field. For each cruise period, the first two EOF modes explained 60% to 70% of the variance and the first three EOF modes explained 80% to 90% of the variance (Figs. 2.13a,b,c). For W9211B, the first mode explains almost 50% of the variance and the mode structure (Fig 2.13b) is suggestive of Ekman turning toward the equator with depth in response to westerly winds. The correlation and EOF analyses suggest that the flow field was relatively homogeneous over the butterfly sampling region as required to justify the use of Seasoar thermohaline gradients to estimate advection at the butterfly center. The correlation and EOF analyses also suggest that it is reasonable to estimate vertical velocity from the horizontal divergence between the various platforms, which we discuss next.

Table 2.2. Average properties of surface layers: depth, layer interface temperature (T_h), and layer interface salinity (S_h).

	W9211A	W9211B	W9211C	3 Cruise Avg.
h_{sml} (m)	15, std = 12	29, std = 21	30, std = 22	26.2
T_h ($^{\circ}\text{C}$)	29.33	28.93	29.21	29.16
S_h (psu)	34.24	34.13	34.18	34.18
h_{uol} (m)	78, std = 10	75, std = 12	76.5, std = 13	76.5
T_h ($^{\circ}\text{C}$)	28.14	28.09	28.10	28.11
S_h (psu)	34.56	34.53	34.54	34.54

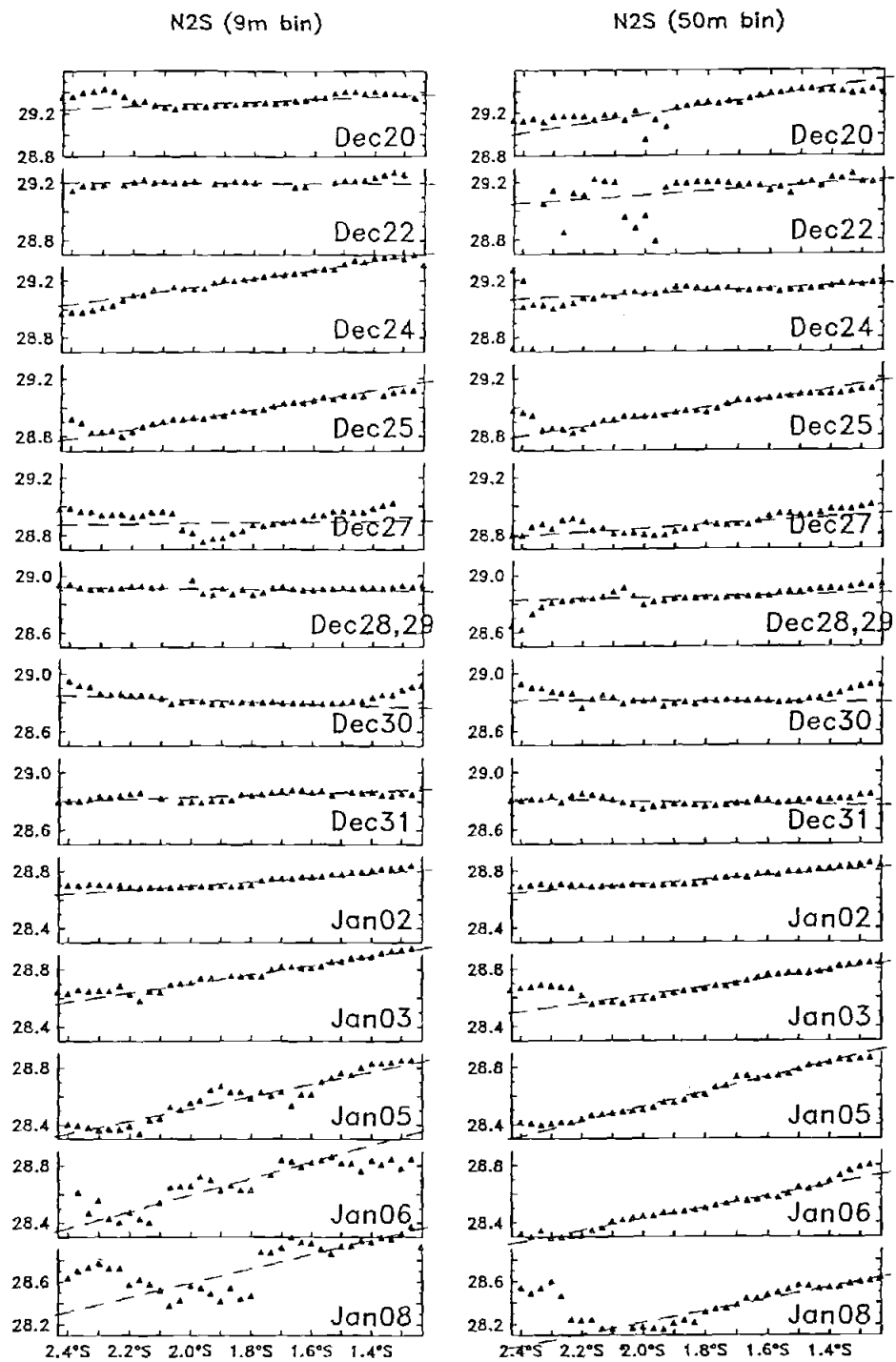


Figure 2.5 Meridional temperature profiles with 130-km regression lines at nominal bin depths of 9 m and 50 m for W9211B.

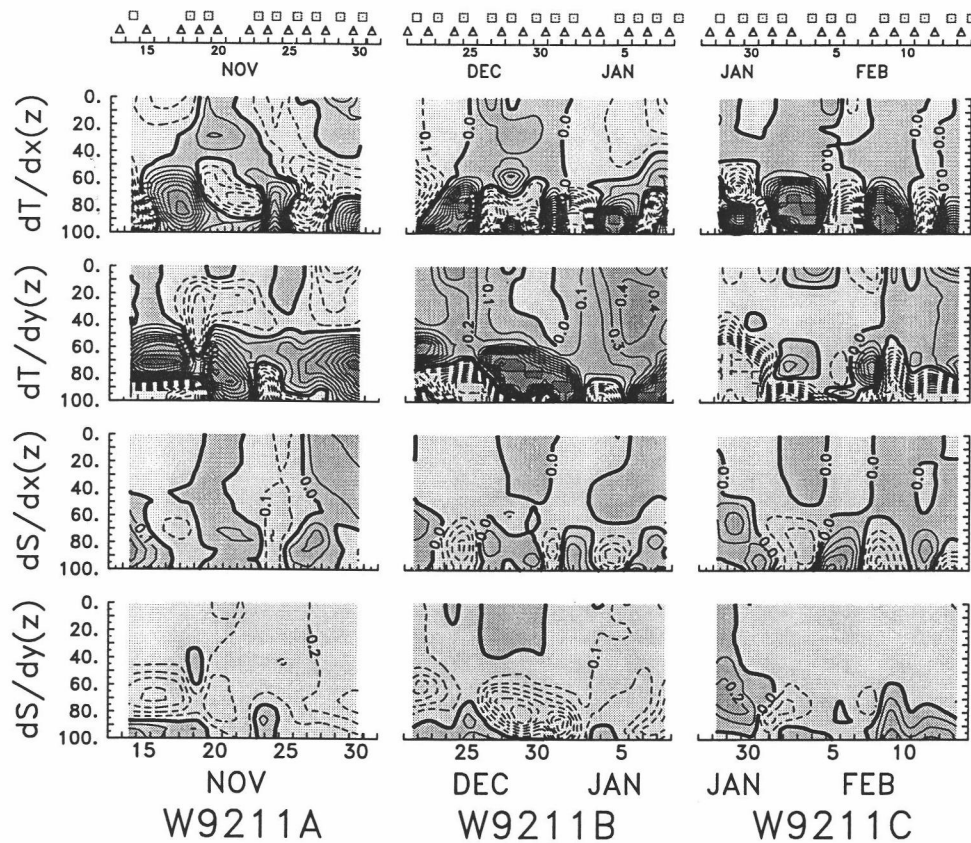


Figure 2.6 Large-scale (130 km) gradients of temperature and salinity, in units of $^{\circ}\text{C}/100\text{ km}$ and $\text{psu}/100\text{ km}$ respectively, as a function of time and depth (m). Contour intervals are 0.1 with dashed lines representing negative values. Symbols at the top denote time of sampling along meridional (triangles) and zonal (squares) sections.

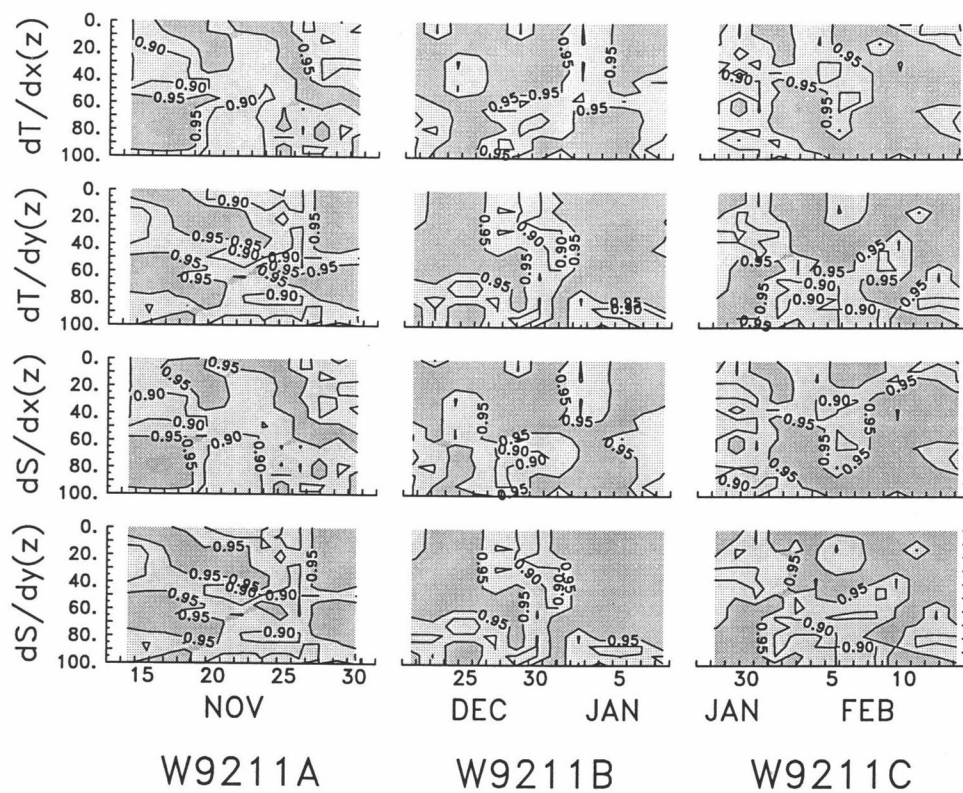


Figure 2.7 Significance level of the slope of the 130 km regression line. Note that this statistic does not distinguish between a poor fit and a zero slope. The degrees of freedom for the significance test have been adjusted using the estimated correlation length scale.

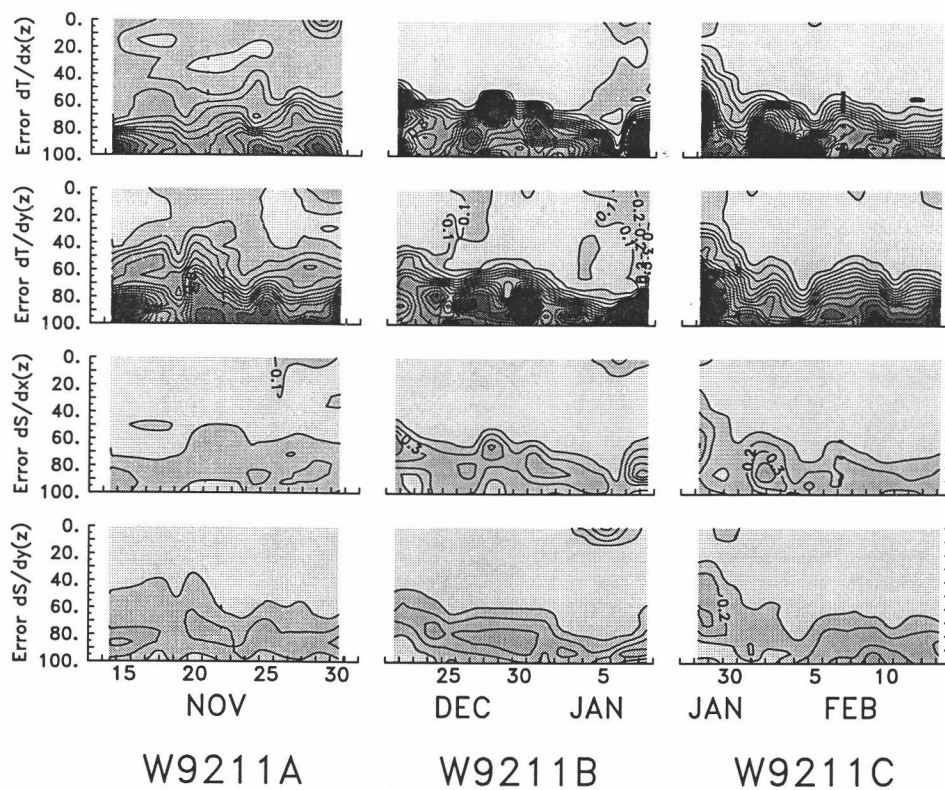


Figure 2.8 Time-depth distributions of the 95% bootstrap error estimates for the 130 km regression fits. The interpretation of the contoured value is as follows: a contour of 0.1 implies that the 95% error bar is ± 0.1 . The upper panel shows the error estimate of the zonal temperature gradient; contour interval is $0.1\text{ }^{\circ}\text{C}/100\text{km}$. The second panel shows the contour of the meridional temperature error estimate. Third and fourth panels show contours of the zonal and meridional salinity gradient error estimate; contour interval is $0.1\text{ psu}/100\text{km}$.

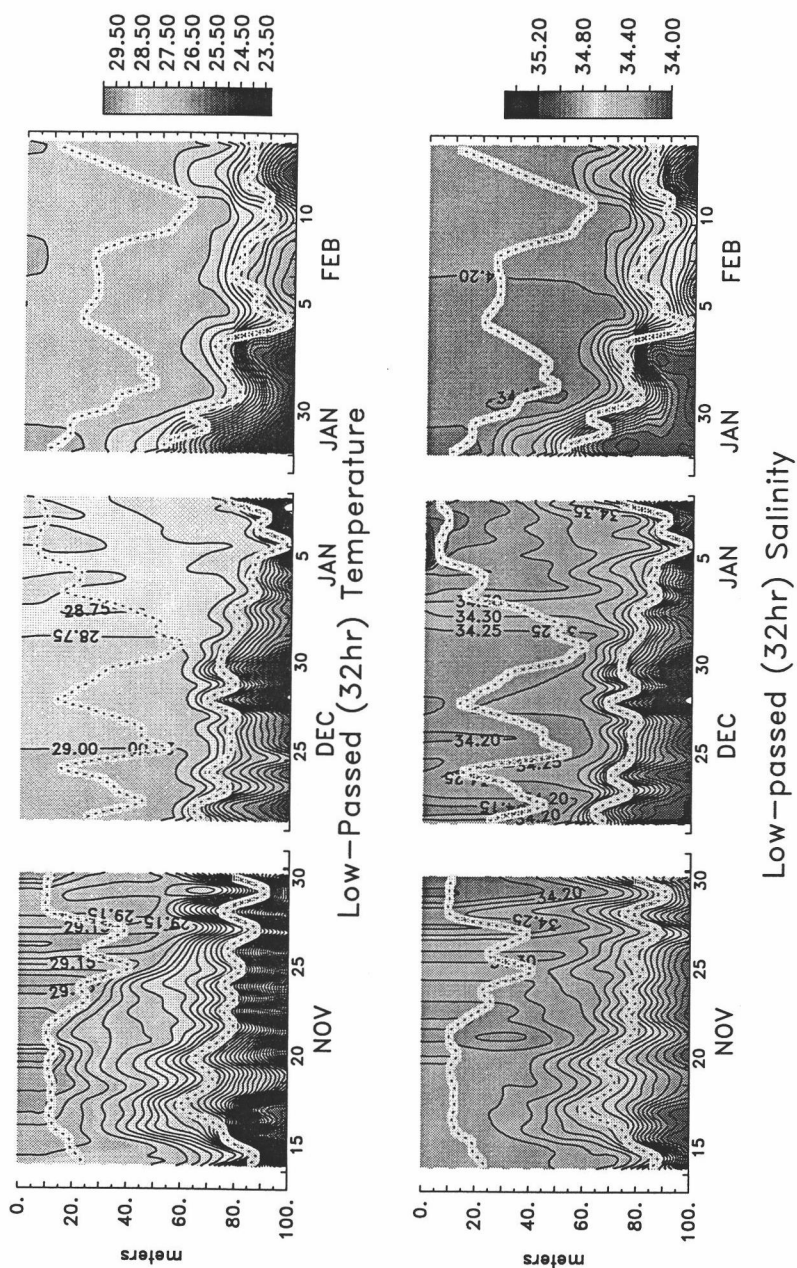


Figure 2.9 Low passed (32 hr) temperature and salinity distributions with SML and UOL depths superimposed. The temperature contour interval is 0.1 °C. Salinity contour interval is 0.1 psu. Data for the first two periods are from Moana Wave; data for the third period is from Wecoma.

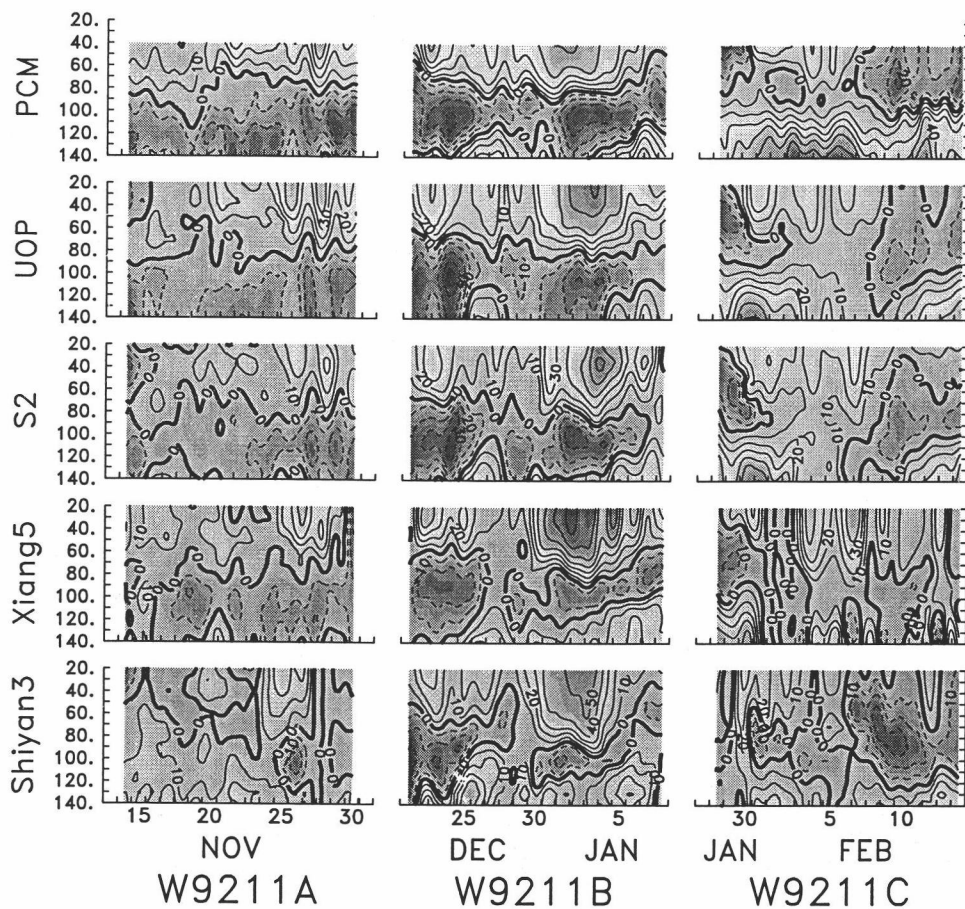


Figure 2.10 Low passed (32 hour) zonal currents from PCM-N, UOP, S2, R/V Xiangyanghong #5, and R/V Shiyang #3. Contour interval is 10 cm/sec.

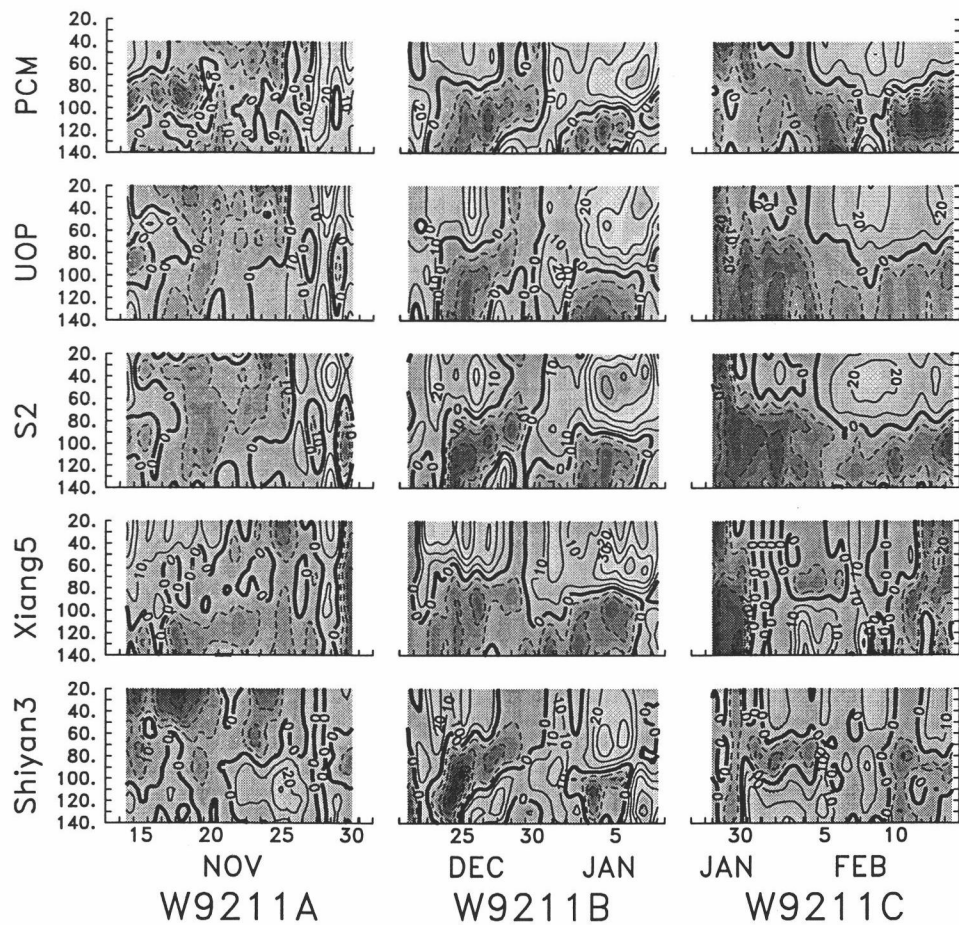


Figure 2.11 Low passed (32 hour) meridional currents from PCM-N, UOP, S2, R/V Xiangyanghong #5, and R/V Shiyan #3. Contour interval is 10 cm/sec.

2.4.5 Vertical velocity

The vertical velocity was obtained by vertically integrating the continuity relation, $w(z) = -\int_0^{-h} \left(\frac{\partial u}{\partial x} + \frac{\partial v}{\partial y} \right) dz$, with the sea surface boundary condition $w(z=0) = 0$, and assuming $\partial w / \partial z = \text{constant}$ above the shallowest current data bin reliably available (40 m) at which horizontal divergence could be explicitly estimated. This relatively straightforward approach to estimate vertical velocity is sensitive to measurement and sampling error but has been applied by others (Halpern and Freitag, 1987; Qiao and Weisberg, 1997). We estimated the horizontal divergence over lateral scales of ~ 100 to 300 km so that the calculated vertical velocity estimates have a similar horizontal scale dependence as the horizontal advection estimates. Using the 32-hour low-passed data, zonal divergence estimates were obtained by differencing between each possible pair of the zonally separated stations along the 2°S latitude line: R/V Shiyang#3 (158°E), S2 (156°E), and R/V Xiangyanghong#5 (at 154.5°E during W9211A and at 155°E during W9211B and W9211C), and one estimate of meridional divergence from PCM-N and S2. Three estimates of w were obtained using the three choices of zonal divergence and the meridional divergence from the PCM-N and S2 mooring. The vertical velocity estimates were generally similar so we show only the w time-depth distribution obtained using the zonal divergence estimated from the Shiyang#3 and Xiangyanghong#5 data (Fig. 2.14). The vertical velocity at h_{uol} was compared to the time derivative of the 32-hour low passed layer depth, $-\partial h / \partial t$ where $z = -h$ (Fig. 2.15a). To interpret Fig. 2.15a we consider a flux step across an ocean layer interface given by,

$$\Delta Q = \rho c_p \Delta T \left(\frac{\partial h}{\partial t} + u \frac{\partial h}{\partial x} + v \frac{\partial h}{\partial y} + w \right) \quad (2.4)$$

where ΔT is the temperature step and ΔQ is the flux step across the interface (deSzoeker, 1980). If turbulent mixing is weak for a deep layer (i.e. h_{uol}) then $\Delta Q \sim 0$ and if the layer depth is horizontally uniform (i.e. $\partial h / \partial x = \partial h / \partial y = 0$), then $w(z = -h) = -\partial h / \partial t$.

During W9211A mixing was weak (Wijesekera and Gregg, 1995) and the correlation between w_{-h} and $-\partial h / \partial t$ is significant at the 95% level (Fig. 2.15a). The correlation for W9211B was not significant even at the 90% level suggesting either mixing and/or horizontal advection of layer depth was important in modifying the local layer depth. The turbulent dissipation profiles (Smyth et al., 1996b, their Fig. 2) indicate that periods of intense mixing occurred from 20-23 Dec, 25-27 Dec, 30 Dec to 3 Jan and remained high in the region around h_{uol} after 3 Jan. Note that during the period of low turbulent dissipation, corresponding to a lull in the winds from 27-30 Dec, the estimated vertical velocity agrees well with $-\partial h / \partial t$. For W9211C, the correlation was not significant even at the 90% level suggesting that mixing, flow divergence, and horizontal advection of layer depth contributed to the h_{uol} displacement, or that the sampling array failed to resolve the relevant flow field scales. In particular, the downward displacement of the thermocline over 29-30 Jan and 3 Feb is not accounted for by the calculated vertical velocity (Figs. 2.9, 2.15a). Since the wind speed was moderate, turbulent mixing was likely insufficient to account for much of the downward movement of the thermocline. Instead, we suspect that it was either due to horizontal convergence that was not resolved by the sampling array and/or horizontal advection of the UOL depth.

Mean profiles of w (Fig. 2.15b) show that for each cruise, the three simple divergence estimates of w agree fairly well above 90 m. There was

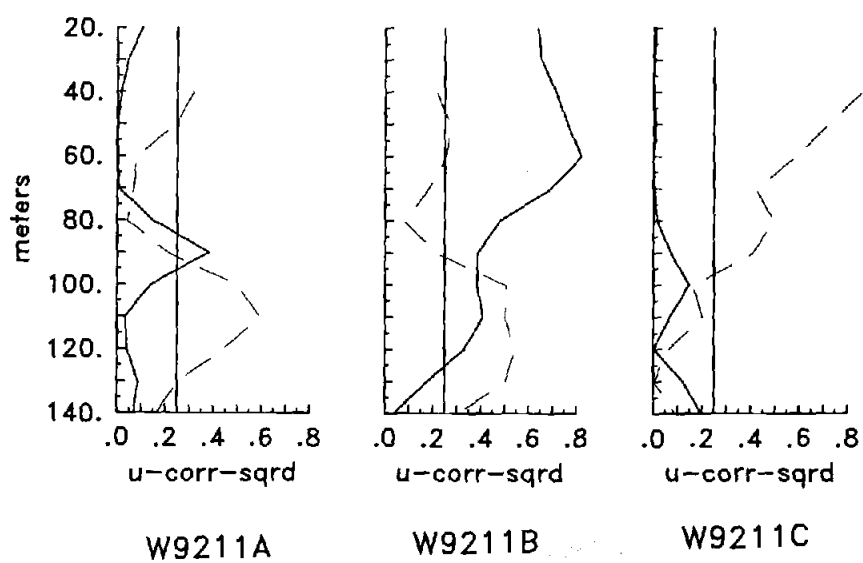


Figure 2.12a Squared correlation coefficients for the zonal currents from 32 hour filtered data. Solid line = correlation between Shiyang #3 and Xiangyanghong #5, dashed = PCM-N and S2. The 95 % significance level is plotted as a solid vertical line.

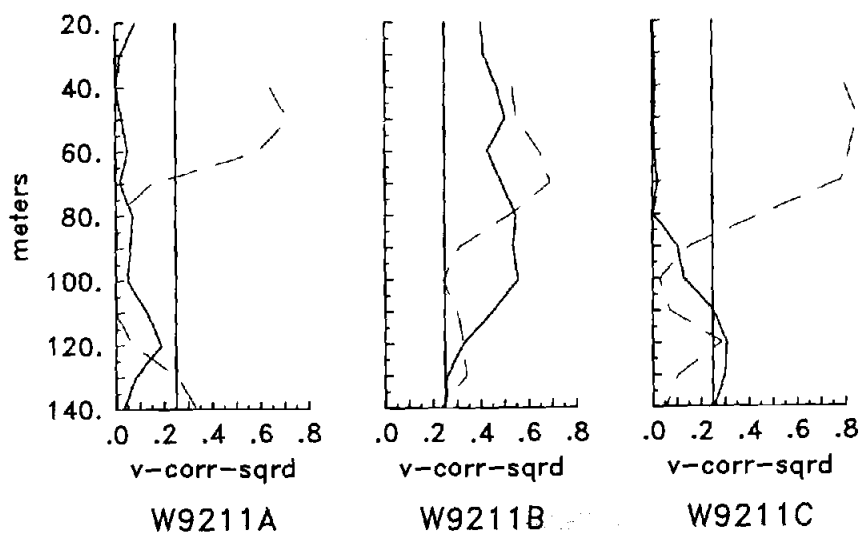


Figure 2.12b Squared correlation coefficients for the meridional currents from 32 hour filtered data. Solid line = correlation between Shiyan #3 and Xiangyanghong #5, dashed = PCM-N and S2. The 95 % significance level is plotted as a solid vertical line.

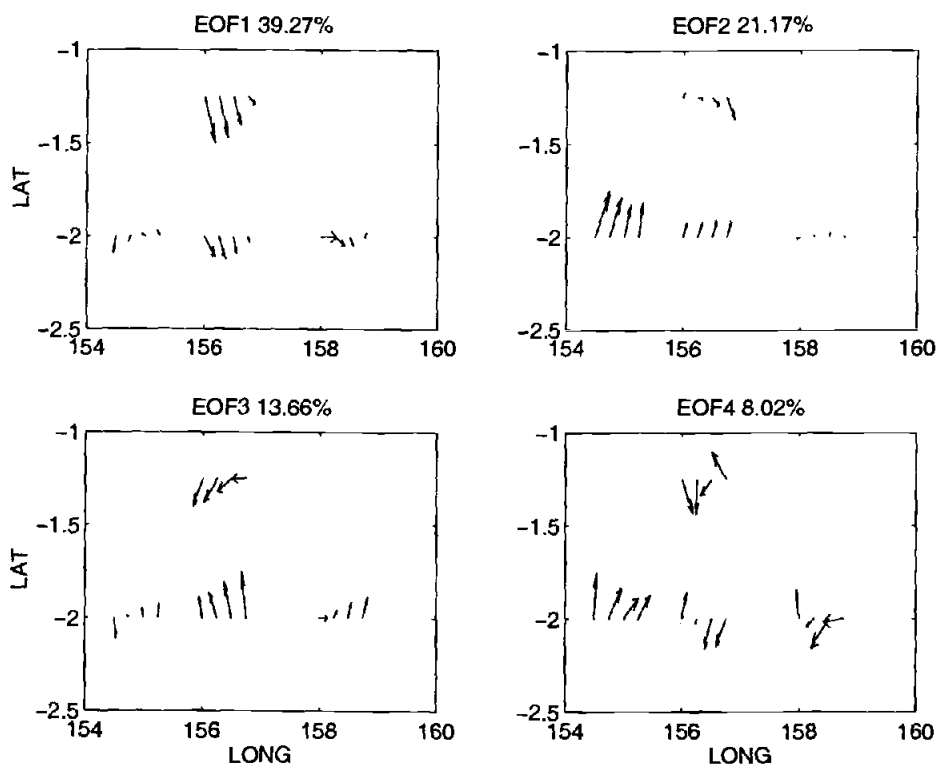


Figure 2.13a Orientation, magnitude, and the percent variance explained by each of the first four modes (EOF1-4) of the Complex Empirical Orthogonal Function eigenvectors at 40, 50, 60, and 70 m for each of the current platform sites for W9211A. The 40 m to 70 m eigenvectors are represented from left to right at each platform location.

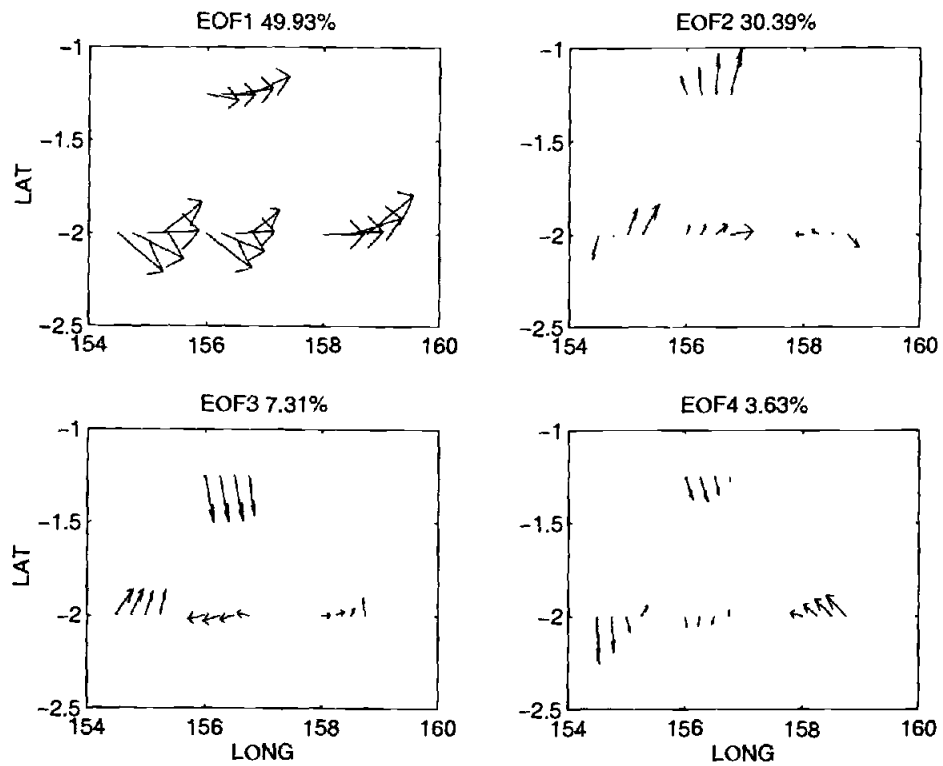


Figure 2.13b Orientation, magnitude, and the percent variance explained by each of the first four modes (EOF1-4) of the Complex Empirical Orthogonal Function eigenvectors at 40, 50, 60, and 70 m for each of the current platform sites for W9211B. The 40 m to 70 m eigenvectors are represented from left to right at each platform location.

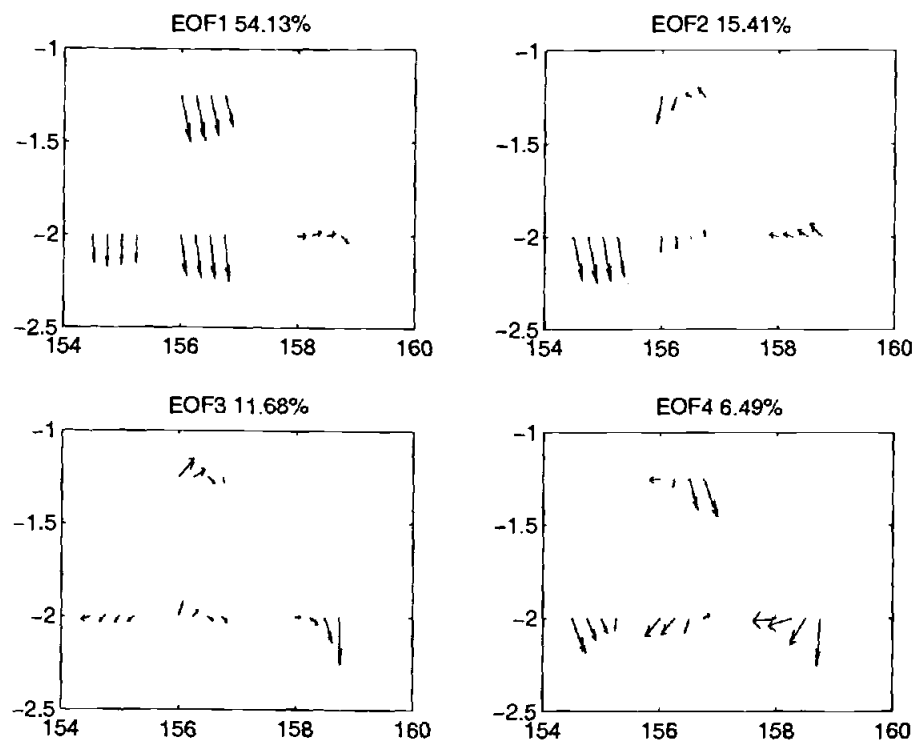


Figure 2.13c Orientation, magnitude, and the percent variance explained by each of the first four modes (EOF1-4) of the Complex Empirical Orthogonal Function eigenvectors at 40, 50, 60, and 70 m for each of the current platform sites for W9211C. The 40 m to 70 m eigenvectors are represented from left to right at each platform location.

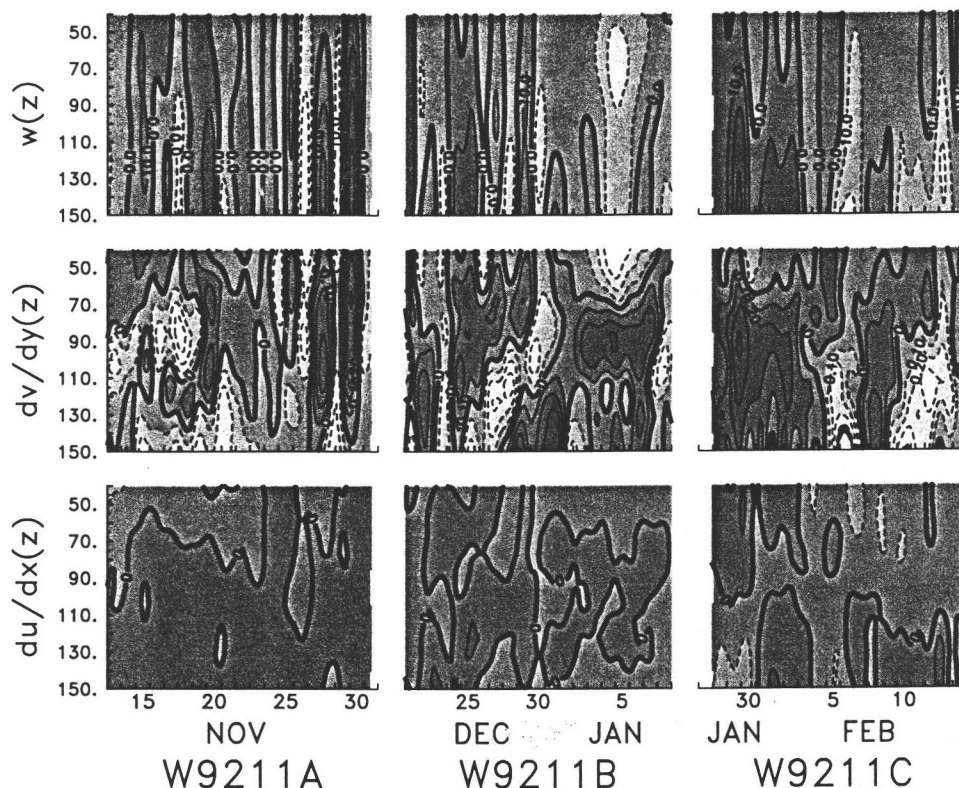


Figure 2.14 Time depth distributions of vertical velocity (w), meridional divergence ($\partial v / \partial y$) between PCM-N and S2, and the zonal divergence ($\partial u / \partial x$) between Shiyan 3 and Xiangyanghong #5. Contour intervals for w are 10 m day^{-1} . Contour intervals for the divergence plots are in units of day^{-1} . The vertical velocity in each panel is calculated using the horizontal divergence shown in the panels below. The divergence estimates were obtained using 32-hour low passed current data.

little net downwelling or upwelling above 90 m during W9211A, strong downwelling above 90 m during W9211B, and weak downwelling above 90 m during W9211C. The W9211B profile qualitatively agrees with vertical velocity estimates using Wecoma ADCP and Seasoar isopycnal data (Feng et al. 1998) but our estimate has about twice the amplitude. The average vertical velocity results appear consistent with the observed wind within a Rossby radius of the equator: weak winds imply weak vertical velocity, strong westerlies drive strong downwelling, and weak to moderate westerlies drive weak to moderate downwelling (Figs. 2.2, 2.15b).

Vertical velocity was also estimated by calculating the divergence of the complex EOF filtered data using currents represented by the first 3 EOF modes plus the mean at each platform (Kundu and Allen, 1976; Rudnick and Davis, 1988). This method gave vertical velocity estimates that compared well with the simple 32-hr FFT low-passed estimates discussed above (Fig 2.15a). In general, we expect that the EOF approach should give a better estimated vertical velocity than the simple FFT low-passed method because it tends to exclude the incoherent part of the flow field over the array provided the EOF series is appropriately truncated. Selection rules for retaining significant eigenmodes and series truncation has been discussed by various authors (Preisendorfer and Barnett, 1977; Overland and Preisendorfer, 1982; North et al., 1982). However, geophysical data sets often do not satisfy the degree of freedom criteria required to directly apply accepted statistical methods and our data set is no exception. Instead, we rely on the rule of thumb approach based on the relative amounts of variance explained by successive modes (North et al., 1982). We have truncated the current series at the third EOF which in our

case implies that over 80% of the low-passed current variance is included in the EOF estimated vertical velocity.

2.4.6 Horizontal and vertical advection

Horizontal advection in Eqns (2.1) and (2.2) was calculated by combining the low-passed UOP mooring currents with the horizontal gradients from Seasoar data to obtain the vertical profile of advective flux per unit volume as a function of time (Figs. 2.16, 2.17, 2.18, 2.19). This result was then integrated vertically over the low-passed layer depths to obtain the total horizontal advection per unit surface area for each layer, in units of Wm^{-2} and $\text{psu hr}^{-1}\text{m}^{-1}$. While the magnitude of the estimated horizontal gradients was often relatively small, $\leq 0.2\text{ }^{\circ}\text{C}/100\text{ km}$ and $\leq 0.2\text{ psu}/100\text{ km}$, the combination of relatively weak gradients with a deep mixed layer and energetic currents occasionally gave sizable horizontal advective fluxes in the SML. Vertical advection was estimated by vertically integrating the estimated vertical velocity with the vertical temperature and salinity gradients described above. Prior to completing the vertical integration, the vertical velocity was linearly interpolated to 4 m bins so that it had the same spacing as the vertical gradients. Vertical advection was negligible in the SML, moderate for the 50 m layer, and was generally very large for the UOL (Figs. 2.20, 2.21).

In the case of salt advection, we express salt advection in terms of an equivalent freshwater flux, f_w , for making direct comparisons with surface forcing. The advective salt flux increases the average layer salinity by $\Delta S = (Q_{s_{adv}}/h)\Delta t$, where $Q_{s_{adv}}$ is the advective salt flux, h is the average layer depth, and Δt is the time over which the flux acted. For an average layer

salinity, S_a , salt advection is equivalent to a local freshwater flux given by, $\Delta(\text{fw})/\Delta t = -Q_{s_{adv}}/S_a$ so that the local accumulated gain or loss of freshwater by salt advection is given by, $-(Q_{s_{adv}}/S_a)\Delta t$.

An error analysis for the advection estimates is discussed in Appendix B and only a brief remark is included here about the vertical component. We considered four different estimates of the vertical velocity to estimate the uncertainty in the vertical advection: three vertical velocity estimates, one from each estimate of zonal divergence, to calculate three estimates of vertical advection and a fourth estimate using the complex EOF vertical velocity discussed above. The average vertical advection in Tables 2.3 and 2.4 was obtained using the zonal divergence between Shiyan and Xiangyanghong (largest separation $\sim 300\text{km}$). The confidence intervals were established using the remaining two estimates of the zonal divergence (See Figure 2.15b) as a measure of the sampling error which was larger than the measurement error (Appendix B). We note that the confidence limits in Tables 2.3 and 2.4 may be too optimistic because they do not include uncertainty from the meridional divergence term. If we assume that the meridional contribution to the uncertainty of the divergence was equal to the zonal contribution the error bars would be $\sim 40\%$ larger assuming a Gaussian distribution of the errors. The EOF result gave an estimated vertical heat advection that was very close to the center estimate (Table 2.3) and well within the error bars except for the UOL during W9211C where the EOF estimate gave 73 Wm^{-2} vs. $44 \pm 20 \text{ Wm}^{-2}$ from the simple approach. For vertical salt advection, the agreement between the two methods was also very good (Table 2.4).

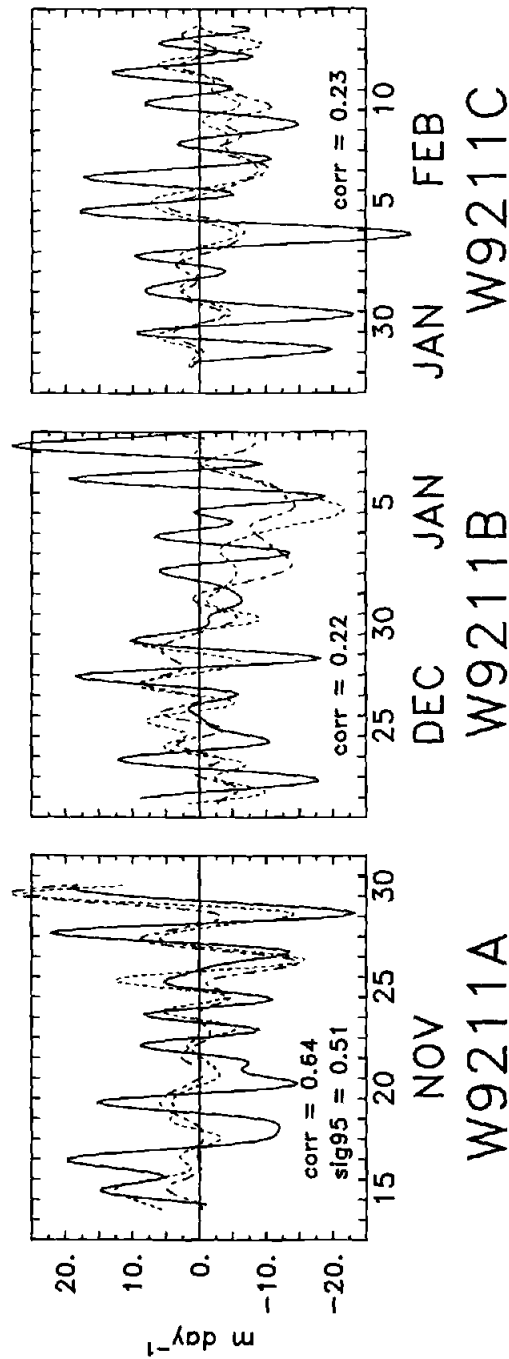


Figure 2.15a Time series of vertical velocity at the base of the UOL estimated from divergence and from the time derivative of the 32 hour low passed UOL depth, i.e. $-\partial h/\partial t$ (solid line). Simple differencing method estimate (small dash, lt. gray) and CEOF estimate (small-large dash, dark gray). The correlation coefficient is shown for $\partial h/\partial t$ and the vertical velocity estimate from the simple differencing method.

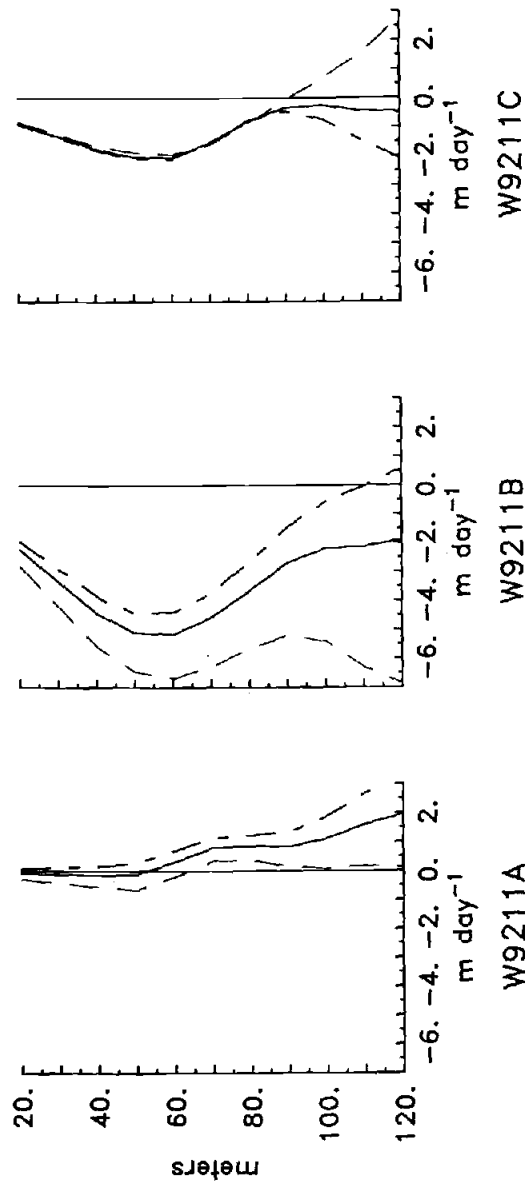


Figure 2.15b Average vertical velocity profiles. The solid line is the estimated vertical velocity obtained by integrating the sum of the meridional divergence ($\partial v/\partial y$) estimated from PCM-N and S2 and the zonal divergence ($\partial u/\partial x$) estimated from the R/V Shiyan #3 and R/V Xiangyanghong #5. The wide dashed line is an estimate of w using $\partial u/\partial x$ estimated from the R/V Shiyan #3 and S2 mooring. The long dash - short dash line is an estimate of w using $\partial u/\partial x$ estimated from the Atlas mooring and the R/V Xiangyanghong #5. These alternatives provide an estimate of the uncertainty in w .

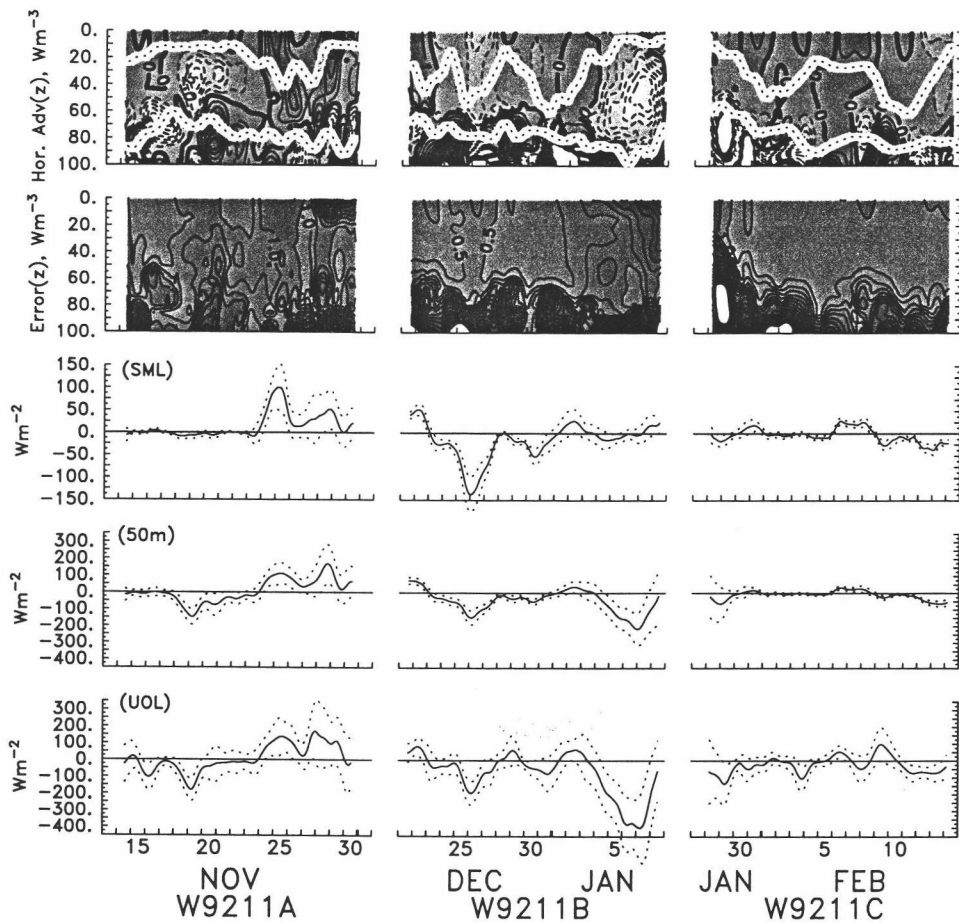


Figure 2.16 Vertical distributions of horizontal heat advection per unit depth (Wm^{-3}) and its error, both estimated from the large scale gradients, with SML and UOL depths superimposed. Time series of total horizontal heat advection (solid) with error bars (dotted), for the SML, 50 m layer, and UOL.

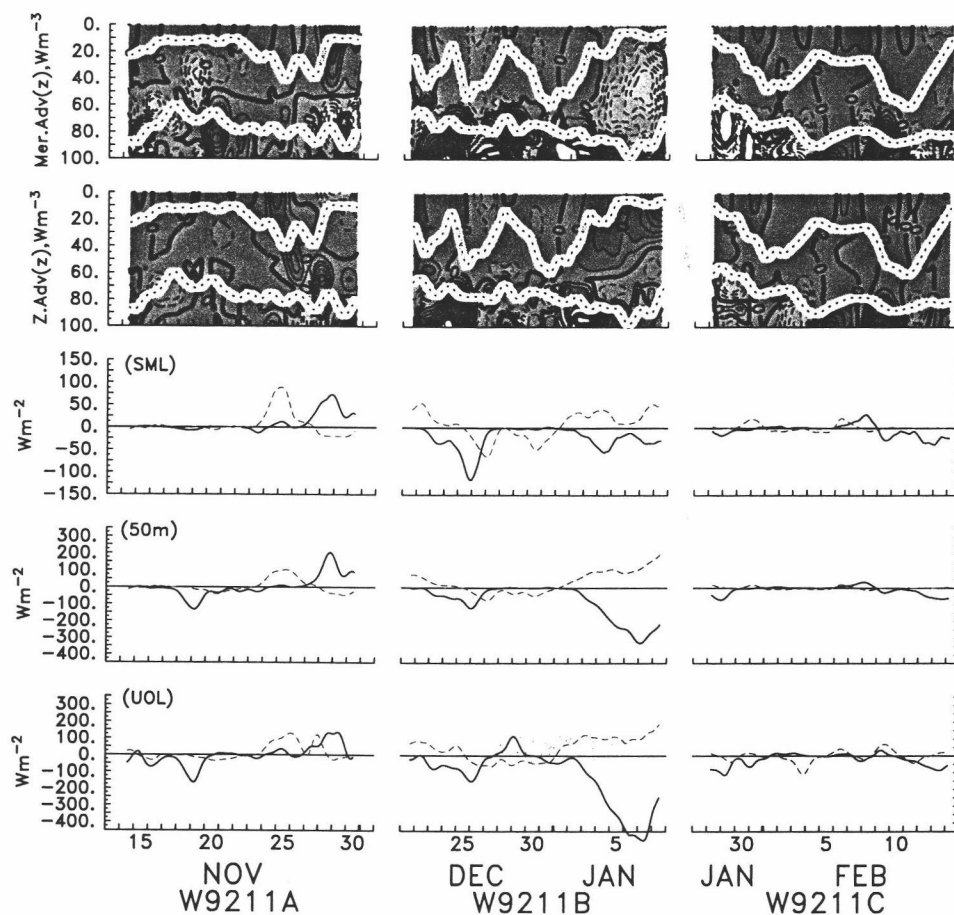


Figure 2.17 Vertical distributions of meridional and zonal heat advection per unit depth (Wm^{-3}), estimated from large scale gradients, with SML and UOL depths superimposed. Lower panels show time series of integrated meridional (solid line) and zonal (dashed line) heat advection contributions for the SML, 50 m layer, and UOL

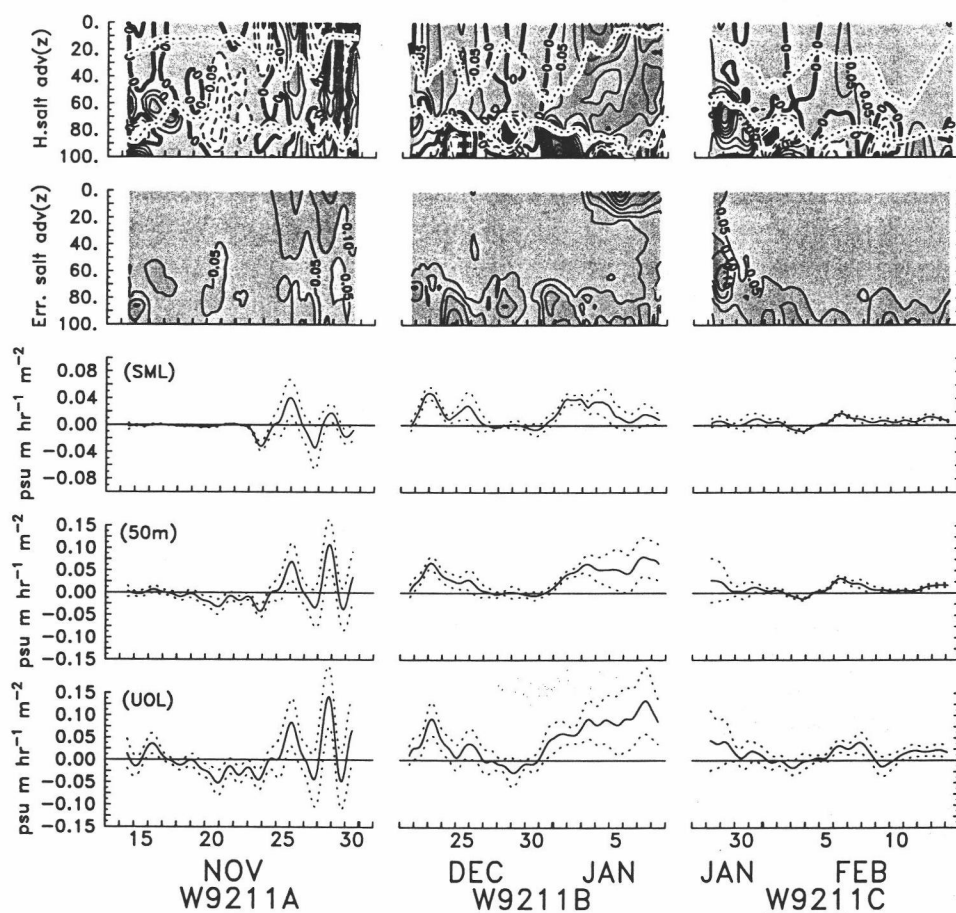


Figure 2.18 Vertical distributions of horizontal salt advection per unit depth ($psu\ hr^{-1}\ m^{-2}$) and its error, both estimated from the large scale gradients, with SML and UOL depths superimposed. Time series of total horizontal salt advection (solid) with error bars (dotted), for the SML, 50 m layer, and UOL.

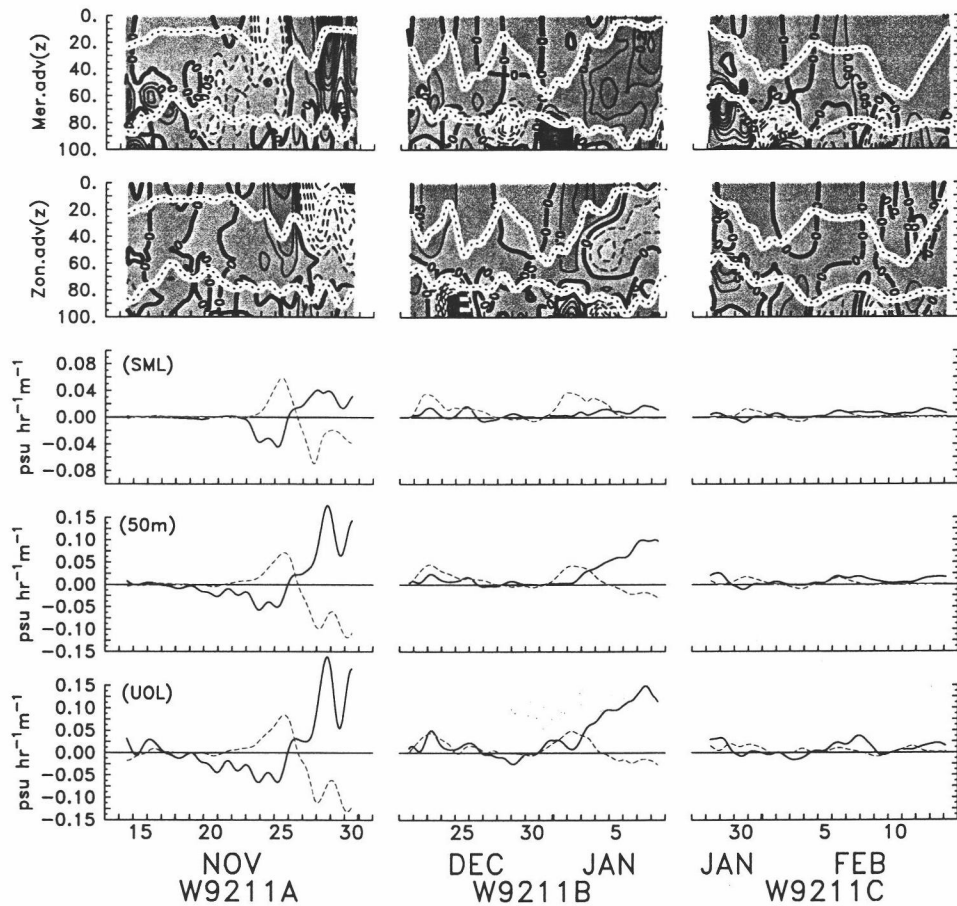


Figure 2.19 Vertical distributions of meridional and zonal salt advection per unit depth ($\text{psu hr}^{-1} \text{m}^{-2}$), estimated from large scale gradients, with SML and UOL depths superimposed. Lower panels show time series of integrated meridional (solid line) and zonal (dashed line) salt advection contributions for the SML, 50 m, and UOL.

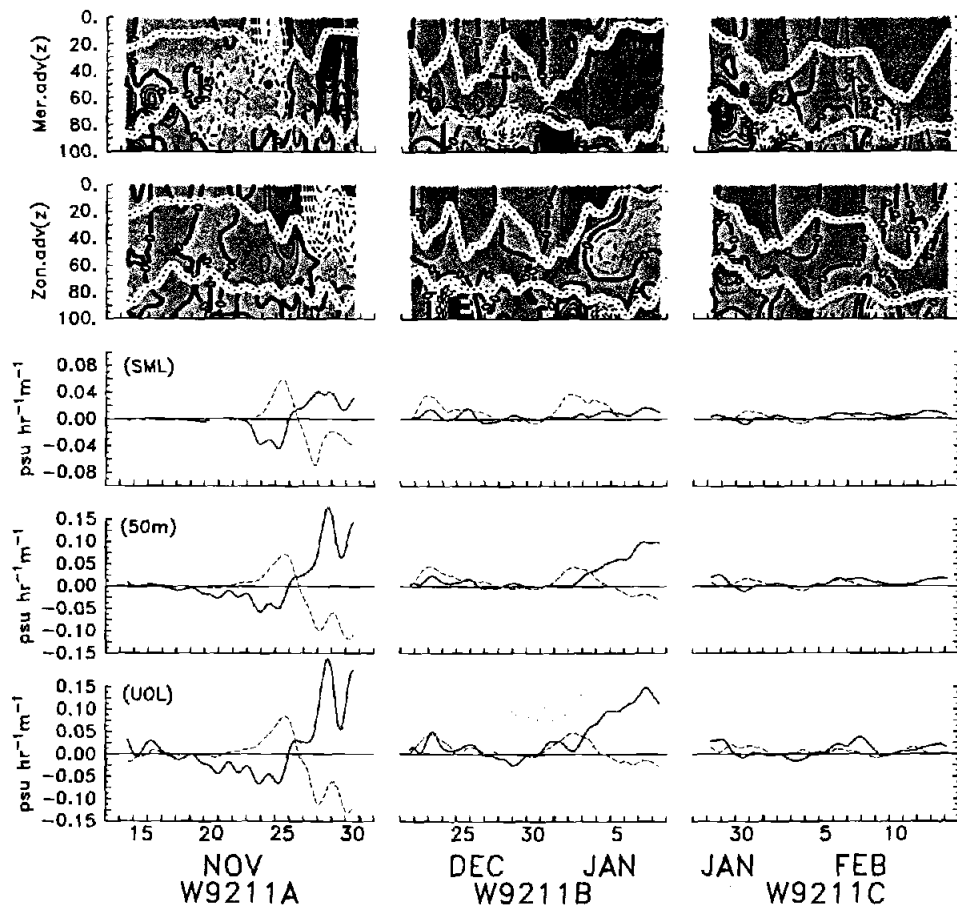


Figure 2.19 Vertical distributions of meridional and zonal salt advection per unit depth ($\text{psu hr}^{-1} \text{m}^{-2}$), estimated from large scale gradients, with SML and UOL depths superimposed. Lower panels show time series of integrated meridional (solid line) and zonal (dashed line) salt advection contributions for the SML, 50 m, and UOL.

2.5 Advection Estimates of Heat and Salt

In the following sub-sections we describe the temporal variability of the upper ocean advection and its response to the atmospheric and oceanic forcing observed during each survey period. The discussion of the data within each cruise begins with the 50 m layer heat and salt budget and is then followed by the SML and the UOL budgets.

2.5.1 W9211A: Nov 14 to Nov 30, 1992

Mostly weak winds (Fig. 2.2) and relatively clear skies were observed from 14-30 Nov. The conditions that were observed during this cruise perhaps typified the warm pool average state. Prior to the survey cruise, a strong westerly wind burst event occurred and lasted a couple of weeks ending on 12 Nov (Weller and Anderson, 1996; Cronin and McPhaden, 1997). This wind event was associated with strong cyclonic activity north (Typhoon Elsie) and south of the equator. Strong winds occurred briefly on 23-25 Nov and were initially northerly becoming westerly by 25 Nov. The SML was generally shallow (< 20 m) and spatially homogeneous (Figs. 2.2, 2.7) with a cruise average depth of 15 m (Table 2.2). The SST had a large diurnal variation of ~ 1 °C (Fig. 2.2) that diminished after the strong winds of 23-25 Nov to an amplitude of ~ 0.25 °C until 28 Nov when the SML shoaled to < 15 m (Fig. 2.2) and the diurnal amplitude became large again (Anderson and Weller, 1996; their Fig. 3d). The upper 50 m warmed at an average rate of $42 \pm 6 \text{ Wm}^{-2}$ estimated from

	W9211A (384 hours) Nov 14 - Nov 30		W9211B (429 hours) Dec 21 - Jan 08		W9211C (407 hours) Jan 28 - Feb 14		3 Cruise Average	
	mid-scale (65 km)	large scale (130 km)	mid-scale	large scale	mid-scale	large scale	mid-scale	large scale
SML								
Merid	20	8	-27	-23	-8	-5	-5	-7
Zonal	9	6	10	6	1	0	7	4
Total Horiz.	29 ± 14	14 ± 6	-17 ± 9	-17 ± 6	-7 ± 6	-5 ± 3	2 ± 10	-3 ± 5
Vertical (EOF Meth.)	0 ± 0.2, (0.03)	0 ± 0.2, (0.03)	0 ± 0.2, (0.15)	0 ± 0.2, (0.15)	0 ± 0.7, (0.7)	0 ± 0.7, (0.7)	0 ± 0.4 (0)	0 ± 0.4 (0)
Total	29 ± 14	14 ± 6	-17 ± 9	-17 ± 6	-7 ± 6	-5 ± 3	2 ± 10	-3 ± 5
50m Layer								
Merid	36	3	-102	-82	-32	-11	-33	-30
Zonal	-12	3	54	32	-5	0	12	12
Total Horiz.	24 ± 33	6 ± 16	-48 ± 20	-50 ± 13	-37 ± 12	-11 ± 6	-21 ± 22	-18 ± 12
Vertical (EOF Meth.)	-12 ± 6, (-7)	-12 ± 6, (-7)	28 ± 5, (33)	28 ± 5, (33)	1 ± 1, (2)	1 ± 1, (2)	6 ± 4 (9)	6 ± 4 (9)
Total	12 ± 33, (17)	-6 ± 17, (-1)	-20 ± 21, (-15)	-22 ± 14, (-17)	-36 ± 12, (-35)	-10 ± 6, (-9)	-15 ± 22 (-12)	-12 ± 13 (-9)
UOL								
Merid	19	-3	-144	-119	-67	-20	-64	-47
Zonal	6	12	56	38	-12	-3	17	16
Total Horiz.	25 ± 59	9 ± 29	-89 ± 40	-81 ± 27	-80 ± 30	-23 ± 18	-47 ± 43	-31 ± 25
Vertical (EOF Meth.)	-23 ± 15, (-28)	-23 ± 15, (-28)	109 ± 40, (115)	109 ± 40, (115)	44 ± 20, (73)	44 ± 20, (73)	43 ± 25 (53)	43 ± 25 (53)
Total	2 ± 61, (-3)	-14 ± 33, (-19)	20 ± 57, (26)	27 ± 48, (33)	-36 ± 30, (-7)	21 ± 27, (50)	-4 ± 50 (6)	12 ± 35 (22)

Table 2.3 Average heat advection (Wm^{-2}).

	W9211A (384 hours) Nov 14 - Nov 30		W9211B (429 hours) Dec 21 - Jan 08		W9211C (407 hours) Jan 28 - Feb 14		3 Cruise Total	
	mid-scale (65 km)	large scale (130 km)	mid-scale	large scale	mid-scale	large scale	mid-scale	large scale
SML								
Total Horiz.	-3 ± 6	1.9 ± 3	- 23 ± 8	- 20.4 ± 4	- 5 ± 3	- 6 ± 2	- 32 ± 10	- 24.5 ± 5
Vertical (EOF Meth.)	0 ± 0.1, (0.06)	0 ± 0.1 (0.06)	0 ± 0.3 (-0.002)	0 ± 0.3 (-0.002)	0 ± 0.1, (0.015)	0 ± 0.1, (0.015)	0 ± 0.2	0 ± 0.2
Total Adv.	-3 ± 6	1.9 ± 3	- 23 ± 8	- 20.4 ± 4	- 5 ± 3	- 6 ± 2	- 32 ± 10	- 24.5 ± 5
50m Layer								
Total Horiz.	-13 ± 14	- 0.5 ± 8	- 53 ± 15	- 40.4 ± 8	- 23 ± 6	- 11 ± 4	- 89 ± 21	- 51.9 ± 11
Vertical (EOF Meth.)	-1 ± 2, (-3)	-1 ± 2, (-3)	16 ± 2, (18)	16 ± 2, (18)	0 ± 1, (2)	0 ± 1, (2)	15 ± 5 (17)	15 ± 3 (17)
Total Adv. (EOF Meth.)	-14 ± 14, (-16)	-1.5 ± 8, (-4)	-37 ± 15, (-35)	- 24 ± 8, (-22)	- 23 ± 6, (-21)	- 11 ± 4.5, (-9)	74 ± 22 (-72)	- 36.9 ± 12 (-41)
UOL								
Total Horiz.	-17 ± 17	- 2.7 ± 12	- 74 ± 29	- 57.8 ± 15	- 36 ± 14	- 16 ± 7	- 127 ± 36	- 76.5 ± 22
Vertical (EOF Meth.)	- 6 ± 4, (-10)	- 6 ± 4, (-10)	64 ± 14, (55)	64 ± 14, (55)	13 ± 4, (21)	13 ± 4, (21)	71 ± 19 (66)	71 ± 19 (66)
Total Adv.	- 23 ± 17, (-27)	- 8.7 ± 13, (-13)	- 10 ± 32, (-19)	6.2 ± 21, (-3)	- 23 ± 15, (-15)	- 3 ± 8, (5)	- 56 ± 41 (-61)	- 5.5 ± 28 (-11)

Table 2.4 Cumulative freshwater advection (cm).

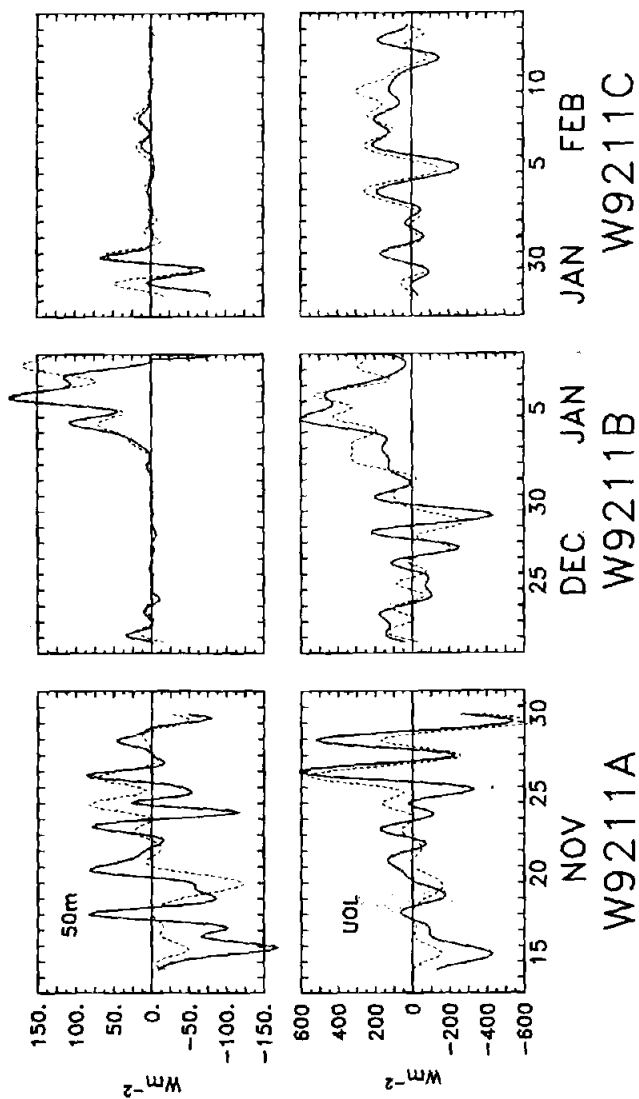


Figure 2.20 Vertical heat advection time series for the 50 m layer and UOL. Upper panel shows 50 m estimates (dashed = CEOF estimate). Lower panel shows UOL estimates (dashed = CEOF estimate).

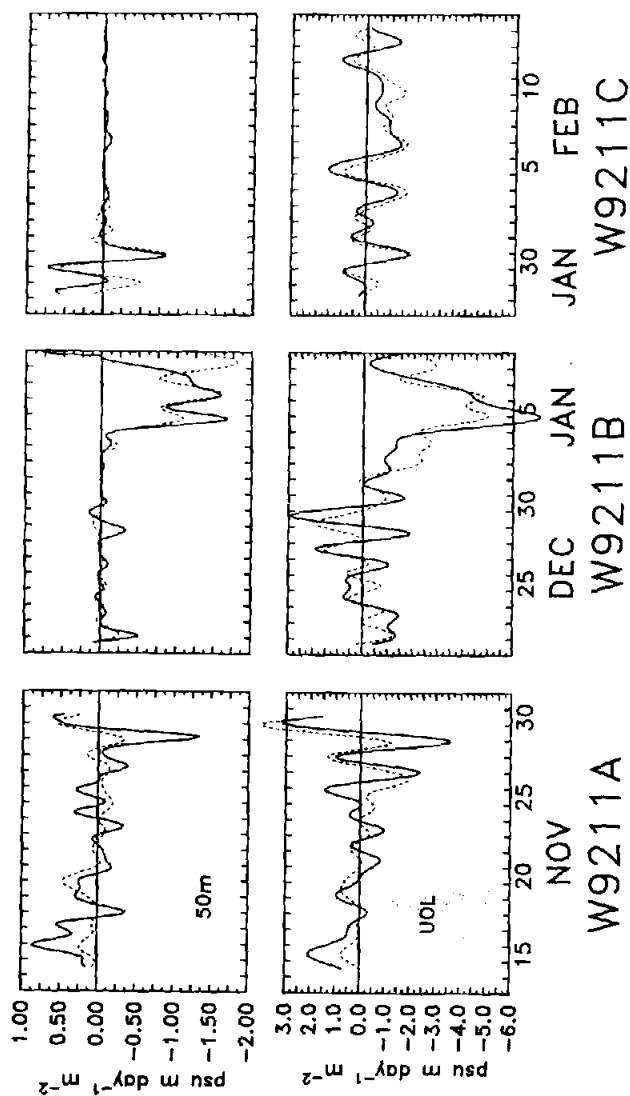


Figure 2.21 Vertical salt advection time series for the 50 m layer and UOL. Upper panel shows 50 m estimates (dashed = CEOF estimate). Lower panel shows UOL estimates (dashed = CEOF estimate). Note that the vertical axis is in units of $\text{psu m day}^{-1} \text{m}^{-2}$.

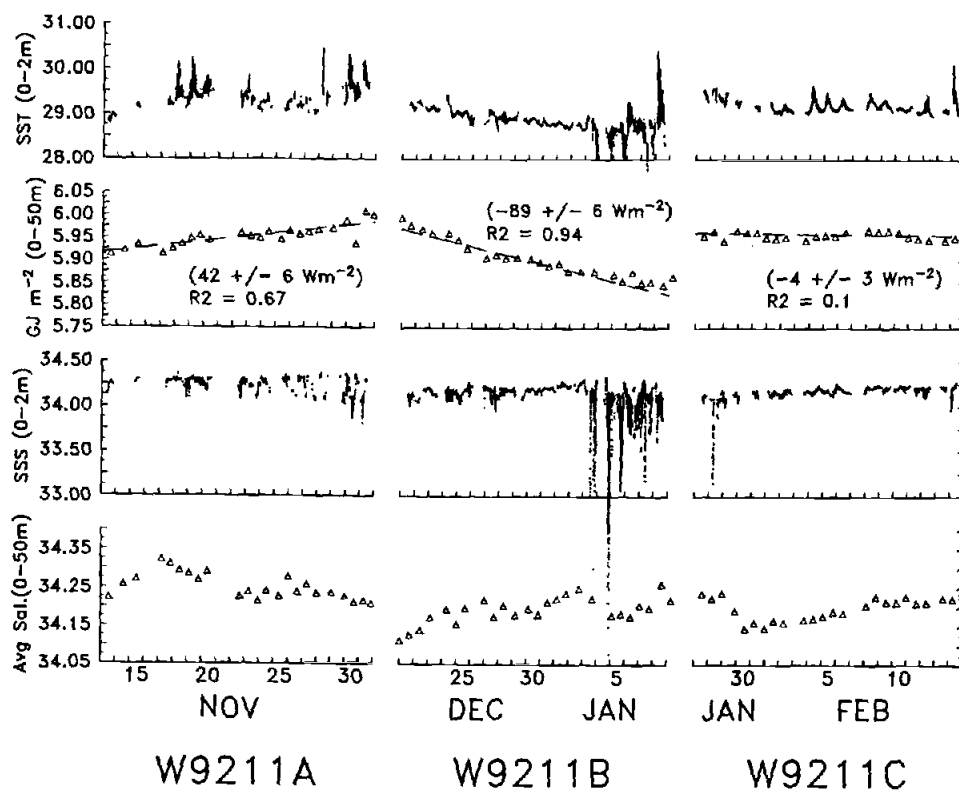


Figure 2.22 Time Series of Seasoar SST (0-2 m) from 1 sec data, upper 50 m heat content ($\int \rho c_p T dz$), Seasoar SSS (0-2 m) time series, and upper 50 m average salinity, ($1/50\text{m} \int S dz$). The gaps in the SST and SSS time series correspond to periods when the seasoar vehicle did not sample the upper 2 m or was onboard ship. The heat content and average salt content were estimated from successive Seasoar CTD sections and the best fit line gives an estimate of the average rate of change of heat storage (Wm^{-2}). Each data point (triangle) corresponds to a section average. For the entire period from Nov 13, 1992 to Feb 15, 1993, the average rate of change in heat storage was less than 1 Wm^{-2} (not shown) in the upper 50 m.

Seasoar sections (Fig. 2.22). The UOL was initially deep (> 80 m), perhaps in response to equatorial downwelling associated with the October wind burst, and then shoaled to ~ 60 m by 17 Nov before descending back to ~ 80 m by 30 Nov (Fig. 2.2). The average depth of the UOL was 78 m and the average interface temperature and salinity was 28.14°C and 34.56 psu, respectively (Table 2.2). During the period of weak winds prior to 23 Nov, the SML was shallow, and the flow above 70 m was generally south-eastward at 10 to 20 cm s^{-1} (Fig. 2.2). Lateral temperature and salinity gradients in the upper 50 m (Fig. 2.6) ranged from -0.4 to $0.2^\circ\text{C}/100\text{ km}$ and -0.2 and $0.2\text{ psu}/100\text{ km}$, respectively. The resulting advection of heat and salt in the SML from 14-23 Nov was very small (Figs. 2.16, 2.18). In the 50 m and UOL layers, modest horizontal advective fluxes tended to cool (Figs. 2.16, 2.17) and freshen (Figs. 2.18, 2.19) the layers as relatively cool and low saline water was advected from the north and west (Fig. 2.2). Vertical advection in the 50 m layer and UOL had a net cooling influence (Fig. 2.18) particularly before 20 Nov coincident with the shoaling of h_{uol} . Vertical salt advection correspondingly increased the salinity of both layers.

On 23 Nov there was a short burst of strong northerly winds ($\tau_y \sim 0.15\text{ Pa}$ for 5 hrs) and by 24-25 Nov there was a more sustained westerly burst ($\tau_x \sim 0.1\text{ Pa}$ for 12 hrs). These events deepened the SML, suppressed the diurnal surfacing of the SML, and generated moderately strong currents that had a ~ 2 -day oscillation (Fig. 2.2). The northerly wind accelerated a southward current and deepened the SML so that both penetrated down to about 30 m by 24 Nov. The westerly wind on 24-25 Nov accelerated the zonal surface current which penetrated down to ~ 50 m as wind stirring deepened the SML and distributed momentum downward. A 2-day wave seen in the PCM-N, UOP, and S2 data (Figs.

2.10, 2.11) appears to be meridionally coherent over the array but out of phase, with the currents in the north leading those in the south. The local inertial period at 1.75°S is 16.4 days so the 2-day wave is likely a locally forced mixed inertia-gravity wave. This wave apparently caused significant heat advection especially in the zonal direction (Figs. 2.16, 2.17); the horizontal components of salt advection were large but out of phase (Figs. 2.18, 2.19). The winds weakened on 26 Nov and the SML shoaled again to ~10 m by 28 Nov (Fig. 2.2) but advection was large during 26-30 Nov in all three layers since the currents were still relatively strong (Figs. 2.16, 2.18).

For this survey period, the average horizontal heat advection in the SML was $14 \pm 6 \text{ Wm}^{-2}$ (Table 2.3); the zonal and meridional contributions were 6 and 8 Wm^{-2} , respectively. Average horizontal heat advection in the 50 m layer and UOL were not different from zero and vertical advection tended to cool the upper ocean (Table 2.3). The estimated freshwater advection was not different from zero for all three layers (Table 2.4).

2.5.2 W9211B: 21 Dec 1992 to 8 Jan 1993

From 20 Dec to 3 Jan a westerly wind burst was observed (Smyth et al., 1996a,b) that had strong northwesterly winds of $5\text{-}10 \text{ ms}^{-1}$ accompanied by high precipitation. The windy period was followed by a calm rainy period from 3-10 Jan (Fig. 2.2). Seasoar data show that the upper 50 m cooled at an average rate of $\sim -89 \text{ Wm}^{-2}$ and the upper 50 m became saltier by $\sim 0.1 \text{ psu}$ (Fig. 2.22) despite the high rainfall. The top of the main thermocline was usually below 50 m and often below 60 m, and the upper 50 m layer was usually fairly well mixed (Fig. 2.9). The average SML

depth was 29 m (Table 2.2) and the low-passed SML depth appears well correlated with the daily averaged wind stress (Fig. 2.2). The UOL deepened almost steadily from 65 to 90 m from 21 Dec to 6 Jan and then shoaled to 70 m by 9 Jan; the cruise average depth of the UOL was 75 m (Table 2.2). The meridional and zonal temperature gradients above 50 m (Fig. 2.6) appear to be almost anti-correlated similar to the W9211A results. The low-passed zonal current at the UOP was eastward in the upper 70 m, reaching speeds $>60 \text{ cm s}^{-1}$ in the upper 25 m at the end of the third phase of the wind burst on 3 Jan (Fig. 2.10). A westward counterflow of $10\text{-}30 \text{ cm s}^{-1}$ was present below 80 m, similar to the subsurface counterflow observed during W9211A. The meridional current had a weaker depth dependence than the zonal current; above 80 m it was generally northward at 10 to 30 cm s^{-1} (Fig. 2.11).

During the high wind period, the SML was deep and the diurnal cycling of the SML depth was greatly modified by the effects of wind stirring and rainfall (Fig. 2.2). The UOL was usually well mixed and the region just below it was strongly stratified (Fig. 2.9). During peaks in the winds, the h_{sml} became as deep as 80 m and approached to within several meters of h_{uol} on 22, 25, 26, 31 Dec and 1 Jan (Fig. 2.2). The combination of a deep SML, modest temperature gradients, and moderate currents gave a large advective cooling event on 25 to 27 Dec (Figs. 2.16) that corresponds to a large residual in the one-dimensional budget computed from data taken by the R/V Moana Wave (Smyth et al., 1996b). The SML heat advection components (Fig. 2.17) reveal that this event had a large meridional contribution of about -100 W m^{-2} followed by a moderate zonal contribution of about -50 W m^{-2} . Related positive salt advection features can be seen in the salt advection time series (Fig. 2.19) but these features are not as prominent in the 50 m layer and the UOL. Despite a moderately strong

northerly wind, the meridional current response after 31 Dec was dominated by the Coriolis force which rotated the strong zonal current northward (Smyth et al., 1996a). For all three layers, horizontal advection from 27 Dec to 3 Jan was dominated by the zonal component. Vertical advection over the period 21 Dec to 3 Jan was small for the SML and 50 m layers; its average was also small for the UOL though there was large variability (Figs. 2.20, 2.21).

During the relative calm, 3 to 8 Jan, the SML shoaled and h_{sml} remained small even at night (Fig. 2.2) because of weak winds and rain-induced salinity stratification near the surface (Fig. 2.9, 2.22). The meridional temperature gradient became increasingly positive after 1 Jan while the zonal gradient became increasingly negative (Figs. 2.5, 2.6). The meridional temperature gradient increased in magnitude after the winds subsided and by 5 Jan it was larger than $0.4\text{ }^{\circ}\text{C}/100\text{ km}$ between 10 to 50 m depth (Fig. 2.6). Although the meridional temperature profiles show strong small-scale horizontal gradients at this time (Fig. 2.5), the temperature gradients at the center are described reasonably well by the linear fit, at least to first order. The resulting meridional advection produced strong cooling while zonal advection gave warming (Fig. 2.17). Vertical advection of heat into the 50 m layer and the UOL was strongly positive while vertical advection of salt was negative consistent with downwelling.

On average, horizontal heat advection during W9211B cooled the SML at an average rate of -17 Wm^{-2} and the upper 50 m by -50 Wm^{-2} (Table 2.3). Vertical heat advection for the 50 m layer averaged 28 Wm^{-2} , most of which occurred in the last few days of the cruise period. Average horizontal heat advection in the UOL was about $-81\pm 27\text{ Wm}^{-2}$ and average vertical advection was estimated at $109\pm 40\text{ Wm}^{-2}$ giving a total average heat

advection for the UOL of $\sim 27 \pm 48 \text{ Wm}^{-2}$. Horizontal salt advection into the SML was equivalent to a freshwater loss of about 20 cm (Table 2.4) and acted to balance a large fraction of the net surface freshwater input of 32 cm (Table 2.1). For the SML and 50 m layer, meridional and zonal salt advection components were generally positive (Fig. 2.17) while vertical salt advection was generally negative (Fig. 2.20). For the upper 50 m, horizontal salt advection was equivalent to a loss of ~ 40 cm of freshwater. Vertical salt advection was equivalent to a gain of 16 cm of freshwater for the 50 m layer (Table 2.4) giving an accumulated advective loss of 24 ± 8 cm of freshwater for the 50 m layer.

2.5.3 W9211C: 28 Jan to 14 Feb, 1993

Weak to moderately strong south-easterly winds blew over the region for about three weeks before the commencement of W9211C (Weller and Anderson, 1996). At the beginning of the cruise, the ocean appeared to be in an upwelling regime with a shallow thermocline (Fig. 2.9) and a southwestward surface flow (Fig. 2.10). Winds during the cruise were moderately strong north-westerlies that were punctuated with strong squalls particularly during 27-31 January and 9-11 February. The period of squalls had mean air-sea heat, freshwater, and momentum fluxes comparable to those during W9211B (Weller and Anderson, 1996). The change in the upper 50 m heat and salt storage over the whole period was not significantly different than zero (Fig. 2.22) and horizontal gradients were usually weak (Fig. 2.6). The diurnal range of h_{sml} was often large, from ~ 0 m to over 70 m, and the low-passed SML depth appears correlated with the daily winds (Fig. 2.2). The zonal component of the current was

initially westward in the upper 80 m and became eastward after 29 Jan, only occasionally attaining magnitudes greater than 20 cm s^{-1} . Unlike W9211B, the surface zonal current weakened over time despite moderate westerly wind forcing and a subsurface westward counterflow was not observed below 80 m. There was a deep southward counterflow below 80 m much of the time at the PCM, UOP and Atlas moorings but the counterflow was not always present at Xiangyanghong #5 and Shiyan #3.

From 27 to 30 Jan, the top of the thermocline was very shallow at $\sim 40 \text{ m}$ (Fig. 2.9) and the resulting horizontal temperature gradients gave large horizontal heat fluxes for the UOL. During this period, horizontal heat advection estimates for the 65 km vs. 130 km gradient scales differed markedly and account for most of the cruise mean differences for the two scales seen in Table 2.3. Given the shallow and rapidly changing thermocline depth it is suspected that a large part of the difference between the two scale estimates is due to tidal aliasing (Appendix B). We cannot clearly determine which horizontal scale is most appropriate especially because the internal tidal wavelength is $\sim 100 \text{ km}$ and the two estimates may therefore best serve as a bounds on the advection estimate for the UOL.

On 30 Jan the top of the thermocline deepened to $\sim 70 \text{ m}$ (Fig. 2.9) at least partially due to surface convergence (Fig. 2.15a). The large vertical advective flux associated with the deepening thermocline is only partially represented in the vertical advection estimates (Figs. 2.21, 2.22) because the vertical velocity estimates alone fail to account for the rapid change in the thermocline depth for this period as noted in section 2.3e. It is unclear if the vertical velocity estimates are a gross underestimate or that horizontal divergence is only partly responsible for the vertical response with lateral

advection of the layer depth and turbulent mixing being responsible for the other part.

After 1 Feb, the thermal structure between the 20 m isobar and the top of the thermocline showed little temporal or spatial dependence (Fig. 2.9) and weak meridional and zonal gradients persisted until near the end of the survey (Fig. 2.6). The apparent spatial variability in the upper 20 m horizontal temperature gradients (Fig. 2.6) is likely due to aliasing of the diurnal signal into a spatial gradient (see Appendix B). The salinity field showed small scale patchiness on scales of 10 to 30 km until around 4 Feb (Huyer et al., 1996) when a fairly weak but persistent meridional gradient of ~ 0.05 psu/100 km was observed (Fig. 2.6). The low passed h_{sml} response appears to be correlated with the winds (Fig 2.2), but even for the relatively low wind period, 3 to 8 Feb, the unfiltered SML depth range had a large diurnal cycle. Despite the deep SML and modest currents, horizontal heat advection for all three layers had little variability (Figs. 2.17) due to the weak gradients (Figs. 2.6) and horizontal salt advection was small but usually positive (Figs. 2.19, 2.20). Vertical advection of heat and salt was generally small in the 50 m layer but had notable variability in the UOL (Figs. 2.20, 2.21).

The SML average horizontal advective heat flux was about zero ($-5 \pm 3 \text{ Wm}^{-2}$) for this period (Table 2.3). Meridional advection dominated the upper 50 m average lateral advection of $-11 \pm 6 \text{ Wm}^{-2}$ and the estimated average vertical heat advection was 1 Wm^{-2} . Average horizontal heat advection for the UOL was between -23 to -80 Wm^{-2} and the average vertical heat advection was $44 \pm 20 \text{ Wm}^{-2}$ (73 Wm^{-2} for the EOF calculation). We suspect that the mean vertical advection estimate may underestimate the actual vertical advection because of the poor representation of the thermocline displacement early in the cruise period (Figs. 2.9, 2.15a). It is

not clear if we have a sampling problem due to unresolved local effects, poorly represented large scale wave dynamics, or some other problem. If we used the isopycnal displacements to determine the vertical velocity we could exactly represent the thermocline displacement but we could not determine if it was due to vertical velocity, lateral advection of the isopycnal surfaces, and/or turbulence. Lateral salt advection was also weak, but rather persistent (Fig. 2.20), and the average horizontal advective forcing resulted in a net freshwater loss of 6 ± 2 cm for the SML and 10 ± 5 cm for the 50 m layer; both tended to balance the net surface flux, $P-E = 11$ cm (Table 2.1).

2.5.4 Overall advection means for the IOP surveys

Time-averaged advective fluxes are summarized in Tables 2.3 and 2.4, and the average values of the net surface flux of heat and freshwater ($P-E$) are summarized in Table 2.1. Horizontal flux estimates are given for both the midscale (65km) and the large scale (130km) estimates of the horizontal gradients and except for the third survey period the estimates for these two scales are not significantly different (Table 2.3). In this third period, the mid- and large-scale estimates differ significantly only during the first four days (27-31 Jan) when the thermocline was very shallow and thus estimated gradients were strongly influenced by thermocline displacements associated with the internal tide and other internal waves. Given the similarity in the average advection results obtained with the two scale analyses we continue to discuss only the large-scale gradient.

Averaging over all three-cruise periods, the SML had nearly zero average horizontal heat advection ($-3 \pm 5 \text{ Wm}^{-2}$) with meridional cooling

being offset by zonal heating (Table 2.3). For the 50 m layer, meridional cooling was stronger than zonal warming so that the average horizontal heat advection was $-18 \pm 12 \text{ Wm}^{-2}$. Vertical heat advection for this layer averaged 6 Wm^{-2} (Table 2.3). The UOL was also subject to meridional cooling and zonal warming; the net horizontal cooling tended to be balanced by vertical warming and the average heat advection into the layer was $12 \pm 35 \text{ Wm}^{-2}$. Overall, horizontal heat advection tended to cool the upper ocean and vertical advection provided warming. For the three cruise period, the average rate of change of heat storage for the 50 m layer estimated from Figure 2.22 was $-17 \pm 9 \text{ Wm}^{-2}$; the estimated surface heat flux was 12 Wm^{-2} and the estimated heat advection in the 50 m layer was $-12 \pm 12 \text{ Wm}^{-2}$. This suggests that turbulent mixing and penetrative radiation may account for the $-17 \pm 15 \text{ Wm}^{-2}$ needed to balance the 50 m layer heat budget.

Meridional and zonal salt advection components both gave a positive net flux, which thus act to maintain the warm pool salinity by compensating for the large net precipitation (2-4 m annually) observed in the region (Philander, 1990). The equivalent freshwater loss from the SML was 25 cm, and for the 50 m layer it was about twice as much (Table 2.4). For the 50 m layer, horizontal salt advection was stronger on average than vertical advection by about a factor of 4. The long term salt balance in the 50 m layer appears to be largely determined by the horizontal advective loss of freshwater (-43 cm) and the surface input of freshwater, $P-E = 44 \text{ cm}$ (Table 2.1).

2.6 Discussion/Conclusions

In this study we estimated the upper ocean advective heat and salt fluxes for the three R/V Wecoma cruises of the TOGA-COARE IOP at $\sim 1.75^{\circ}\text{S}$, 156.0°E . Our advection estimates suggest that horizontal heat and salt advection in the warm pool can be as important as the net surface fluxes on time scales of days to months and that the role of the winds in deepening the mixed layer and in generating strong currents has a large impact on advection. The advective fluxes and the wind forcing tended to be episodic with time scales of 2 to 5 days. The meridional flux generally provided relatively cool and high saline water that dominated the zonal flux which generally had a warming and freshening influence. Large advective fluxes were not always coincident with the winds, however. Following the wind burst which ended on 3 Jan, the SML heat advection was small since the layer depth was very shallow, but strong cooling of $\sim -300 \text{ Wm}^{-2}$ due to meridional advection occurred for at least 5 days in the 50 m layer and in the UOL and was largely balanced by advective heating from zonal and vertical heat advection. This response appears consistent with equatorial downwelling in response to westerly winds with cooler water advecting from the south and warmer water from the west. The vertical structure of the dominant eigenmode suggests an Ekman spiral structure consistent equatorial convergence in response to westerly winds.

While the warm pool SML often appears to be thermally balanced in a one-dimensional sense (Anderson and Weller, 1996) the episodic nature and magnitude of the advective fluxes suggest that the one-dimensional view of the warm pool may be too simplistic for general use. Under low wind conditions, which is often the case in the warm pool (Philander,

1990), the SML is shallow and currents are modest so that heat advection in the SML is generally small and thus the local ocean-atmosphere response may be well represented by a one-dimensional model. Similarly, when the ocean is laterally uniform (as it was during W9211C) advection is small even though the SML has a deep diurnal cycle. However, heat advection in the SML can be considerable during and just after westerly wind bursts and other wind events (e.g. 23-25 Nov) that deepen the SML and generate sizable currents that when combined with the modest lateral gradients found in the warm pool give advective fluxes as large as $\pm 50 \text{ Wm}^{-2}$ for several days. Anomalous wind forcing appears to be an important link in understanding, not just the latent flux in the warm pool (Meyers et al., 1986), but also the advective flux. Rainfall during weak winds is also important in minimizing SML advection due to freshwater capping or shoaling of the SML to within a couple of meters of the surface (i.e. W9211B). Following the wind burst during W9211B freshwater capping played a significant role in shoaling the SML and thus minimized horizontal heat advection even though the horizontal temperature gradients and currents were large (Figs 2.2, 2.6). While our results suggest that heat advection in the SML is likely very important to the local heat budget on time scales of days to weeks, the three-cruise average result was nearly zero ($-3 \pm 5 \text{ Wm}^{-2}$) and is in agreement with the conventional view that the ocean and atmosphere in the warm pool region are in local thermodynamic balance (Niiler and Stevenson, 1982).

For the 50 m layer, horizontal advection provided cooling at an average rate of -18 Wm^{-2} and vertical advection warmed the layer at an average rate of 6 Wm^{-2} over the three Wecoma cruises. The three cruise mean estimate of horizontal heat advection in the 50 m layer is not small relative to the surface flux of $\sim 12 \text{ Wm}^{-2}$ (Table 2.1), or turbulent flux

estimates of -1 to -20 Wm^{-2} (Niiler and Stevenson, 1982; Godfrey and Lindstrom, 1989; Wijesekera and Gregg, 1995; Smyth et al., 1996b). Given that our advection estimates are over a limited temporal and spatial domain are they representative of the annual warm pool advective fluxes? Our 50 m layer horizontal heat advection results ($-18 \pm 12 \text{ Wm}^{-2}$) compare fairly well to estimates from a climatological model study of the equatorial Pacific Ocean heat balance (Enfield, 1986). Enfield used monthly climatological surface fluxes, wind stress, and SST over $10^\circ \times 10^\circ$ latitude-longitude boxes centered on the equator. For the box centered at 155°E , which includes our survey region, Enfield's estimate of annual horizontal advection for the 50 m layer was $\sim 0 \text{ Wm}^{-2}$ and the meridional diffusion was -8 Wm^{-2} . If we consider that for a model driven by monthly data, as opposed to \sim daily data resolution in our study, the diffusion time scale may nominally correspond to our "daily" sampling of advection. In other words, our advection estimate over the nominally 4 month period and the annual diffusion from the model are in fairly good agreement. This agreement further supports the idea that the episodic behavior of advective events dominate the mean advective response. The low frequency (\geq monthly) response in the gradients and currents is the not the dominant contributor to the mean advective flux. The relatively short time period events dominate the mean advective flux.

For all three survey cruises, the net horizontal salt advection was positive and generally the sign of the advective salt flux was positive in all three layers. Given the net surface freshwater flux into the ocean, salt must either be turbulently mixed into the upper ocean from below or advected into the region to maintain the warm pool salinity. Estimates of turbulent salt flux indicate that turbulent mixing of salt in the SML is very large but not sufficient to balance the salt budget (Smyth et al., 1996). The advection

estimates indicate that horizontal advection of salt was substantial compared to the surface flux. Given that the warm pool is a region of net precipitation of ~ 2 to 4 m yr^{-1} , our results suggest that horizontal salt advection is important in helping maintain the salinity of the warm pool.

The complete ocean heat and salt budget must be considered to understand what mechanisms are dominant and we have at least three case studies to consider. A detailed study of the budgets is the subject of a companion paper. The relative success of SST prediction on diurnal time scales by one-dimensional modeling efforts (Anderson and Weller, 1996) point to the strength of the diurnal signal and to the strong coupling of the SML to that signal, but over longer time scales of order days to one month the prediction is not so successful. What is clear from these surveys is that the warm pool heat budget near the equator is not appropriately characterized in a one-dimensional sense on time scales of weeks but over the longer term such characterization may be appropriate as the advection effects may average out.

Chapter 3

On the Evolution of the Western Equatorial Pacific Warm Pool during the TOGA COARE IOP: Heat and Salt Budgets

3.1 Abstract

Upper ocean heat and salt balances in the warm pool of the western equatorial Pacific Ocean are investigated for three R/V Wecoma cruise surveys for the period Nov 1992 to Feb 1993. Using data from the R/V Wecoma, R/V Moana Wave and the WHOI Upper Ocean Processes Group (UOP) mooring three upper ocean layers are considered: the surface mixed layer (SML), the 50 m layer, and the Upper Ocean Layer (UOL) extending from the sea surface to the $\sigma_\theta = 22.0 \text{ kg m}^{-3}$ isopycnal. This is the second of two closely related papers on the evolution of the upper ocean during the Intensive Observation Period (IOP, Nov 1992-Feb 1993) of the Tropical Ocean-Global Atmosphere (TOGA) Coupled Oceanic-Atmospheric Response Experiment (COARE). The first work (Chapter 2) provided details about the experimental sampling and estimates of heat and salt advection at 1.75°S , 156.0°E along with an overview of the oceanic and atmospheric conditions observed during each of the three R/V Wecoma IOP cruises.

Each of the Wecoma surveys occurred during unique atmospheric and oceanic conditions; calm winds with fairly clear skies (W9211A), strong westerly winds accompanied with strong atmospheric convection

(W9211B), and moderate north-westerlies punctuated by strong squalls (W9211C). The spectral response of the SML heat storage rate is well represented by linear trends over a few day to one week timescales and with a significant cooling peak occurring at the diurnal frequency. Over the three surveys, an average of 52 Wm^{-2} of radiant heat penetrated below the base of the SML and for each cruise the penetration of radiant energy was a major component of the net flux. By comparison, net surface and turbulent flux over the three surveys averaged only 14 and -11 Wm^{-2} , respectively, and advection was not significant in the three cruise average.

For all three layers, the role of advection in modifying the heat and salt content on time scales of days to months and spatial scales of $\sim 100 \text{ km}$ can be considerable with fluxes of over 100 Wm^{-2} observed for periods of days. Unlike the SML, the three cruise average horizontal heat advection was the largest term in the heat budget for the 50 m layer during W9211B and for the three cruise mean budget. Further, salt advection appears to be important in maintaining the warm pool salinity and suggests that ocean circulation may be important to the long term warm pool thermohaline response. The role of the winds in driving equatorial ocean dynamics appears to be an important link in predicting upper ocean heat and salt advection.

Our findings indicate that the role of penetrative radiation must be well accounted for in models of the surface mixed layer and the upper 50 m layer. The upper ocean thermal response of the warm pool cannot be accurately modeled as a simple one-dimensional system over day to month time scales as horizontal and vertical advection can be significant over those time scales but over longer times heat advection in the SML tends average to zero. The significance of salt advection in our budgets suggests that the warm pool saline variability depends on the input of salt from

ocean circulation and cannot be modeled as a simple one-dimensional system. There are periods, however, when the advective response is weak and one-dimensional models may be adequate.

3.2 Introduction

This is the second of two closely related papers on the evolution of the thermohaline structure of the warm pool in the upper western equatorial Pacific Ocean during the Intensive Observation Period (IOP, Nov 1992-Feb 1993) of the Tropical Ocean-Global Atmosphere (TOGA) Coupled Oceanic-Atmospheric Response Experiment (COARE). The first work (Chapter 2) provided details about the experimental sampling and estimates of heat and salt advection at 1.75°S , 156.0°E (Fig. 2.1) along with an overview of the oceanic and atmospheric conditions observed during each of the three R/V Wecoma IOP cruises. In this work we focus on closing upper ocean heat and salt budgets at the center of the COARE butterfly using data from the R/V Wecoma, R/V Moana Wave and the WHOI Upper Ocean Processes Group (UOP) mooring, and the advection estimates from chapter 2. Closure of the heat and salt (freshwater) budgets are necessary steps in validating the estimated fluxes and understanding the processes that modify sea surface temperature (SST) and drive the ocean-atmosphere system (WCRP, 1990; Webster and Lukas, 1992). These three case studies provide insight into the air-sea interaction and upper ocean evolution in the warm pool on day to month time scales.

The western Pacific warm pool is a region of considerable interest to climate researchers because it has the highest annual atmospheric heating

rates and is responsible for setting global atmospheric temperature gradients (Webster and Lukas, 1992). The warm pool's migration and temperature response has long been recognized as an integral component of the El Niño-Southern Oscillation (ENSO) cycle (Bjerknes, 1966; Rasmusson and Carpenter, 1983) which is known to affect weather patterns on global scales (Bjerknes 1969; Horel and Wallace, 1981). Interestingly however, the warm pool and its overlying atmosphere have been thought to be largely in local thermodynamic balance with net surface flux being mostly balanced by vertical turbulent diffusion into the ocean interior (Niiler and Stevenson, 1982). Climatological estimates of net surface flux into the ocean range from 20 to 80 Wm^{-2} (Esbensen and Kushnir, 1981; Weare et al., 1981) with the large incident radiation term being largely offset by latent heat loss from the ocean surface. Recent estimates of turbulent heat loss from the warm pool into the ocean interior range from -1 to -20 Wm^{-2} (Godfrey and Lindstrom, 1989; Wijesekera and Gregg, 1996; Smyth et al., 1996b). These estimates of net surface heat flux and vertical turbulent diffusion do not readily balance and suggest that either the results are not representative or some other process may be important to the overall heat balance. While it is well known that the atmosphere is largely responsible for the export of heat away from the western Pacific equatorial region (Philander, 1990) ocean circulation and mixing, as well as penetrative radiation, may be important to the long term heat storage variability for the upper ocean layers.

Some studies of ocean circulation processes indicate that they may contribute -10 to -20 Wm^{-2} cooling annually to the upper ocean in the warm pool. Enfield (1986) used a model driven by monthly surface wind and heat flux climatologies and estimated that ocean processes (advection + turbulent diffusion) provide a cooling rate of $\sim -8 \text{ Wm}^{-2}$ in the western

equatorial Pacific. More recent work from atmospheric heat budgets for the IOP (Ramanathan, 1995) estimated that upper ocean processes (advection + turbulent diffusion from the mixed layer) provide cooling at -10 to -20 Wm^{-2} annually. A net cooling of 10 Wm^{-2} would lower the upper 50 m layer temperature by $\sim 0.8^\circ\text{C yr}^{-1}$, which is considerable considering that the SST anomaly for a composite ENSO event in this region is less than 0.5°C (Rasmusson and Carpenter, 1983). This points to the importance of relatively small fluxes and their associated uncertainties to the long term heat storage. Such considerations motivated the strong desire to have ocean heat budgets close to within 10 Wm^{-2} for the COARE IOP (Webster and Lukas, 1992).

What are the dominant heat and salt fluxes in the warm pool? Is there a local heat balance between the ocean and atmosphere in the warm pool? Over what time and space scales do the individual fluxes contribute? What is the depth dependence of the response? To understand the exchange of heat and moisture between the ocean and atmosphere it is useful to close the ocean heat and salt budget over a variety of upper ocean layers which may represent different scale interactions and/or processes. Three depth layers were considered in this study: the surface mixed layer (SML) {defined as the depth, h_{sml} , where the potential density (σ_θ) first exceeds the surface density value by 0.01 kg/m^3 (Moum, 1989; Brainerd and Gregg, 1994)}, a 50 m fixed depth layer (h_{50}), and the Upper Ocean Layer (UOL) defined from the surface to the depth of the $\sigma_\theta = 22.0 \text{ kg/m}^3$ isopycnal (h_{uol}) which often coincided with the top of the thermocline. We attempt to quantify the exchanges of heat and moisture from the upper ocean at $\sim 1.75^\circ \text{S}$, 156.0°E for each of the three layers described above during the Wecoma cruises of the TOGA COARE IOP.

Given the limited spatial and temporal coverage of oceanic observations, one-dimensional heat and salt budgets are often attempted with advection being estimated from the budget residual (Wijesekera and Gregg, 1996; Smyth et al., 1996b; Anderson and Weller, 1996). This one-dimensional budget approach may be very effective provided the measured fluxes and oceanic heat and salt storage estimates are accurate and representative. Surface and turbulent flux estimates, however, often have substantial uncertainties and the ocean and atmosphere are generally not spatially homogeneous so that even accurate point estimates of the fluxes and ocean storage rates may not be representative.

In our budget studies we estimated the cruise mean budgets and looked for correlation between the flux and storage rate time series. In other words, given the large background geophysical noise, e.g. internal waves, we found that mean budget results could be very sensitive to averaging but the summed fluxes and the rate of change in storage may not be well correlated in time. During TOGA COARE, observations were made that provide direct estimates of the heat and salt storage rates as well as direct estimates of the advection, turbulent, and surface fluxes over a relatively wide spatial area so that three-dimensional budget closures may be attempted.

As summarized in chapter 2, the vertically integrated ocean heat and salt budgets can be written as,

$$\rho c_p \int_{-h}^0 \frac{\partial T}{\partial t} dz = -\rho c_p \int_{-h}^0 (\vec{u} \cdot \vec{\nabla} T) dz + Q_s + Q_p + Q_t \quad (3.1)$$

and,

$$\int_{-h}^0 \frac{\partial S}{\partial t} dz = -\int_{-h}^0 (\vec{u} \cdot \vec{\nabla} S) dz + Q_{ns} + (E - P)S_o \quad (3.2)$$

where the Q_s , Q_p , and Q_t represent the surface, penetrative radiant, and turbulent heat flux contributions, respectively, to the local heat budget and Q_{ts} and $(E-P)S_o$ represent the turbulent and surface salt fluxes for the salt budget.

The remainder of this paper is organized as follows. In section 2 we summarize the observations used for the budget analysis. Section 3 briefly describes our methods, including a spectral approach for estimating the change in the rate of heat and salt storage. In section 4, the budget results for each cruise and the three cruise average is detailed. We provide a discussion and conclusions of our findings in section 5. Appendix C provides a discussion of estimating heat and salt storage terms using spectral methods and Appendix D gives a summary of the budget error estimates.

3.3 Observations

Below we describe the observations used in three case studies of the heat and salt budgets at $\sim 1.75^\circ\text{S}$, 156.0°E corresponding to the three R/V Wecoma survey periods (W9211A 14 to 30 Nov, 1992; W9211B 21 Dec to 8 Jan, 1993; W9211C 28 Jan to 15 Feb, 1993) of the COARE IOP.

3.3.1 Turbulent fluxes at the base of surface layers

The R/V Moana Wave conducted three survey cruises that coincided approximately with the R/V Wecoma survey cruises but the

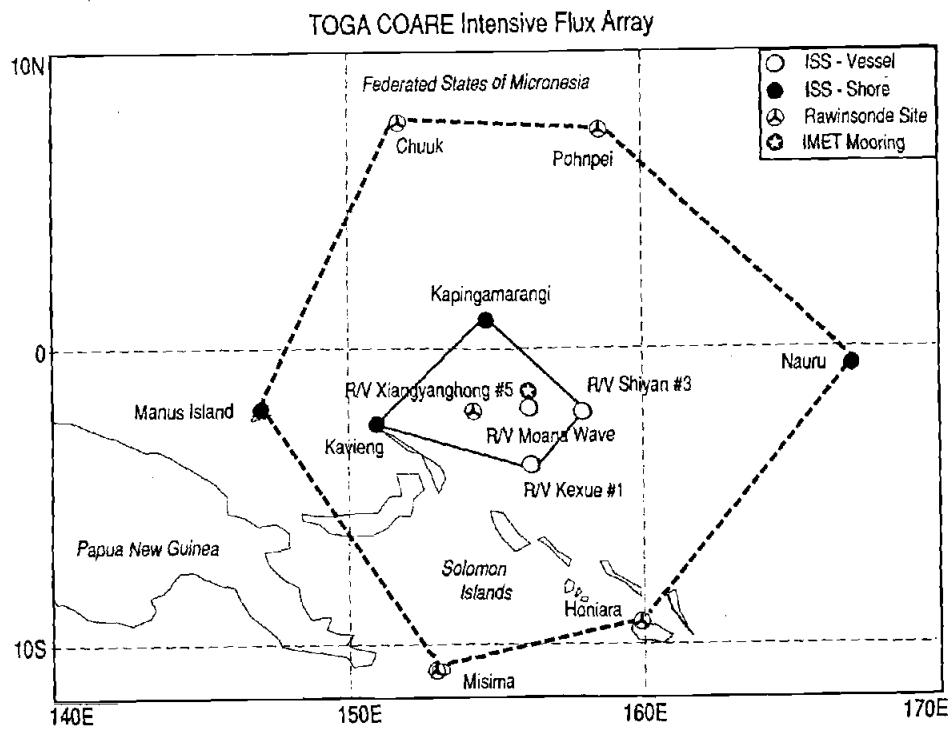


Figure 3.1a The location of the TOGA COARE sampling domain showing location of islands and principal stationary ships (reproduced from the TCIPPO Operations Summary, 1993).

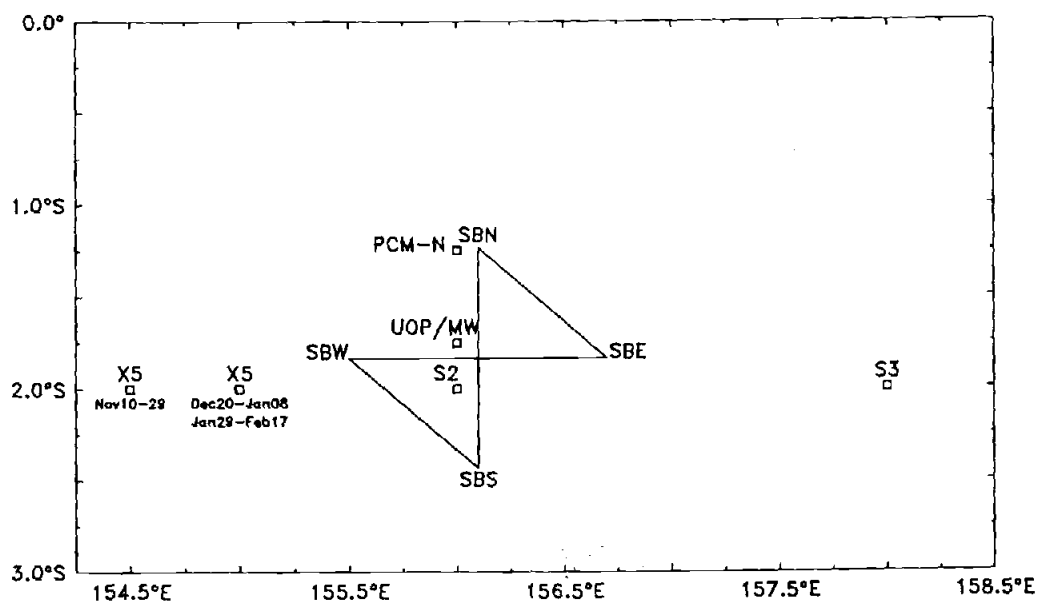


Figure 3.1b An expanded view of the center of the Intensive Flux Array, showing the butterfly pattern sampled repeatedly by R/V Wecoma and the location of the stationary platforms used in this study: UOP mooring, Profiling Current Meter mooring (PCM-N), the S2 mooring, R/V Moana Wave (MW), R/V Xiangyanghong#5 (X5), and R/V Shiyan#3 (S3).

oceanographic sampling on each cruise was performed by different scientific teams each using unique instrumentation. During the first two cruises (6 Nov- 6 Dec, 1992; 17 Dec, 1992 - 11 Jan, 1993) Moana Wave remained within 10 km of the WHOI Upper Ocean Processes Group (UOP) mooring at 1.75°S, 156.0°E (Fig. 3.1b) while frequently sampling (3 - 6 times/hour) the upper ocean thermohaline structure. On the third cruise, sampling was much less frequent (4 - 5 times/day), and the ship remained near the UOP mooring only from 29 Jan to 5 Feb, 1993. On the first Moana Wave cruise, the Advanced Microstructure Profiler (AMP) was used to measure the upper ocean temperature, salinity, and microstructure from 2.0 - 225 m (Wijesekera and Gregg, 1995). On the second cruise CHAMELEON was used to measure temperature, salinity, and microstructure from ~ 3.0 - 250 m (Smyth et al., 1996a,b). Both AMP and CHAMELEON have a vertical resolution of ~ 0.1 m. Hourly values of h_{smL} and h_{uol} as well as temperature, salinity, and turbulent heat and salt fluxes calculated from microstructure observations were provided in 4 m bins by H. Wijesekera for W9211A and by W. Smyth for W9211B. For both cases, microscale shear data was used to construct estimates of turbulent dissipation to calculate the turbulent eddy coefficients K_T and K_S for heat and salt, respectively, assuming that they are equal to the turbulent eddy coefficient for density, i.e. $K_\rho = K_T = K_S$ (Wijesekera and Gregg, 1996; Smyth et al., 1996b). The turbulent heat and salt flux estimates are accurate to about a factor of 2 (Smyth et al., 1996b). Turbulence data is not available for W9211C and thus it is a component of the budget residual.

The R/V Wecoma conducted three survey cruises (W9211A,B,C) and on each cruise a towed undulating Seasoar CTD system and a hull mounted RD Instruments Acoustic Doppler Current Profiler (ADCP) were used to sample the upper ocean thermohaline and current structure as

continuously as possible along a simple butterfly pattern (Fig. 3.1b) with zonal and meridional sections extending 72 nautical miles (130 km). The final processed Seasoar CTD data set consists of 1-sec averages of temperature (T) and salinity (S); these data have a horizontal resolution < 3 km and a vertical resolution of ~2 dbar. The temperature, salinity and pressure accuracy are believed to be $\pm 0.01^{\circ}\text{C}$, ± 0.01 psu and ± 1 dbar, respectively. Some partial Seasoar sections were completed using conventional CTD casts spaced every 10 km (Huyer et al., 1997). The ADCP (model VM-150) recorded ensemble averages every 2 minutes and acquired the current data in 8 m bins using a 16 m (8 m) pulse length during W9211A (W9211B,C). The raw ADCP data was calibrated, processed and provided by E. Firing and P. Hacker (both at U. Hawaii) and the final processed data are accurate to better than 0.02 ms^{-1} over horizontal scales greater than 10 km. We gridded the ADCP data and Seasoar CTD data onto a common spatial grid with 8.3 m depth (length of bin has been adjusted for the speed of sound) and 4 km horizontal bins using a 16 m triangle filter in the vertical on the CTD data to match the response of the ADCP (RD Instruments, 1990). We then used this data to calculate the gradient Richardson number (Ri) along the Wecoma transects to use as a qualitative indicator of local mixing. We attempted to quantify the along track turbulent fluxes using a Ri flux parameterization (Peters et al., 1988) but the magnitudes of the fluxes were not consistent with the direct microstructure observations from the Moana Wave.

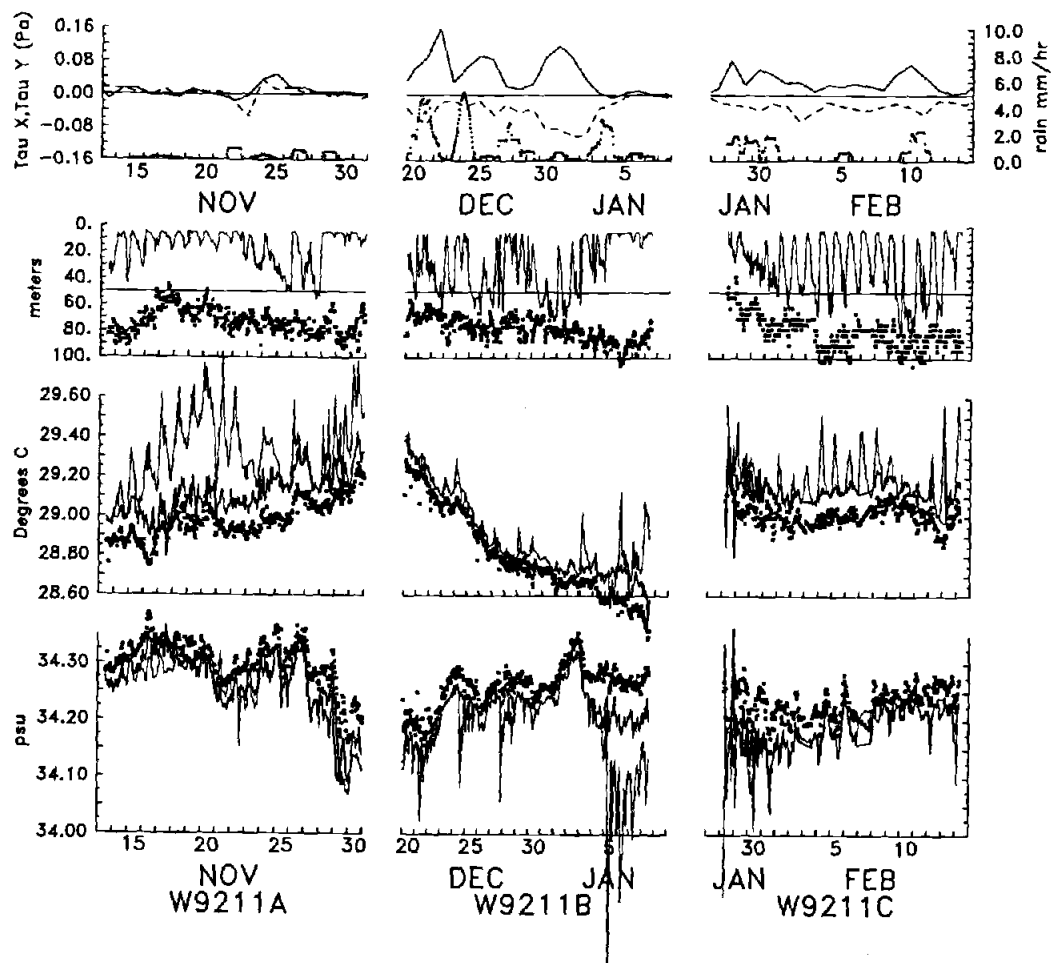


Figure 3.2 Time series of wind stress, rainfall, SML depth, UOL depth, SML, 50 m layer, and UOL temperature and salinity. Panel 1: Daily averaged wind stress and rainfall from the central UOP mooring. Panel 2: Hourly layer depths: SML (solid), 50 m (dashed), UOL (squares). Panel 3: Hourly values of the average layer temperatures: SML (solid), 50 m (dashed), UOL (squares). Panel 4: Hourly average layer salinity: SML (solid), 50 m (dashed), UOL (squares).

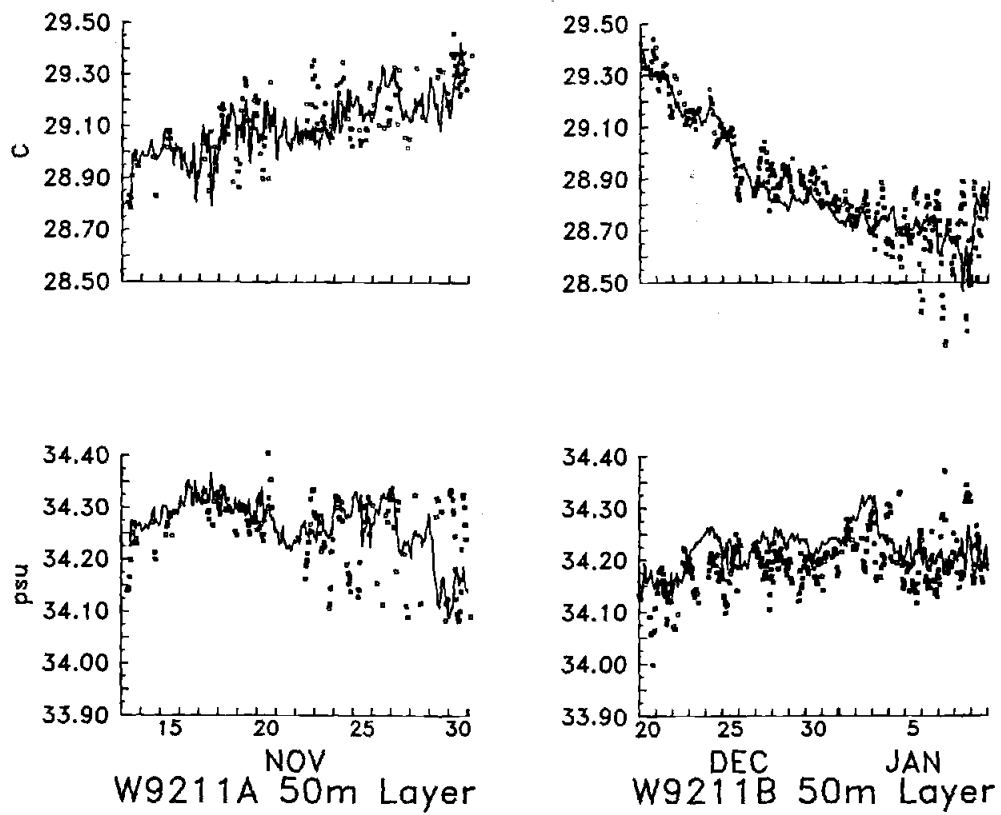


Figure 3.3 Hourly 50 m layer temperature (upper panels) and salinity (lower panels) from the R/V Wecoma (squares) and R/V Moana Wave (solid black).

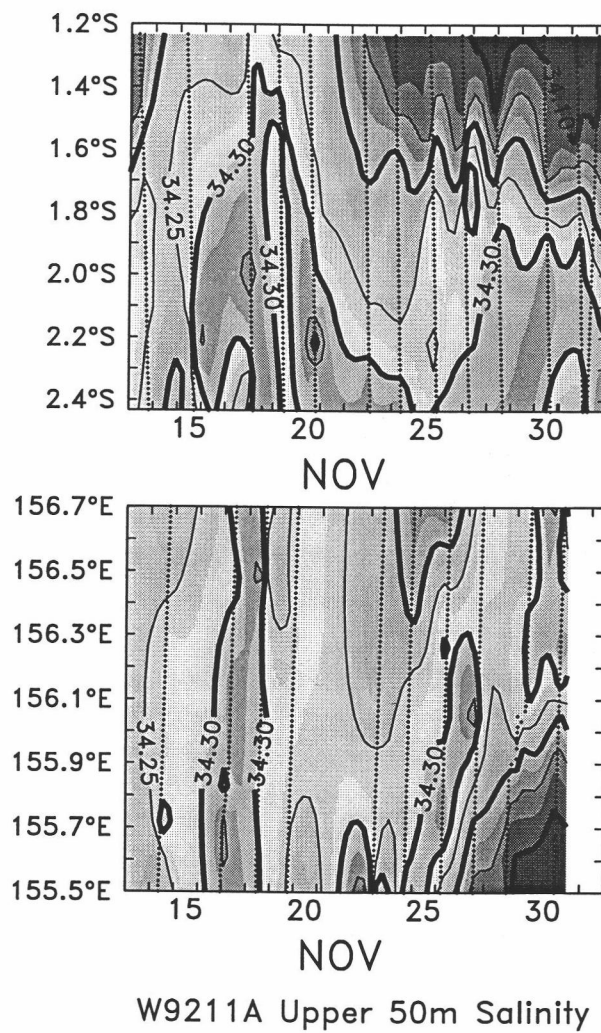


Figure 3.4a Time-latitude and time-longitude plots of the 50 m layer salinity from Wecoma for W9211A.

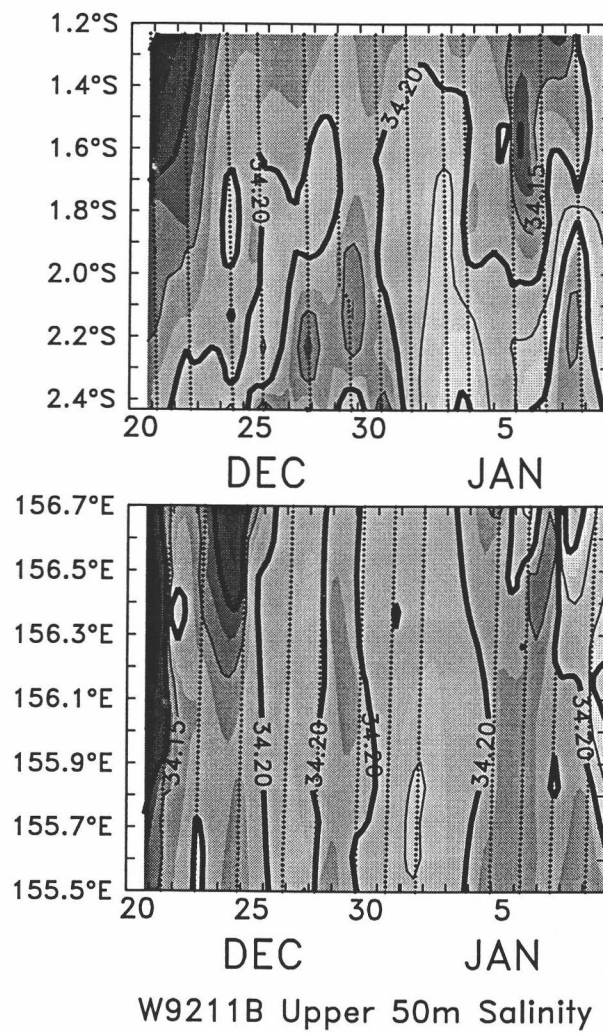


Figure 3.4b Time-latitude and time-longitude plots of the 50 m layer salinity from Wecoma for W9211B.

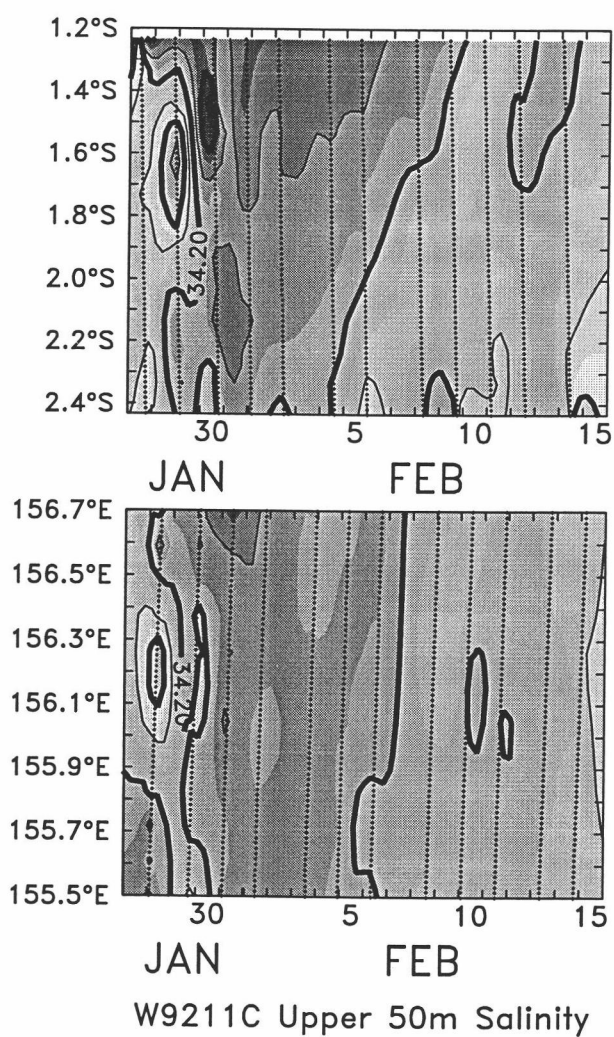


Figure 3.4c Time-latitude and time-longitude plots of the 50 m layer salinity from Wecoma for W9211C.

3.3.2 Storage rates of heat and salt

The storage rates of heat and salt were estimated using CTD data from the R/V Moana Wave during W9211A and W9211B and the R/V Wecoma for W9211C. Because Moana Wave did not maintain station at the central point for most of W9211C, we used the Wecoma 2-dbar gridded Seasoar data to make hourly estimates of the temperature and salinity storage variability as well as the SML and UOL depths. Some short gaps, not exceeding 18 hours, in the Seasoar temperature and salinity data were filled with linear interpolation. Gaps in the SML data were filled with UOP mooring data (provided by M. Baumgartner, WHOI; Anderson and Weller, 1996) and linear interpolation was used to fill the gaps in the 50 m and UOL time series. Hourly values of the vertically averaged temperature and salinity are shown in Fig. 3.2. During W9211C, the upper ocean was fairly homogeneous (chapter 2) so that the Seasoar data along the butterfly pattern is representative of the center point temperature and salinity.

The use of the Wecoma data to compute horizontal temperature and salinity gradients has been previously described (chapter 2) but here we also use the Wecoma data to provide a spatial context/representation of the heat and salt storage rates and compare it to the point like representation from the Moana Wave data described below. For the first two cruises we calculated the average 50 m layer temperature and salinity along the butterfly pattern in hourly bins for comparison with the Moana Wave results (Fig. 3.3). Also, we constructed time-latitude and time-longitude maps of the vertically averaged 50 m salinity to determine the relative homogeneity of the ocean (Figs. 3.4a,b,c).

3.3.3 Surface heat fluxes

The R/V Wecoma, R/V Moana Wave, and the UOP mooring were outfitted with various suites of meteorological and near surface temperature and salinity sensors. The basic observed meteorological variables were wind velocity, relative humidity, air temperature, barometric pressure, incoming shortwave radiation, incoming longwave radiation, rain rate, rain temperature, and sea surface temperature. The R/V Moana Wave also made atmospheric eddy flux measurements for estimating latent heat fluxes (Fairall et al., 1996).

Hourly surface fluxes including shortwave and longwave radiation, latent heat, sensible heat and rainfall were provided by our colleagues: C. Paulson (Wecoma, manuscript in prep.), H. Wijesekera (Moana Wave, Wijesekera and Gregg, 1996), W. Smyth (Moana Wave, Smyth et al., 1996a,b), and R. Weller (UOP Mooring, Weller and Anderson, 1996). For more details concerning the operation and capability of the instruments please see the cited references. Given the continuing effort to refine the surface flux estimates we note that the surface fluxes used in this manuscript were estimated using version COARE 2.5 of the bulk flux algorithm developed for the TOGA COARE IOP by Fairall et al. (1996).

A series of flux inter-comparisons completed for the IOP show that cruise averaged surface fluxes agreed within 10 Wm^{-2} (Weller and Anderson, 1996). Even though the three platforms had good agreement over each cruise period the comparison of the surface fluxes from the three platforms over the periods that budgets were completed for this study showed slightly larger disagreement (Table 3.1). The Wecoma shortwave flux is markedly larger by $\sim 15 \text{ Wm}^{-2}$ during W9211B and W9211C which may represent spatial variability in cloud coverage. The UOP mooring

surface heat flux time series (Fig. 3.5) is used as a reference as it was centrally located for all three Wecoma cruises. The Wecoma and Moana Wave flux data are likely of higher quality and thus the three platform estimates provide an estimate of the average flux over the domain and an estimate of the uncertainty associated with spatial variability and measurement error of the surface fluxes. Also the three-platform average provides a more reliable flux estimate because the ocean "calorimeter" that we are studying essentially has horizontal sides of ~ 100 km as dictated by the scale of the advection flux estimates (chapter 2).

3.3.4 Surface freshwater fluxes

Obtaining reliable precipitation flux estimates has been an elusive goal because of the considerable disagreement between the various surface measurements of 30% or more (Table 3.2) and a disagreement of a factor of 2 between radar and surface measurements (Short et al., 1996; Bradley and Weller, 1996). This budget study will hopefully provide some insight into which measurements are correct. We note that Feng et al. (1998) have found closure of the 50 m and UOL freshwater budget for the period 20 Dec to 8 Jan, 1993 to within 20% of the Moana Wave and Wecoma optical rain gauges. In this study we will review the fluxes obtained from the three surface platforms in the context of the budgets to estimate an upper and lower bounds for the precipitation estimates. Again, we used the UOP mooring precipitation time series as a reference noting that the mooring data represents a blend of the Wecoma, Moana Wave, and UOP mooring data as well as rain data from an Atlas mooring at 2° S, 156° E (Weller and Anderson, 1996). Moana Wave precipitation data may be more reliable

than the UOP mooring data (Paulson, pers. comm.) and we will consider this point in the context of the budgets. Note that the average of the three platform surface freshwater flux is almost exactly the same as the Moana Wave data for W9211B (Table 3.2) during which the most rainfall occurred. The evaporative flux was calculated from the latent heat flux using a latent heat of vaporization of 2.43 MJ kg^{-1} .

3.3.5. Penetrative radiant flux

Given the relatively clear surface waters of the warm pool, penetration of radiant heat below the base of the mixed layer can be considerable. To estimate the penetrative flux we used a double exponential relation proposed by Siegel et al. (1995),

$$\text{Tr}(z) = 0.945 I_0 [0.62 \exp(z/2.86) + 0.38 \exp(z/22.2)] \quad (3.3)$$

where $\text{Tr}(z)$ is the transmitted radiant flux at depth z . The coefficient 0.945 accounts for the sea surface albedo, I_0 is the incident shortwave flux, the first exponential represents the longwave response with an extinction coefficient of $(2.86)^{-1} \text{ m}^{-1}$ from Paulson and Simpson (1977) and the second exponential represents the shortwave response with an extinction coefficient of $(22.2)^{-1} \text{ m}^{-1}$ determined by Siegel et al. (1995). The shortwave coefficients used in this equation were determined from 100's of shortwave transmission profiles made during the COARE IOP. Given that the transmission profile is based on measurements of the spectral range 340 to 683 nm it underestimates the radiant flux associated with longer

Table 3.1 Surface heat flux comparisons between each platform and for each component of the surface flux.

Heat Flux (Wm^{-2})	W9211A (319.50-335.50)			W9211B (356.68-374.52)			W9211C (394.28-411.24)		
	R/V Moana Wave	R/V Wecoma	UOP IMET	R/V Moana Wave	R/V Wecoma	UOP IMET	R/V Moana Wave	R/V Wecoma	UOP IMET
Shortwave	219	221	220	156	177	158	185	200	185
Longwave	-62	-59	-63	-50	-54	-52	-57	-61	-56
Latent heat	-84	-80	-87	-122	-123	-119	-109	-132	-135
Sensible	-6	-4	-7	-7	-8	-9	-8	-12	-9
Net Surface flux	68	76	63	-23	-8	-22	11	-4	-15
Range			13			15			11*
Avg. Surface flux†			69±7			-18±8			-10*±6

*Moana Wave data excluded from W9211C range and average because the ship was in the butterfly domain for only 5 of the ~ 17 days for which the budget is estimated.

†Error bars are estimated using the range divided by two and the result is then rounded to a whole number.

Table 3.2 Comparison of the surface freshwater flux estimates from each platform.

Freshwater (cm accum)	W9211A (319.50-335.50)			W9211B (356.68-374.52)			W9211C (394.28-411.24)		
	R/V Wave	R/V Wec.	UOP ^a IMET	R/V Wave	R/V Wec.	UOP ^a IMET	R/V Wave	R/V Wec.	UOP ^a IMET
Precipitation	7.3	2.7	7.2	30.8	20.3	41.6	ND	7.6	20.3
Evaporation	5.6	5.2	5.2	8.5	8.6	8.3	ND	8.6	8.6
P-E (Net flux)	1.7	-2.5	2	22.3	11.7	33.3	ND	-1	11.7
Range			4.5			21.6			12.7
Avg. P-E			0.4 ± 2.3			22.4 ± 10.8			5.4 ± 6.4

^a The UOP rain result is a blend (Weller and Anderson, 1996) from the three platforms plus data from the Atlas mooring at 2°S, 156°E.

[†] Error bars are estimated using the range of the three estimates that is then divided by two.

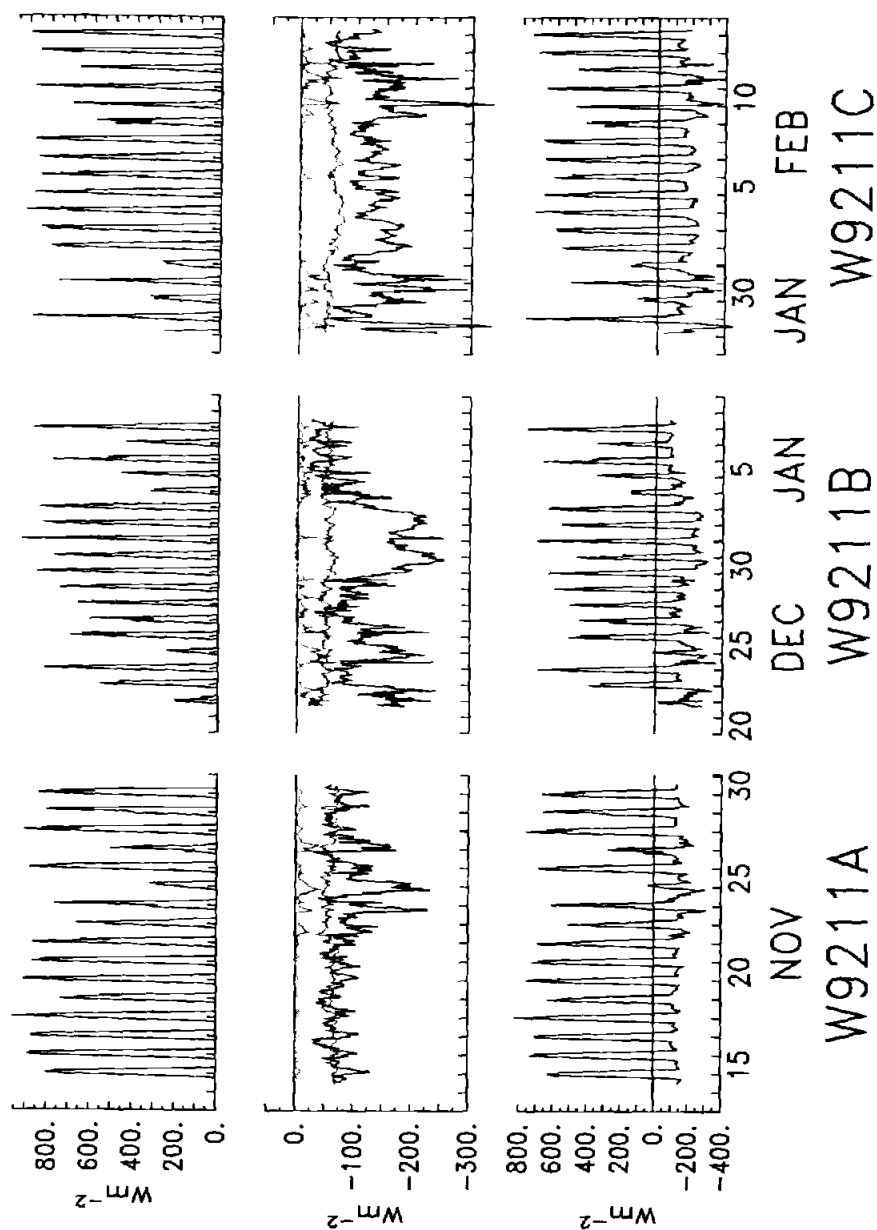


Figure 3.5 Hourly averaged surface heat fluxes from UOP mooring. Upper panels: Incident shortwave radiant flux. Center panels: Sensible heat flux (medium gray line), latent heat flux (dark line), and net longwave radiation (light gray line). Lower panel: Net surface flux. Note that Table 1 provides cruise average results for each platform.

wavelengths at shallow depths so that $Tr(z)$ is considered to be valid only below ~ 10 m with the error growing as the depth decreases. At 5 m and 1 m the transmission profile underestimates the penetrative term by roughly 3% and 10%, respectively and depends on solar zenith angle and cloud cover (C. Ohlmann, pers. comm). This translates to an underestimate of ~ 5 to 20 Wm^{-2} in the daily averaged penetrative flux assuming a typical diurnal cycle of the SML depth under light winds. The transmission profile is also affected by changes in phytoplankton pigment concentrations which reduced the average penetrative radiation flux by $\sim 5 \text{ Wm}^{-2}$ at 30 m during to a phytoplankton bloom following the December Westerly Wind Burst (Siegel et al., 1995). We have adopted an uncertainty of $\pm 10 \text{ Wm}^{-2}$ in the penetrative estimate for the SML and a 20% error estimate for the 50 m and UOL layers. The motivation for choosing the 20% error estimate comes from the range in the incident shortwave radiation (as much as 21 Wm^{-2}) between the observing platforms and uncertainty about the relative clarity of the water, e.g. phytoplankton. In practice, 20 % of the 50 m penetrative term is $\sim 2 \text{ Wm}^{-2}$.

3.3.6 Advective fluxes

Wecoma Seasoar data was used to determine the horizontal temperature and salinity gradients in the SML, the 50 m layer, and the UOL and combined with currents from the UOP mooring to estimate horizontal advection in those layers (chapter 2). Vertical advection was estimated by combining estimates of vertical temperature and salinity gradients obtained from Wecoma Seasoar and Moana Wave CTD data with

vertical velocity calculated from horizontal flow divergence using current data from four well separated platforms (chapter 2).

3.4 Analytical Methods

The time derivative in the heat and salt storage rates for the 50 m layer (left hand side of Eqns. 3.1 and 3.2) was calculated using centered differences in time from hourly-4m binned temperature and salinity data. The time derivative estimates were then vertically integrated from 0 to 50 m to obtain the storage rates. A similar approach is used fo the UOL. For the SML, we recast the left hand side of Eqns. 3.1 and 3.2 using Leibniz' rule,

$$\int_{-h}^0 \frac{\partial T}{\partial t} dz = h(t) \frac{\partial T_a}{\partial t} + (T_a - T_{-h}) \frac{\partial h}{\partial t} \quad (3.4)$$

and a similar result is obtained for salinity. Writing the left hand side of Eqns. 3.1 and 3.2 as shown in Eqn 3.4 allows the use of the traditional center differences in time approach as well as a spectral correlation estimate to calculate the storage rates as a function of frequency as detailed below. In the first method, the time derivative of the average layer temperature, T_a , and salinity, S_a , is estimated using centered differences in time which are then multiplied by $h(t)$ evaluated at the center time. We note that the second term on the RHS in Eqn. 3.4 is negligible in the mean. In the second method we calculate the storage term as a zero-lagged cross correlation in the spectral domain and avoids estimating an explicit discrete derivative in the time domain. This latter method also provides

information about the heating and cooling frequency response of the SML. For example, the correlated diurnal and semidiurnal temperature and SML depth responses can be analyzed (Appendix C). Also, the spectral estimate may be superior to the temporal estimate because time derivatives from "noisy" data may be a significant underestimate of the true derivative and therefore underestimate the correlation between $h(t)$ and $\partial T_a / \partial t$ or $\partial S_a / \partial t$ (Appendix C).

We can write the first term on the right hand side of Eqn 3.4 as,

$$\left\langle h(t) \frac{\partial T_a}{\partial t} \right\rangle = \sum_j^{\frac{N}{2}+1} \text{Re}\{G_{xy}(\omega_j)\} \Delta\omega_j + DC = 2\pi \sum_j^{\frac{N}{2}+1} \omega_j \text{Re}\{iG_{xy}(\omega_j)\} \Delta\omega_j + DC \quad (3.5)$$

where $x = h(t)$ and $y = T_a(t)$. Note that the right hand side of Eqn. 3.5 is a function of the cross-spectral density, $G_{xy}(\omega_j)$, of $h(t)$ and $T_a(t)$, and not the cross-spectral density of $h(t)$ and $\frac{\partial T_a}{\partial t}$. The angle brackets denote a time

averaged result. When using the spectral approach a "DC" or zero frequency component must be added to the sum to account for the detrending of the time series that must be performed to compute the cross-spectral estimate. In practice the cross correlation was calculated by breaking the time series up into N 64 hour segments which are detrended and the trend of each segment is used as the estimate of the "DC" time derivative of that segment which is multiplied by the average layer depth for that segment. The N segment "DC" storage rate values are then averaged to obtain the average "zero" frequency contribution to the storage rate. We can also estimate confidence intervals for the spectral estimates using the variance of the quadrature spectral density, Q_{xy} (Appendix C).

Note that we can write an analogous expression for the term $\langle (T_a - T_h) \partial h / \partial t \rangle$ and thus express the time-averaged left hand side of Eqn. 3.4 as,

$$\begin{aligned} \langle h(t) \partial T_a / \partial t \rangle + \langle (T_a - T_h) \partial h / \partial t \rangle = \\ 2\pi \sum \omega_j \operatorname{Re}\{iG_{xy}(\omega_j)\} \Delta\omega_j + 2\pi \sum \omega_j \operatorname{Re}\{iG_{xz}(\omega_j)\} \Delta\omega_j + \\ DC_{xy} + DC_{xz} \end{aligned} \quad (3.6)$$

where $z = T_a(t) - T_h(t)$ and where we have omitted the limits on the summations. The second term on the right hand side of Eqn. 3.4 is, however, negligibly small for the SML so instead we simply use Eqn. 3.5.

Both the time domain and spectral domain approach give null results for variability at the Nyquist frequency, $(2 \text{ hrs})^{-1}$. Spectral methods are valid for periodic stationary time series and as can be seen by reviewing the time series of $h(t)$ and $T(t)$ (Fig. 3.2) we are working marginally within these assumptions. For $S(t)$, it appears that neither approach may work for the SML salt storage rate. The problem of estimating the budget over a variable depth may be ill-posed given noisy non-stationary data. If the temperature and salinity time series are reasonably smooth regardless of stationarity, the time discretized approach may be more reliable and when the time series are "noisy" but stationary, the cross-spectral method may be more reliable. Tables 3.3a,b summarize the comparison of the heat and salt storage terms from the two methods. In general, the spectral and time difference estimates of the heat and salt storage rate for the SML are in good agreement with each other. The UOL budget requires some additional consideration because, unlike the SML, large temperature and salinity gradients exist at the layer base such that heat and freshwater storage rates associated with changes in depth may be

very large. The hour to hour variation of the UOL heat storage rates was generally greater than $\pm 2000 \text{ Wm}^{-2}$ so that a storage rate calculation requires long term averaging to achieve good estimates of the mean. Estimates of the standard error for the SML and UOL mean heat storage rates are greater than 100 Wm^{-2} and 1000 Wm^{-2} , respectively. Standard error estimates based on Gaussian statistics, however, are not appropriate for variables with strong sinusoidal-like dependences as observed in the case of $T(t)$ and $h(t)$. The large variability associated with the storage in the UOL layer makes comparisons with calculated fluxes problematic and poses significant problems for closing budgets for this layer over the relatively short cruise survey periods of ~ 17 days. Also, we do not have an independent way of estimating lateral advection of the layer depth. Essentially our analysis is noise limited and to some extent sample limited for this layer. As an alternative, we could exclude our estimated vertical advection from the flux balance and let the budget residual represent vertical advection within the layer and vertical entrainment/detrainment at the layer base that is not associated with turbulence. In this case, vertical advection/entrainment as well as errors in the other fluxes would be included in the residual. This approach is not very satisfying or revealing but it results in a balanced budget. It is essentially the same as assuming that changes in the layer depth are due to vertical velocity only so that vertical velocity can be determined using isopycnal displacements. This approach would likely work well for layers that have weak turbulent mixing and weak lateral gradients in depth but the UOL during the COARE IOP does not seem to fit these criteria. We can at least compare the implied vertical entrainment flux with the estimated vertical advection.

The other terms of the heat and salt budgets have been described in the introduction and observations section. Given the Wecoma sampling

plan, the temporal variability of the advection estimates is ~ 32 hours and for comparison plotting purposes the surface fluxes and storage terms, as appropriate, have been filtered at 32-hours. A comparison of the low passed summed flux time series and storage rate for the 50 m layer budgets is shown in figures 3.6 and 3.7. Finally, we note that it is useful to express the salt flux in terms of an equivalent freshwater flux for making direct comparisons with surface forcing. The salinity flux increases the layer salinity by $\Delta S = (Q_s/h) \Delta t$, where Q_s is a given salinity flux, h is the average layer depth, and Δt is the time over which the flux acted. For an average layer salinity, S_a , the salt flux is equivalent to a freshwater flux given by, $\Delta(\text{fw})/\Delta t = -Q_s/S_a$ so that the accumulated gain or loss of freshwater is given by, $\Delta(\text{fw}) = -Q_s \Delta t/S_a$ (Tables 3.3b, 3.5).

3.5 Heat and Salt Budgets

The R/V Wecoma surveys provide an opportunity to study the dynamics of the warm pool under three markedly different atmospheric forcing regimes: calm winds with fairly clear skies (W9211A), strong westerly winds accompanied with strong atmospheric convection (W9211B), and moderate north-westerlies punctuated by strong squalls (W9211C). In the following sub-sections, we will examine the heat and salt budget for each R/V Wecoma survey. Given the special considerations involved in completing budgets for variable depth layers we consider the 50 m fixed depth layer budget first and then discuss the SML and UOL budgets.

Table 3.3a SML heat storage rate: Time difference vs. spectral approach.

Layer Storage Rate (Wm ⁻²)	W9211A (319.50-335.50)		W9211B (356.68-374.52)		W9211C (394.28-411.24)	
	Time	Spec.	Time	Spec.	Time	Spec.
SML	- 32 [†]	-26 ± 39	- 89 [†]	- 79 ± 22	- 83 [†]	- 82 ± 46

Table 3.3b SML Freshwater storage: Time difference vs. spectral approach (accumulated in cm).

Layer Accum. (cm)	W9211A (319.50-335.50)		W9211B (356.68-374.52)		W9211C (394.28-411.24)	
	Time	Spec.	Time	Spec.	Time	Spec.
SML	8 [†]	7.6 ± 8.4	- 15 [†]	- 12.6 ± 38	- 25 [†]	-33 ± 21

[†]Standard error estimates are not shown for the time difference estimates because they are excessively large due to the very large hour to hour variation and sinusoidal like time dependence of the SML temperature, salinity, and layer depth.

3.5.1 W9211A heat and salt budgets: 14 to 30 Nov, 1992

A couple of weeks prior to the W9211A survey cruise, the fifth Typhoon of the season to hit the region, Typhoon Elsie, and strong westerly winds, the so-called October wind burst period (Cronin et al., 1996), were observed in the survey region. During W9211A, mostly weak winds, relatively clear skies, and low precipitation were observed (Table 3.2, Fig. 3.2) and the average upper ocean temperature increased while the average salinity decreased in each of the three layers.

3.5.1.1 50 m layer

The upper 50 m warmed at an average rate of $\sim 49 \text{ Wm}^{-2}$ estimated from hourly CTD data from the Moana Wave (Table 3.4) and a similar result of $42 \pm 6 \text{ Wm}^{-2}$ was obtained from the R/V Wecoma averaged sections (chapter 2). The estimated net flux of 53 Wm^{-2} agreed well with the storage rate and the surface heat flux (69 Wm^{-2}) dominated the budget. The correlation coefficient of the 1-dimensional (1-D) budget residual (low-passed) and the advection time series is not significantly different from zero but the low frequency response of the residual roughly agrees with the advection time series (Fig. 3.6). We expect that there could be some phase differences between the 1-D residual and horizontal advection given the ~ 32 hr repeat sampling time of the butterfly pattern by Wecoma (chapter 2). The time integrated series (Fig 3.6, panel 5) shows that while the agreement between the residual and advective time series was poor, the integrated net flux reproduces the trend of the storage rate very well.

The upper 50 m salt content at Moana Wave decreased by ~ 0.1 psu but the R/V Wecoma sections show an average decrease of only ~ 0.025 psu (Fig. 3.3) which imply a freshwater gain of 16 cm and 4 cm, respectively (Table 3.5). The reason for the discrepancy is due to the propagation of a relatively fresh water mass from the north that nearly intersected the butterfly center (Fig. 3.4). The front ceased its southward migration around 23 Nov and then meandered over a few tenths of a degree of latitude for the remaining period of the cruise. The strong heterogeneity of the salinity field suggests that point observations near the butterfly center may be biased by the location of the front. The 1-D residual and advection time series vary with comparable magnitudes but are out of phase with the residual time series (Fig. 3.7). The net freshwater accumulation from fluxes amount to -2.1 cm which is in very poor agreement with the storage rate from Moana Wave but is in fair agreement with the result of 4 cm obtained from Wecoma data. The net estimated freshwater advection for the center point was small, ~ 0.5 cm, but advection clearly had a large impact on storage just to the north of the center point. When we consider the variable depth layer budgets we must take this lateral heterogeneity into account, ie. the rate of storage from the Moana Wave data may not be representative. To do this, we consider the simple ratio of the 50 m freshwater content estimated with Wecoma data to that estimated by Moana Wave data, $r = 4/16 \sim 0.25$, and apply it to the Moana Wave SML and UOL storage rate.

3.5.1.2 Surface mixed layer (SML)

The surface mixed layer temperature and depth had strong diurnal variability (Fig. 3.2) prior to two moderately strong wind events that

Layer	Surface (Avg)	Turb.	Pen. Rad.	Ver. Adv.	Hor. Adv.	Summed Fluxes (Sum1)	Heat Storage: Time (Spectral)	Residual =Storage-Sum1	Summed fluxes not including vert. adv. (Sum2)	Est. Vertical Entrain.= Storage-Sum2
W9211A SML	69 ± 7	-9 ± 4	-65 ± 10	~0	14 ± 6	9 ± 14	-32 (-26 ± 39)	-41 ± 14		
W9211A 50m	69 ± 7	-1 ± 1	-9 ± 2	-12 ± 6	6 ± 16	53 ± 19	49	-4 ± 19		
W9211A UOL	69 ± 7	-1 ± 1	-4 ± 1	-23 ± 15	9 ± 29	50 ± 33	80	30 ± 33	73 ± 30	7 ± 30
W9211B SML	-18 ± 8	-13 ± 7	-32 ± 10	~0	-17 ± 6	-80 ± 16	-89 (-79 ± 22)	-9 ± 16		
W9211B 50 m	-18 ± 8	-6 ± 3	-10 ± 2	28 ± 4	-50 ± 13	-56 ± 16	-96	-40 ± 16		
W9211B UOL	-18 ± 8	-21 ± 11	-2 ± 1	109 ± 40	-81 ± 27	-13 ± 50	-150	-137 ± 50	-122 ± 30	-28 ± 30
W9211C SML	-10 ± 6	N/D	-58 ± 10	~0	-5 ± 3	-73 ± 12	-83 (-82 ± 46)	-10 ± 12 (turb?)		
W9211C 50 m	-10 ± 6	N/D	-7 ± 1	1 ± 1	-11 ± 6	-27 ± 9	31	58 ± 9		
W9211C UOL	-10 ± 6	N/D	-2 ± 1	44 ± 20	-23 ± 18	9 ± 28	180	171 ± 28	-35 ± 19	215 ± 19
SMLAverage‡	14 ± 12	-11 ± 8	-52 ± 17	0	-3 ± 9	-52 ± 24	-68 (-62 ± 64)	-16 ± 24		
50 mAverage‡	14 ± 12	-4 ± 3	-9 ± 3	5 ± 7	-18 ± 21	-12 ± 26	-5	7 ± 26		
UOLAverage‡	14 ± 12	-11 ± 11	-3 ± 2	43 ± 47	-32 ± 44	11 ± 66	37	26 ± 66	-32 ± 47	69 ± 47

‡ Turbulence values are estimated for W9211C by simply using the average value from W9211A and W9211B.

Table 3.4 Heat budget results (Wm⁻²): W9211A (319.5-335.5), W9211B (356.68-374.52), W9211C (394.28-411.24).

Table 3.5 Freshwater budget results (cm): W9211A (319.5-335.5), W9211B (356.68-374.52), W9211C (394.28-.24).

Layer	Surface (Avg.)	Turbulent	Ver. Adv.	Hor. Adv.	Summed Fluxes (Sum1)	FW Storage Time (Spectral)	Residual = Storage-Sum1	Summed fluxes not including vert. adv. (Sum2)	Estimated Vertical Entrain = Storage-Sum2
W9211A SML	0.4±2.3	-1±0.5	~0	1.9±3	1.3±3.8	8 (7.6±8.4)	6.7±3.8		
W9211A 50m	0.4±2.3	-1±0.5	-1±1	-0.5±8	-2.1±8.4	16	18.1±8.4		
W9211A UOL	0.4±2.3	-0.4±0.2	-6±4	-2.7±12	-8.7±12.9	19	27.7±12.9	-2.7±12.2	21.7±12.2
W9211B SML	22.4±10.8	-16.1±8	0±1	-20.4±4	-14.1±14	-15 (-12.6±38)	-0.9±14		
W9211B 50 m	22.4±10.8	-12.6±6.3	11.7±3	-40.4±8	-18.9±15.1	-13	5.9±15.1		
W9211B UOL	22.4±10.8	-3.2±1.6	64±14	-57.8±15	25.4±23.2	-14	-39.4±23.2	-38.6±18.6	-24.6±18.6
W9211C SML	5.4±6.4	ND	~0	-6±2	-0.6±6.7	-25 (-33.0±21)	-24.4±6.7		
W9211C 50 m	5.4±6.4	ND	0±1	-11±4	-5.6±7.6	15	20.6±7.6		
W9211C UOL	5.4±6.4	ND	13±4	-15±7	3.4±10.3	64	61.6±10.3	-9.6±9.5	73.6±9.5
SML Cumul. †	28.2±12.8	-25±9	0	-18.5±5.4	-15.3±16.4	-32 (-38±44)	-16.7±16.4		
50 m Cumul. †	28.2±12.8	-20.4±7	10.7±3	-51.9±12	-33.4±19.1	18	51.4±19.1		
UOL Cumul. †	28.2±12.8	-5.4±1.8	71±15	-75.5±20.4	18.3±28.4	69	50.7±28.4	-55.3±24.2	124±24.2

† Cumulative turbulent flux contributions are estimated by simply using the average of the W9211A and W9211B to estimate the turbulent contribution for W9211C.

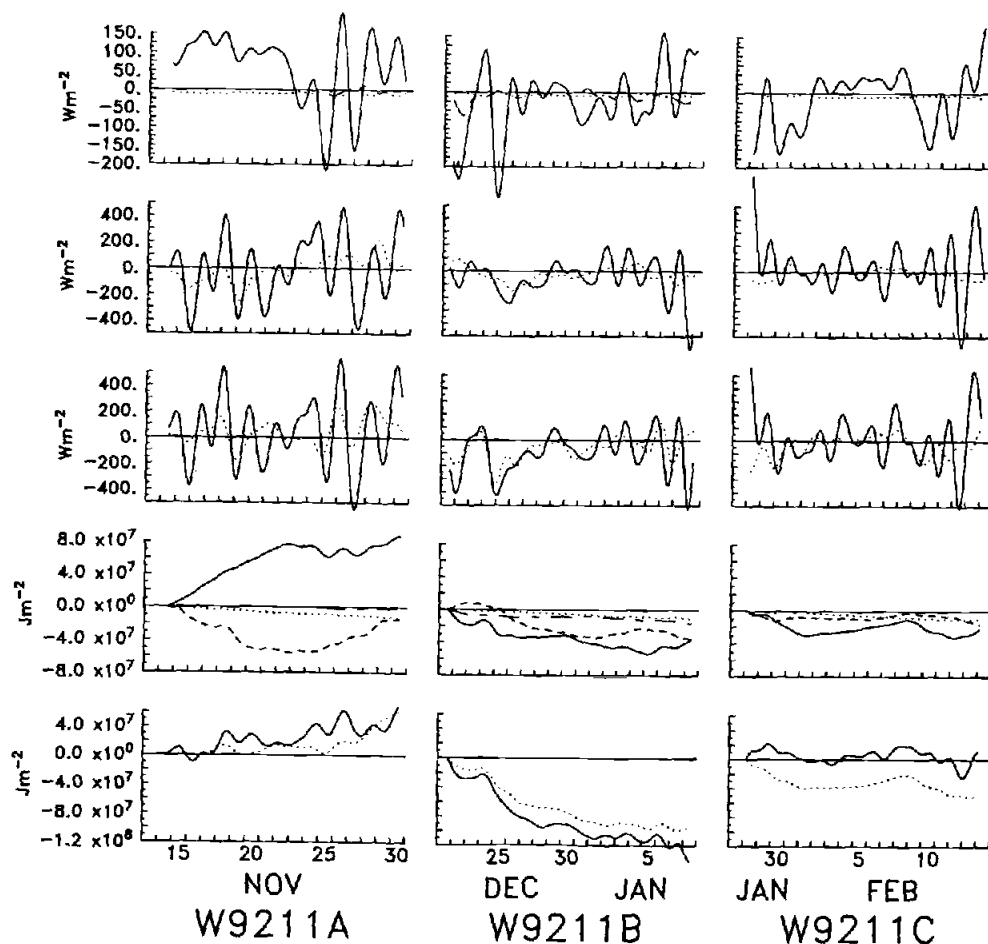


Figure 3.6 The 50 m layer heat budget: Upper panels: Net surface flux (solid black), penetrative radiant flux (small dash), and turbulent flux (wide dash). Panel 2: One-dimensional budget residual (solid) and advection flux (small dash). Panel 3: Rate of change in heat storage (solid) and sum of all fluxes including advection (small dash). Note that all terms in the upper three panels, except advection, have been low-passed at 32 hours. Panel 4: Time integrated surface flux (solid), turbulent flux (wide-narrow dash), penetrative flux (small dash), and advection (med. dash). Panel 5: Time integrated storage rate (solid) and summed fluxes (dash).

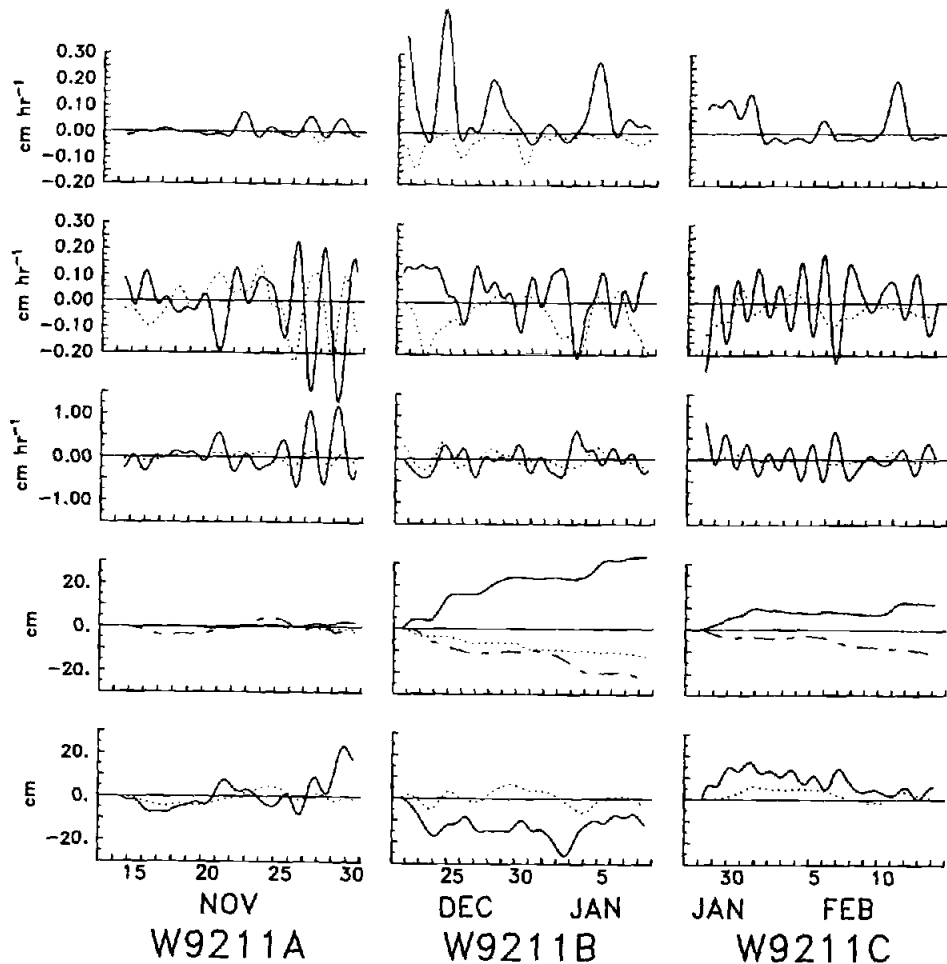


Figure 3.7 The 50 m layer salt budget in terms of equivalent freshwater fluxes: Upper panels: Net surface flux (solid black) and turbulent flux (dash). Panel 2: One-dimensional budget residual (solid) and advection flux (small dash). Panel 3: Rate of change in salt storage (solid) and sum of all fluxes including advection (small dash). Note that all terms in the upper three panels, except advection, have been low-passed at 32 hours. Panel 4: Time integrated surface flux (solid), turbulent flux (wide-narrow dash), and advection (small dash). Panel 5: Time integrated storage rate (solid) and summed fluxes (dash).

Table 3.6. Layer averages: depth, salinity and temperature.

	W9211A (319.50-335.50)	W9211B (356.68-374.52)	W9211C (394.28-411.24)	3 Cruise Average
SML depth (m)	18.5	29	34	27.2
SML salinity (psu)	34.24	34.13	34.18	34.18
SML temp. (°C)	29.33	28.93	29.21	29.16
UOL depth (m)	78	75	76.5	76.5
UOL salinity (psu)	34.56	34.53	34.54	34.54
UOL temp. (°C)	28.14	28.09	28.10	28.11

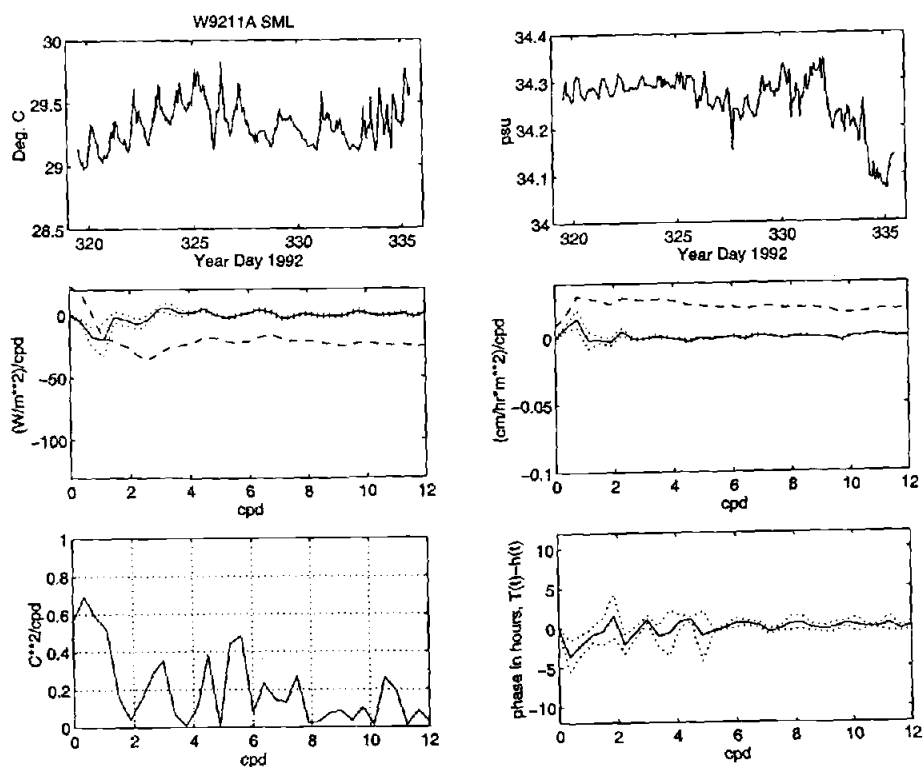


Figure 3.8 Frequency dependence of heat and salt storage for the SML during W9211A. Upper panels show hourly layer average temperature (T_a) and salinity (S_a). Center panels: The left hand panel shows heat storage rate as function of frequency (solid) in cycles per day (cpd) along with 95% confidence limits (fine dash), and the spectrally integrated or summed heat storage which is in units of Wm^{-2} (wide dash). The right hand panel is the same but for freshwater and the integrated freshwater storage has units of $cm\ hr^{-1}\ m^{-2}$. The lower left-hand panel shows the coherence-squared between T_a and h_{sml} . The solid line in the lower right hand panel is a plot of the phase lag (in hours at each frequency) between $h(t)$ and $T_a(t)$. The dotted lines represent the ± 1 standard error. Note that a negative lag here means that h leads T .

occurred on 23-25 Nov. The wind event deepened the surface mixed layer and excited moderately strong currents that oscillated with ~ 2 day period (chapter 2). Following the wind events, the SML temperature had a strong response at a higher frequency than the diurnal cycle while the layer depth range was small, perhaps due to rainfall. The result is that the temperature and h_{sml} have three distinct frequency regimes and thus the temperature time series is neither smooth or stationary. Over the budget period 14 to 30 Nov, the surface mixed layer temperature increased by $\sim 0.5^\circ\text{C}$ (Fig. 3.2) and the depth at the end of the budget period was 3 m deeper than at the beginning but the layer actually lost heat (Table 3.3a). This is a somewhat surprising result given the overall increase in the SML temperature but Fig. 3.8 reveals that while the rate of storage had a low-frequency (DC) warming trend there was a strong cooling peak at the diurnal frequency. As the temperature increases in response to daily heating the layer depth decreases and conversely when the temperature cools at night the layer depth increases, ie. $\partial T / \partial t$ and h are \sim anti-correlated at the diurnal frequency (Appendix C).

The average rate of change in heat storage estimated from differencing in time (-32 Wm^{-2}) and that estimated spectrally ($-26 \pm 39 \text{ Wm}^{-2}$) do not differ significantly. The temperature data are neither smooth nor stationary so that neither the hourly time differencing or the spectral approach are strictly valid. Filtering the data prior to differencing in time gives $\sim -3 \text{ Wm}^{-2}$ for boxcar-filtering of the data at 6 hours (Wijesekera and Gregg, 1996) and -7 Wm^{-2} for fourier filtering with a 24 hour-cutoff. The results are sensitive to the filter and method to $\sim \pm 15 \text{ Wm}^{-2}$. Taking the spectral estimate of -26 Wm^{-2} and the net flux of 3 Wm^{-2} the budget mis-closes by 29 Wm^{-2} . In other words, an additional cooling of -29 Wm^{-2} is needed to close the budget exactly. The budget mis-closure is likely due to

uncertainty in the storage term and underestimates in the penetrative loss term. The underestimate of the penetration term is because the transmission profile is based on the spectral range 340 to 683 nm and so it is not well characterized above 10 m where longer wavelength radiation may penetrate below the SML base (Siegel et al., 1995, Ohlmann et al., 1997). As noted in Sec 3.2e, this effect may be on the order of 10 to 20 Wm^{-2} (C. Ohlmann, pers. comm). The budget misclosure notwithstanding we see that the surface flux of 69 Wm^{-2} was largely offset by the loss -65 Wm^{-2} due to penetrative radiation (Table 3.4). Advection warmed the layer at an average rate of $14 \pm 6 \text{ Wm}^{-2}$ and turbulence cooled the layer at an average rate of $-9 \pm 5 \text{ Wm}^{-2}$.

The SML freshwater budget residual was $6.7 \pm 3.8 \text{ cm}$ (Table 3.5) with the turbulent and horizontal advection fluxes contributing ~ -1 and 1.9 cm each (Table 3.5). The heterogeneity of the salinity field does not affect the SML budget as strongly as the 50 m budget because the storage rate is directly proportional to depth and the SML was relatively shallow (18.5 m, Table 3.6). When we adjust the Moana Wave storage term by applying the ratio $r = 0.25$ to the storage accumulation, to account for the lateral heterogeneity, we get an estimated 2 cm storage change which gives closure to within 1 cm.

3.5.1.3 Upper ocean layer (UOL)

For the UOL heat balance the residual was $30 \pm 33 \text{ Wm}^{-2}$ with the storage rate averaging 80 Wm^{-2} and the summed fluxes averaged $50 \pm 33 \text{ Wm}^{-2}$ (Table 3.5). Vertical advection estimated as a residual was $7 \pm 30 \text{ Wm}^{-2}$ which compares somewhat well with the explicitly calculated value

of $-23 \pm 15 \text{ Wm}^{-2}$. As noted in Appendix D, the uncertainty associated with ignoring layer depth advection could be $O(50 \text{ Wm}^{-2})$ given that $T_a - T_h \sim 1^\circ\text{C}$, $u = 0.1 \text{ m s}^{-1}$, and $\partial h / \partial x = 5 \text{ m} / 100 \text{ km}$ which implies a 5 m increase in depth in 10 days. In fact, we see that the UOL deepening beginning around 17 Nov does not appear to be associated with windstress (Fig. 3.2) and is only partially represented in estimates of vertical velocity (chapter 2) and thus may be associated with horizontal advection of the layer depth itself. The freshwater budget provides some additional insight.

For the UOL freshwater budget we get a residual of $\sim 28 \pm 12.9 \text{ cm}$ (Table 3.5) which reduces to $\sim 13.5 \pm 12.9 \text{ cm}$ using the factor $r=0.25$ to account for the lateral heterogeneity in the sampling domain. Again, as in the heat storage case, we find a large discrepancy in the freshwater storage term as compared to the summed fluxes. There is more freshwater than what can be accounted for in the budget. If the layer deepened because of advection of the layer depth itself we would expect an error in the budgets such that the storage of heat and freshwater would be larger than the estimated fluxes. The estimated vertical velocity accounts for a significant fraction of the change in h_{uol} (chapter 2) but some increases in depth may be associated with horizontal advection of the layer depth since turbulent mixing was weak (Table 3.4). Estimating the vertical advection as a budget residual we get 21.7 cm which reduces to $7.5 \pm 12.2 \text{ cm}$ when the storage term is adjusted for the lateral heterogeneity. The explicitly calculated vertical advection was $-6 \pm 4 \text{ cm}$ and so, as in the heat budget, the residual estimate implies more deepening of the layer than what is accounted for by the direct estimate. So the two budgets are consistent and lateral advection of the layer depth itself is proposed as the missing element from the direct flux estimates.

3.5.2 W9211B heat and salt budgets: 21 Dec, 1992 to 8 Jan, 1993

From 21 Dec to 3 Jan enhanced convective conditions with strong westerly winds (Fig. 3.2) and heavy rainfall were observed (Fig. 3.5). A calm, rainy, and convectively suppressed period began on 3 Jan and lasted past 8 Jan. The upper ocean cooled largely in response to surface and horizontal advective fluxes (Table 3.4) and the upper ocean became saltier despite the heavy rainfall (Table 3.5).

3.5.2.1 50 m layer

The 50 m layer heat budget residual was significantly different than zero, $-40 \pm 16 \text{ Wm}^{-2}$ (Table 3.4), but the sum of the fluxes was correlated with the rate of change in storage and the lower frequency advection response is relatively well correlated with the large advective features, specifically on 25 Dec (Fig. 3.6). Surface and turbulent fluxes cooled the layer at an average rate of $-18 \pm 8 \text{ Wm}^{-2}$ and $-6 \pm 3 \text{ Wm}^{-2}$, respectively. Penetrative radiation accounted for a loss of 10 Wm^{-2} of radiant heat through the layer base. Advection cooled the layer at an average rate of -22 Wm^{-2} making it the dominant heat flux during this period. The relatively large residual is largely due to a discrepancy between the advective terms, primarily the vertical component, and the one-dimensional budget residual near the end of the time series. In other words, if we had closed the budget over a period just 12 or more hours sooner the budget would have closed to $\sim 15 \text{ Wm}^{-2}$.

The 50 m freshwater budget residual is not different from zero, $5.9 \pm 15.1 \text{ cm}$ (Table 3.5). The advective and turbulent fluxes were comparable to

each other and together accounted for an equivalent loss of 41.3 ± 10.6 cm which more than offset the addition of freshwater of 22.4 ± 10.8 cm by the surface flux (Table 3.5). As in the case of the heat budget, one-dimensional processes, i.e. surface forcing and turbulent mixing, were grossly insufficient to balance the budget. The horizontal and vertical advective contributions are critical to achieving budget closure during this period. One caveat, however, is that the 1-D residual time series does not agree strongly with the advection time series. The storage rate of change does, however, agree fairly well with the summed fluxes (Fig. 3.7) and the budget closes within $\sim 25\%$ of the measured precipitation. Could we have gotten the correct answer for the wrong reason. Salinity features can be seen in the time-latitude and time-longitude plots of the Wecoma average 50 m layer salinity (Fig. 3.4b) but the change in freshwater from the 50 m layer estimated from the Wecoma averaged sections was ~ -15 cm which compared well to the -13 cm from Moana Wave. Perhaps because of patchiness in the rain field (Short et al., 1997) we should not expect to obtain good correspondence between the 1-D residual and advection (Feng et al., 1998).

3.5.2.2 Surface mixed layer (SML)

During the peak phases of the wind burst strong mixing drove the SML base within a few meters of the UOL base (Fig. 3.2) and latent heat loss was more than -200 Wm^{-2} (Fig. 3.5). By the third phase of the wind burst the sensible heat flux was positive indicating that the surface ocean temperature was less than the overlying atmosphere. Good closure of the heat budget was achieved with surface, penetrative, and horizontal

advective fluxes contributing about equally and with the turbulent flux being the smallest term at -13 Wm^{-2} (Table 3.4). A key finding from this study is that horizontal advection was as important to the budget as the surface term. Given the strength of the wind forcing it is surprising that the turbulent term was the smallest. One reason suggested Smyth et al. (1996b) is that the turbulent flux at the base of the SML gave positive heat fluxes almost as often as negative fluxes due to rain induced temperature inversions.

The SML freshwater budget closed to within a centimeter (Table 3.5). In the case of the SML, horizontal advective processes are important along with the surface and turbulent flux terms to close the budget. The successful closure of these budgets, despite the relatively large error bars (Table 3.5), point to the fundamental importance of understanding the advective response for successful simulations of the air/sea interaction in this region.

3.5.2.3 Upper Ocean Layer (UOL)

The UOL loss heat at an average rate of -150 Wm^{-2} but the estimated fluxes account for only $-13 \pm 50 \text{ Wm}^{-2}$. The value of vertical entrainment estimated as a residual was $-28 \pm 30 \text{ Wm}^{-2}$ which compares very poorly with the directly estimated vertical advection value of $109 \pm 40 \text{ Wm}^{-2}$. One implication is that the vertical advection estimate is grossly wrong but a review of the temperature and vertical velocity profiles (chapter 2) suggests otherwise. Strong downwelling occurred during this period but strong gradients in density were observed along the North to South transect which, as they propagated northward, may have acted to shoal the UOL.

which in turn was being deepened by the convergent flow. The implication is that this shoaling would tend to act as a cooling flux of -137 Wm^{-2} while the downwelling provided warming at a rate of 109 Wm^{-2} . This argument seems plausible but another possibility is that the storage term is unreliable and thus the residual estimate is unreliable. Horizontal and vertical heat advection dominates the UOL balance (Table 3.4) and the sense of the advection fluxes is consistent with equatorial downwelling in response to the westerly wind stress (chapter 2). It is interesting to note that the largest turbulent heat flux for this layer occurred after the subsidence of the winds and appears to be a result of the strongest observed sub-surface shear (Fig. 3.10; Smyth et al., 1996b). Meridional-depth distributions of gradient Richardson number (Fig. 3.10), temperature (Fig. 3.11a), and salinity (Fig. 3.11b) calculated from Wecoma Seasoar CTD and ADCP data suggest that the local observation of turbulence by Moana Wave at $\sim 1.75^\circ\text{S}$ may not represent the strongest mixing in the Wecoma butterfly domain. As implied by low Ri number, the strongest mixing appears to be occurring just south of the Moana Wave location at $\sim 2^\circ\text{S}$, the edge of the near-equatorial zone as defined by the equatorial deformation radius of $\sim 250 \text{ km}$ (Philander, 1990). The gradient Richardson number falls below 0.25 on 2 Jan in at least four locations along the meridional section (Fig. 3.10) and by 3 Jan the Richardson number profile and temperature profile have evolved substantially with cooler water apparently mixing upward at $\sim 2^\circ\text{S}$ (Fig. 3.11a). The signal is less apparent in salinity (Fig. 3.11b) but there is still a suggestion of rising isohalines in the south. The R/V Noroit Seasoar temperature sections from 5°S to 5°N show similar features further south as well (Inall et al., 1997). A simple

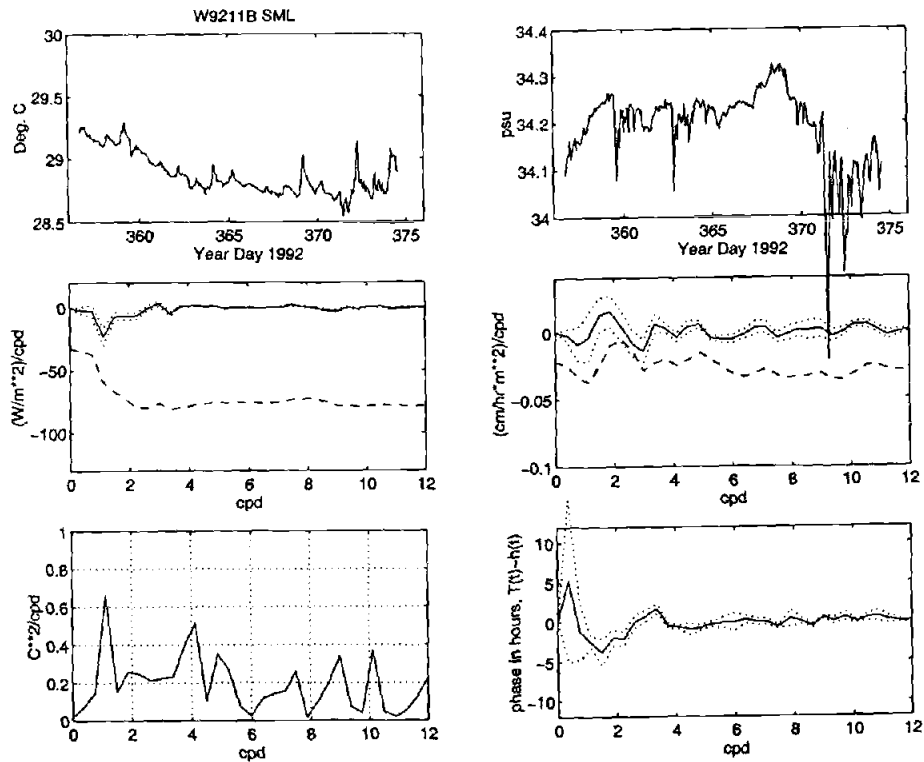


Figure 3.9 Frequency dependence of heat and salt storage for the SML during W9211B. Upper panels show hourly layer average temperature (T_a) and salinity (S_a). Center panels: The left hand panel shows heat storage rate as function of frequency (solid) in cycles per day (cpd) along with 95% confidence limits (fine dash), and the spectrally integrated or summed heat storage which is in units of Wm^{-2} (wide dash). The right hand panel is the same but for freshwater and the integrated freshwater storage has units of $cm\ hr^{-1}\ m^{-2}$. The lower left-hand panel shows the coherence-squared between T_a and h_{sml} . The solid line in the lower right hand panel is a plot of the phase lag (in hours at each frequency) between $h(t)$ and $T_a(t)$. The dotted lines represent the ± 1 standard error. Note that a negative lag here means that h leads T .

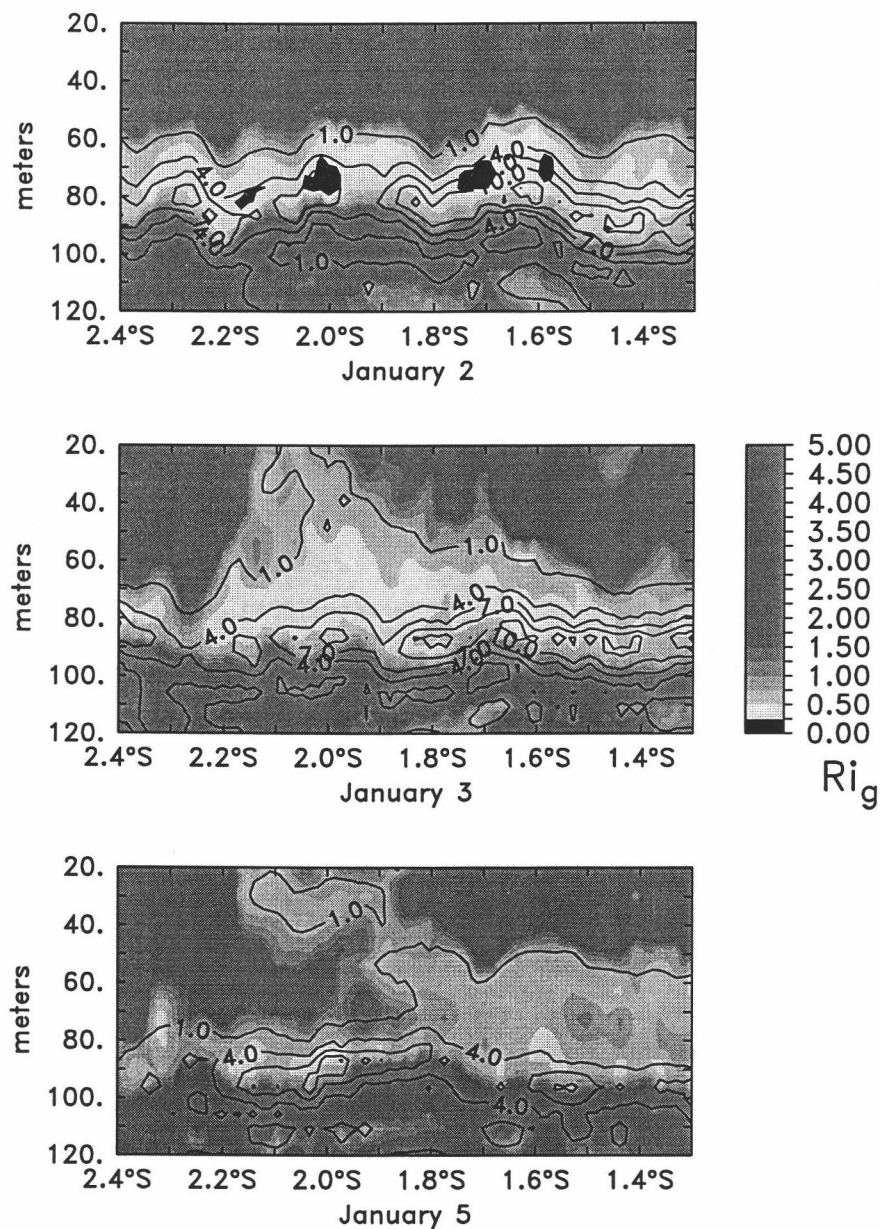


Figure 3.10 Meridional section distributions of gradient Richardson number and shear-squared (contours in units of 10^{-4} s^{-2}) from Wecoma Seasoar density and ADCP data.

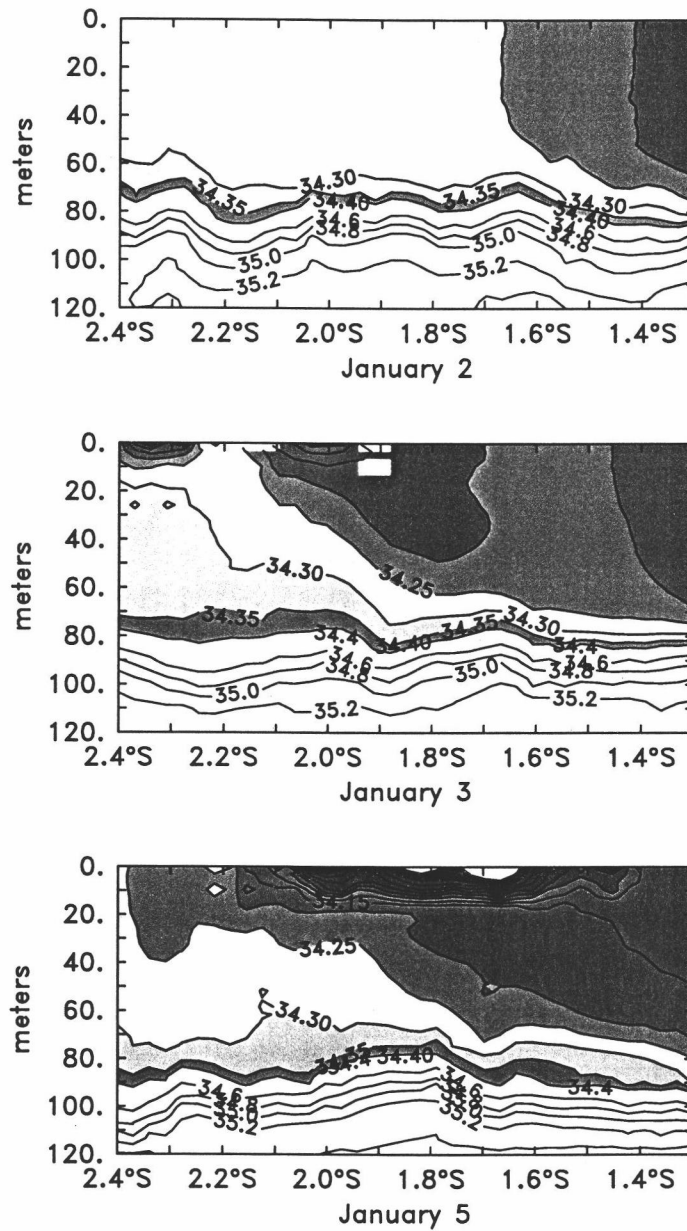


Figure 3.11b Meridional section distributions of salinity from Wecoma Seasoar data.

model of the equatorial ocean response to uniform westerlies shows that coincident with the zonal Yoshida Jet and equatorward flow, the thermocline is displaced downward within the equatorial zone and upward just outside the zone (Philander, 1990; his Fig. 3.4). We hypothesize that this mixing near the southern half of the butterfly pattern may be partly responsible for the genesis of cool/salty fronts (Fig 3.11a,b) that propagated northward (chapter 2).

We achieved relatively poor closure of the UOL freshwater balance. As in the heat budget case, advection of the layer depth that acted to shoal the layer may account for some of the missing cooling and freshening. We note here that for the period Dec 20 to Jan 8 Feng et al. (1998) report good closure of the 50 m and UOL heat and salt budgets, to within 10 Wm^{-2} and 20% of rainfall, respectively. We postulate, however, that the poor agreement between the results reported here and Feng et al., (1998) indicate that the budget closure is very sensitive to the budget period and method of calculating the storage terms. For example, if we had closed our 50 m budget over year day 356.7 (Dec 21) to 374.0 (8 Jan) instead of 374.5 the budget would have closed to within 10 Wm^{-2} (Fig. 3.6) instead of $-40 \pm 16 \text{ Wm}^{-2}$ (Table 3.4). Also, it is important to note that Feng et al. (1998) calculated the vertical velocity by weighting the horizontal divergence and isopycnal displacements to minimize the budget. This approach may achieve good budget closures but it may also obscure unresolved processes (e.g. advection of layer depth).

3.5.3 W9211C heat and salt budgets: 28 Jan, 1992 to 15 Feb, 1993

Prior to the commencement of this cruise the ocean was in a nominally upwelling regime with easterlies driving a surface westward flow and the top of the thermocline was at ~ 50 m from 27-29 Jan (chapter 2). The easterlies gave way to moderately strong north-westerlies with occasional intense squall events and the thermocline deepened sharply around 30 Jan. The latent heat loss was comparable to the westerly wind burst period of W9211B (Table 3.1) as noted by Weller and Anderson (1996) but with clearer skies that gave 20 to 25 Wm^{-2} more shortwave radiation than during W9211B (Table 3.1). During W9211B there was intense, relatively persistent and organized wind forcing that coupled strongly to the ocean and generated a relatively well organized ocean response, i.e. a Yoshida Jet (Smyth et al., 1996a) and near-equatorial downwelling (chapter 2). During W9211C the wind forcing was much more disorganized and intermittent but occasionally very intense. The result was that the upper ocean was relatively well mixed as if by an "egg beater" but without the development of any strong lateral thermohaline gradients. These weak gradients coupled with only relatively weak currents resulted in modest horizontal advective fluxes compared to W9211B (Tables 3.4, 3.5) except for the period when the thermocline was shallow from 27-29 Jan (chapter 2).

3.5.3.1 50 m layer

The shallow thermocline and the internal tide present some difficulty for closing the 50 m budget because the estimated vertical

advective heat flux estimate failed to capture the large vertical response early in the cruise as discussed in chapter 2 and shown in Fig. 3.6. The 50 m layer budget misclosure is very large at 58 Wm^{-2} . The residual of the heat budget should be equal to the turbulent flux but it is unreasonable to attribute $+58 \text{ Wm}^{-2}$ to turbulence and instead we consider some sources of error. The 1-D residual had considerable variability before 30 Jan and after 10 Feb that is not reproduced by the advection time series (Fig. 3.6). If the period before 30 Jan is omitted the budget would close within $\sim 15 \text{ Wm}^{-2}$. There is also a difference of 12 Wm^{-2} between the UOP mooring and the Wecoma net surface flux but it is in the “wrong” sense, i.e. using the Wecoma data would worsen the mis-closure.

The freshwater budget provides some additional insight. The 50 m salinity field (Fig 3.4c) was fairly laterally homogenous over the butterfly after 30 Jan. The trend of the 1-D residual roughly follows the trend of the advection time series after 30 Jan (Fig. 3.7) just like the heat budget. This result also suggests that the vertical velocity is relatively poorly estimated in the early period. Specifically, since the thermocline was shallow at the beginning of the time series and comparisons between the depth of the UOL base and vertical velocity at that depth do not correspond very well prior to 30 Jan (chapter 2) it is probable that much of the misclosure is attributable to error in the vertical velocity estimate.

3.5.3.2 Surface mixed layer (SML)

The SML had a strong and deep diurnal cycle throughout most of the period following the deepening of the thermocline after 30 Jan. The heat budget closed to $-10 \pm 12 \text{ Wm}^{-2}$ with the layer losing heat at an

average rate of -83 Wm^{-2} and the largest contributor to the budget was the penetrative flux at -58 Wm^{-2} . Given that turbulent fluxes were not included in the budget it seems reasonable that the residual is easily attributable to turbulent diffusion especially since it is about the same as the turbulent flux estimates estimated for both W9211A and W9211B. There was a strong cooling peak at the diurnal and semi-diurnal frequencies (Fig. 3.12). The semi-diurnal contribution was not present during W9211A (Fig. 3.8) or W9211B (Fig. 3.9). Also, during this cruise soliton type structures in the thermocline were observed that occurred with the semi-diurnal tide. Given that the SML base was near the top of highly stratified regions on 27-31 Jan and 9-12 Feb mixing at the base of the SML may have been strongly influenced by the semi-diurnal internal tide and, in particular, the soliton structures. It is possible, however, that some contribution to the semi-diurnal peak may be partly due to the second harmonic of the Fourier representation of the non-sinusoidal diurnal cycle. The variation in depth and temperature at the semi-diurnal frequency resulted in a net cooling which may be explained by both mechanisms.

The freshwater budget has a large residual of $\sim -24.4 \pm 6.7 \text{ cm}$ and we speculate that a considerable fraction of it is due to turbulent diffusion. The net surface forcing and horizontal advection were fairly small during this period and tended to offset each other. The storage rate of freshwater (Fig 3.12) shows a strong response at the diurnal frequency but there is no significant peak at the semi-diurnal frequency. If the semi-diurnal tide was important to the heat budget it does not appear to be so for the freshwater budget. This latter consideration suggests that the semi-diurnal response in the heat storage rate is probably not due to enhancement of turbulent mixing at the internal tidal frequency.

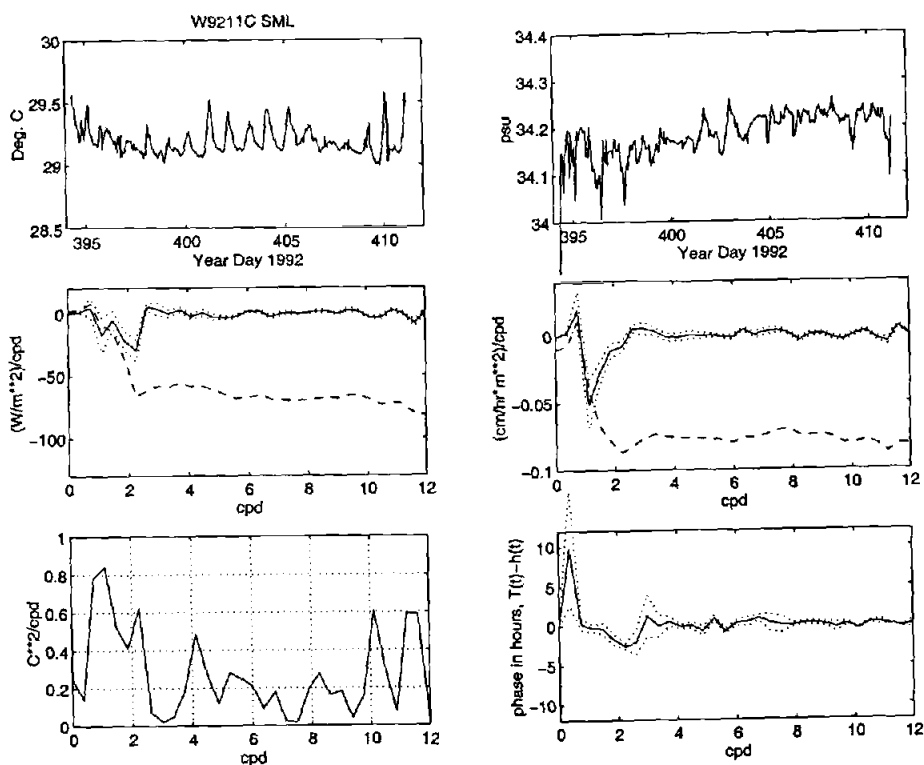


Figure 3.12 Frequency dependence of heat and salt storage for the SML during W9211C. Upper panels show hourly layer average temperature (T_a) and salinity (S_a). Center panels: The left hand panel shows heat storage rate as function of frequency (solid) in cycles per day (cpd) along with 95% confidence limits (fine dash), and the spectrally integrated or summed heat storage which is in units of Wm^{-2} (wide dash). The right hand panel is the same but for freshwater and the integrated freshwater storage has units of $cm\ hr^{-1}\ m^{-2}$. The lower left hand panel shows the coherence-squared between T_a and h_{sml} . The solid line in the lower right hand panel is a plot of the phase lag (in hours at each frequency) between $h(t)$ and $T_a(t)$. Note that a negative lag means that h leads T . The dotted lines represent ± 1 standard error.

Upper ocean layer (UOL)

The UOL heat balance miscloses by 180 Wm^{-2} using the directly estimated vertical advection result (Table 3.4) which is suspect as discussed earlier for the 50 m layer case. Given the large increase in the thermocline depth that was not captured by the vertical velocity estimates (chapter 2) a better estimate of vertical advection of heat and freshwater are likely obtained from the budget residuals in this case. The positive sense of both heat and freshwater residuals suggests that the vertical velocity may be under estimated and/or advection of the layer depth contributed to net heating and freshening. From the residuals then, we estimate that downwelling advected heat at an average rate of 215 Wm^{-2} and amounted to an equivalent increase in freshwater content of 73.6 cm, not including the influence of turbulence in both cases. If these estimates are accurate, downwelling dominated the budget and horizontal advection and the net surface flux were nearly an order of magnitude weaker (Table 3.4, 3.5).

3.5.4 Overall heat and salt budgets for the IOP surveys

The three cruise average surface flux was 14 Wm^{-2} and the SML lost heat at an average rate of 68 Wm^{-2} . Most of the balance is accounted for by penetrative radiation (-52 Wm^{-2}) and turbulent mixing which accounted for -11 Wm^{-2} . Horizontal and vertical advection were negligible and the three cruise residual was only $-16 \pm 24 \text{ Wm}^{-2}$. For the 50 m layer, the dominant term was horizontal advection which cooled the layer at an average of -18 Wm^{-2} and the budget closed to $7 \pm 26 \text{ Wm}^{-2}$. This last result comes from the fact that the residuals from W9211B and W9211C largely

offset each other. The UOL had a vertical advective heat flux that was 12 Wm^{-2} larger than the lateral cooling and thus advection tended to balance turbulent mixing (-11 Wm^{-2} , estimated from the first two cruises) and the overall budget residual was, $26 \pm 66 \text{ Wm}^{-2}$. Again the residuals from the W9211B and W9211C budgets tended to offset each other so that the three cruise residual appears small. If the budget residuals are used to estimate vertical entrainment, excluding turbulent diffusion, we find that the estimated vertical entrainment is 69 Wm^{-2} which compares reasonably well with the directly estimated vertical advection of 43 Wm^{-2} . The main point here is that vertical advection appears to be the largest flux for the UOL followed by horizontal advection for the three survey periods.

The cumulative SML freshwater budget residual was $-16.7 \pm 16.4 \text{ cm}$, assuming an average of W9211A and W9211B turbulent flux estimates are a valid estimate for W9211C. The surface flux contributed 47 cm (UOP composite, Table 2) and advection removed $24 \pm 6 \text{ cm}$. Note that we could obtain fairly good closure if we assumed that the turbulent flux during W9211C was -24.4 cm , which is the residual estimate for the cruise period, instead of the estimate of $\sim -8.5 \text{ cm}$ obtained from the average of W9211A and W9211B turbulent flux estimates. The upper 50 m became slightly saltier (Fig. 3.2) and the budget residual was $\sim 50 \text{ cm}$, excluding turbulent contributions for W9211C. Horizontal advection (-51.9 cm) more than offset the surface flux of 28.2 cm (Table 3.5). Vertical advection was estimated at $\sim 11 \text{ cm}$ but this result is likely an underestimate and most of the residual is probably due to the vertical advection estimate from W9211C as noted earlier except for about 12 cm that was due to heterogeneity of the salinity field during W9211A that biased storage estimates. For the UOL, the budget residual was about the same as the

50 m layer, ~51 cm. Advection is the dominant process that regulated storage rates in the UOL over the period of the surveys with horizontal and vertical advection tending to decrease and increase freshwater content, respectively.

3.6 Discussion/Conclusions

Our initial goal was to verify the heat and freshwater fluxes by demonstrating closure of the respective budgets and we were able to close some of the budgets satisfactorily (within useful limits of the uncertainty). All of the SML layer heat and freshwater budgets nearly closed within limits of uncertainty and all of the SML heat budgets were closed to within ~20 Wm⁻². The SML freshwater budget was nearly closed for each cruise period with the exception of W9211C principally because there was no turbulence data available. Estimating the turbulent salt flux from the budget residual seems reasonable given the sign and magnitude of the residual in comparison to W9211B leading us to the conclusion that budget closure was essentially achieved. Further, the desired closure of the SML heat budgets to within 10 Wm⁻² for two very dynamic periods, W9211B and W9211C, was achieved and strong statements about the important mechanisms responsible for regulating the SML temperature can be made.

For the 50m and UOL layers, it is possible to achieve good budget closure in almost all cases if we adjust the averaging or budget period given the background geophysical noise. Also, data smoothing approaches may yield a balanced budget but they tend to be subjective and hence prone to bias. We have tried to avoid these temptations and instead have focused on closing budgets over periods for which we have the longest

common time record for all the fluxes. We have also attempted to verify that the estimated flux time series corresponds to the rate of change in storage so that we can make meaningful statements about the heat and moisture exchange processes. For all the layers considered, we have learned that the storage rate must be well estimated, temporally and spatially, and care must be exercised to insure that the storage terms are either well represented or sufficient averaging can be achieved to obtain reliable estimates of mean quantities.

While the net surface flux (14 Wm^{-2}) is an important term to the SML heat budget, the overwhelming importance of the penetrative term to the SML heat budget (Siegel et al., 1995) is confirmed in each of our case studies. In the SML, the turbulent heat flux averaged $\sim -11 \text{ Wm}^{-2}$ (averaged over the first two surveys) and the advection term averaged only -3 Wm^{-2} giving a net oceanic process flux of -14 Wm^{-2} . This result is consistent with earlier studies of the warm pool which suggested that advection in the warm pool was small and that the net surface heat flux was largely balanced by local mixing (Niiler and Stevenson, 1982, Godfrey and Lindstrom, 1989). For the 50 m layer and the UOL, the penetrative term is less important, but not negligible in the 50 m case, and advection tends to balance the net surface heat flux. Oceanic heat advection exported $\sim -13 \text{ Wm}^{-2}$ from the 50 m layer and was about 3 times larger than turbulent heat loss which averaged -4 Wm^{-2} for the first two R/V Moana Wave surveys during the IOP giving a net oceanic processes flux of -17 Wm^{-2} . It is remarkable that this estimate of oceanic processes agrees so well with the SML result, albeit for different reasons. Our results are also consistent with the result of -10 to -20 Wm^{-2} estimated for ocean processes from atmospheric budget studies (Ramanathan et al., 1995).

We estimate that for the 50 m layer and the UOL that the advective component was ~ 3 times larger than the turbulent term. This is a significant finding which challenges conventional views of the warm pool where local turbulence was thought to balance the net surface flux and where advection was thought to be negligible (Niiler and Stevenson, 1982; Godfrey and Lindstrom, 1989). It should be noted that Niiler and Stevenson (1982) directly extrapolated central equatorial Pacific turbulence estimates (-50 to -100 Wm^{-2}) which may be too large for the western equatorial Pacific warm pool which has been estimated between -1 to -20 Wm^{-2} from COARE IOP studies (Wijesekera and Gregg, 1996; Smyth et al., 1996b). A mechanism for weak turbulent heat exchange from the upper ocean in the warm pool was suggested by Lukas and Lindstrom (1991) who observed that net surface freshwater input in this region can form a salinity gradient known as the "barrier layer". A persistent "barrier layer" as defined by Lukas and Lindstrom (1991) was not, however, observed during most of the survey periods but such a mechanism was occasionally important in reducing the exchange of heat during the December wind burst by inverting the thermal gradient in the SML (Smyth et al., 1996b).

If the heat advection and turbulent flux estimates for the 50 m layer and the UOL are representative of the longer term values then advective cooling is 3 to 4 times larger than cooling from local mixing in those layers. If this is true, then advective cooling below the SML would tend to balance the local turbulent heat flux from the SML over the long term. In this way, heat that was mixed down through the base of the SML could be exported away. The importance of advection to the local freshwater budget supports the idea that advection may be important to the long term heat budget because salt acts, in some sense, as a tracer of ocean circulation.

If our estimates are representative of the long term response then the connection of the local SML temperature response may be significantly coupled to the deeper ocean circulation. By extension, subsurface advection may be an important mechanism by which the warm pool SML heat storage and hence SST is modified over long time scales like the ENSO cycle. These comments are purely speculative given the time frame of the present study and are simply intended to foster serious consideration of all of the terms in the heat and salt budgets of the warm pool given the comparable magnitude of the advection term, for example, to the surface term from this study. The relative success of ENSO modeling using the long wave (hence long time scale) approximated equations of motion (Zebiak and Cane, 1987) suggest that the information from this study may only serve to better estimate parameters used to represent sub-grid scale diffusive processes in the ocean. If the diffusive physics for time scales of weeks to months cannot be well parameterized for successful model prediction of important long time scale phenomena (e.g. ENSO) then it may be necessary to directly model the advective processes on time scales of days to months.

The one-dimensional thermal response of the SML of the western Pacific warm pool suggested by other researchers (Godfrey and Lindstrom, 1989; Niiler and Stevenson, 1982; Anderson and Weller, 1996) appears to be correct under some conditions, like those observed during much of W9211A and W9211C, but horizontal advection can occasionally be considerable. The largest term by far in the budget for these conditions is the penetrative term which substantially limits the net deposition of heat into the SML and thus appears as cooling term in the budget. Turbulent mixing essentially balanced the surface flux and horizontal advection was small on average over the three surveys. Horizontal salt advection was the

second largest term in the SML salt budget during a high precipitation period and horizontal salt advection is an important component of the salt budget that acts to maintain the salinity of the warm pool. It appears that horizontal and vertical advection may be important fluxes for redistributing heat and salt in the warm pool SML particularly during westerly wind bursts. Our results suggest that successful modeling of the SML temperature and hence SST response on day to month time scales will require explicit incorporation of advective processes.

We hypothesize that the advection mechanism works as follows during westerly wind bursts. Strong westerly winds set up a Yoshida Jet with downwelling occurring inside the near-equatorial region (within a equatorial Rossby radius $\sim 250\text{km}$) and upwelling outside as depicted by simulation of the equatorial ocean response to westerly wind forcing by Philander (1990). As the thermocline rises in the outside equatorial zone the wind driven shear effectively entrains cold salty water into the SML and the cold salty water converges toward the equator via Ekman convergence. This implies that frontal genesis occurs within the warm pool itself and microstructure observations within the near equatorial zone may not be representative of the greater warm pool. The implication is that ocean processes in the warm pool cause it to cool itself "internally" as turbulent and advective processes work together to distribute the heat within the warm pool itself. This is not suggested as the only advective mechanism because general ocean circulation is also likely important.

Chapter 4

General Conclusions

Waliser (1996) reviewed the relatively short history of our evolving understanding of the warm pool SST regulation and traced the initial hypotheses, which focused largely on the atmosphere: Newell (1979) initially proposed an evaporation limited SST to $\sim 30^{\circ}\text{C}$ which was later modified for increased albedo from deep convective clouds limiting SST to $\sim 28^{\circ}\text{C}$ (Graham and Barnett, 1987); Ramanathan and Collins (1991) hypothesized that the primary limiting mechanism was solar shielding from relatively high altitude cirrus clouds that act as a "thermostat." The "thermostat" hypothesis as proposed introduces a non-local interaction associated with the convergence of moisture laden trade winds over the warmest ocean waters. Coupled ocean-atmosphere models evolved (Cane and Sarachik, 1987) that attempted to feedback the ocean response into the atmosphere and attained some degree of success in predicting the equatorial ocean-atmosphere response but much improvement in predictive skill was needed. Using tropical ocean and atmosphere data from 1970 to 1993, Waliser (1996) found that fairly rapid changes in the upper ocean temperature and sea surface height coincided with the evolving atmosphere but were too large to be accounted for by surface heat fluxes alone. These studies strongly suggest that something other than the local air-sea heat exchange must contribute significantly to the long-term heat balance.

From our work, horizontal and vertical advection appear to be important processes for distributing heat and salt in the warm pool during

or just after strong wind events like westerly wind bursts. It perhaps should not be surprising that vertical advection is important here given the proximity of the survey region to the equator. The equatorial deformation radius is about 250 km assuming a first mode Kelvin wave propagation speed of about 3 ms^{-1} and an upper ocean effective depth of 50 m.

Theoretical and model results suggest that a distinctive equatorial zone is established within two deformation radii by westerly winds after a few days (Philander, 1990). Inside the equatorial zone, surface meridional Ekman convergence drives strong downwelling while upwelling occurs outside the region. It is not clear that these processes are important over the long term, however, unless the IOP average is representative of the long term warm pool conditions.

Compared to the average observed surface flux of 14 Wm^{-2} (Table 3.3) and to the estimated annual surface fluxes that range from 20 to 80 Wm^{-2} (Weare, 1981; Reed, 1982, Esbensen and Kushnir, 1981) the estimated horizontal heat advection of -18 Wm^{-2} in the 50 m layer probably cannot be ignored in the long-term balance. Alternatively, however, one may argue that advection in the SML, which was negligible in the long term mean, need only be considered because it is the layer that is involved with direct heat exchange with the atmosphere. Further, because large advective events in the SML often coincide with large advective events in the deeper layers, the synchronicity of the advective events largely eliminates the need to consider the impact of heat advection in deeper layers on the local air/sea interaction. Is it possible, however, that heat advection in the deeper layers may manifest itself in a time delayed sense on the local air/sea interaction through the modification of heat storage in layers beneath the SML as suggested in chapter 3?

The advective flux depends on layer thickness and the SML is often shallow so that even strong lateral gradients may at times contribute very little to the SML heat balance. But could these lateral gradients contribute substantially to the change in the heat storage below the SML as occurred near the beginning of W9211A and at the end of W9211B (Figs. 2.9, 2.15)? The SML may act as an insulator for the deeper layers keeping them from exchanging heat with the atmosphere. This mechanism is somewhat similar to the barrier layer hypothesis (Lukas and Lindstrom, 1991) but it is not dependent on saline stratification per se and introduces the idea of a delayed response associated with advective loading. When the winds become strong at a later period and deepen the SML, the ocean may exchange heat energy accumulated through advection in the deeper layers with the atmosphere. Local turbulent fluxes do not necessarily need to be exceptionally large to release this stored heat since there is no implication that vertical stratification throughout the upper water column is necessarily enhanced when horizontal advection is large. In fact, shear driven mixing near the top of the thermocline could generate relatively well mixed subsurface regions and there is evidence of such mixing at the top of the thermocline following the weakening of the winds after Jan 3 (Smyth et al., 1996, their Fig. 2a). Following the wind burst high rainfall induced saline stratification (Figure 2.9) reduced the SML depth to less than 10 m (Fig. 2.2) but the upper 10 to 50 m was fairly well mixed. During this period strong lateral temperature gradients (Fig. 2.5) contributed to large horizontal advective fluxes (Fig. 2.15) particularly below the SML and above the thermocline. This mechanism provides a way for the upper ocean below the SML to change its heat storage without strong direct interaction with surface forcing. At a later time, winds of sufficient strength and duration may erode the stratification at the SML base and cause mixing in the less

strongly stratified subsurface region thus releasing the stored heat energy. Such a time-delayed mechanism suggests that the ocean-atmosphere system can appear on short time scales to be a one-dimensional system but over longer time scales, months to years, ocean advection may be important in charging and discharging the warm pool "heat capacitor" (WCRP, 1990) and thus influencing SST.

From a modeling stand point it would be helpful if we could definitively rule out advection as an important component of the heat and salt budgets because modeling of advection is generally difficult without a much better understanding of mixing processes that establish fronts and the response of the flow field that transports them. Our results suggest, however, that we probably cannot ignore ocean transport for the salt budget and perhaps not for the heat budget either. Inverse models or data assimilation techniques may be helpful but in-situ temperature data is generally sparse except for satellite SST data which may not be sufficiently sensitive, $O(0.2\text{ }^{\circ}\text{C}/100\text{km})$, or representative of temperature variations that may be important, i.e. subsurface. The reason that relatively small gradients are important in this region is because the SML is occasionally deep and the upper ocean currents can occasionally be very large.

The larger implication of chapters 2 and 3 is that the response of the local ocean-atmosphere system may depend, at least in part, on non-local processes, specifically heat and salt advection. This latter statement is in conflict with early assertions about the warm pool that suggested a largely local thermodynamic balance between the ocean and atmosphere existed in the warm pool. How can this conflict be reconciled? There is no doubt about the importance of local air-sea processes in warm pool SST regulation but are they sufficient to account for the SST response? The

summarized heat and freshwater budget data from chapter 3 shows that the three layers are dominated by different processes.

For the SML, the heat budget is largely dominated by the penetrative term given that the layer is often shallow and the water clarity is generally very high in the region. The SML freshwater balance results mostly from the competing effects of surface forcing and turbulent entrainment at the layer base. For the 50 m and UOL layers the penetrative term is less important but advection of both heat and salt dominate the response. It is important to note, however, that vertical advection tended to offset the horizontal advective contributions to the deeper layer budgets. The episodic sustained wind events in the region are an important link in predicting the upper ocean heat and freshwater response because they drive the latent heat flux and advective flux by deepening the SML and generating strong currents.

Bibliography

- Anderson, S. P., R. A. Weller, and R. Lukas, 1996: Surface buoyancy forcing and the mixed layer of the western Pacific warm pool: Observations and 1-d model results, *J. Climate*, 9, 3056-3085.
- Antonissen, Huyer and Kosro, 1997a: On the evolution of the western Pacific warm pool during the TOGA COARE IOP: Advection of heat and salt., *to be submitted to J. Geophys. Res.*
- Bjerknes, J., 1966: A Possible Response of the Atmospheric Hadley Circulation to Equatorial Anomalies of Ocean Temperature, *Tellus*, Vol. XVIII, No. 4, 515-524.
- Bjerknes, J., 1969: Atmospheric Teleconnections from the Equatorial Pacific, *Monthly Weather Review*, Vol. 97, No. 3, 525-535.
- Bradley, E. F., J. S. Godfrey, P. A. Coppin, and J. A. Butt, 1993: Observations of net heat flux into the surface mixed layer of the western equatorial Pacific Ocean, *J. Geophys. Res.*, Vol 98, No. C1, 22521-532.
- Bradley, F and R. Weller, 1997: Fourth Workshop of the TOGA COARE Air-Sea Interaction (Flux) Working Group 9-11 October, 1996, Woods Holes, Mass., TOGA COARE International Project Office, UCAR. 49pp
- Brainerd, K. E., and M. C. Gregg, 1995: Surface mixing and mixing layer depths, *Deep Sea Res.*, 42, 9, 1521-43.
- Chen, D., A. J. Busalacchi, and L. M. Rothstein, 1994: The roles of vertical mixing, solar radiation, and wind stress in a model simulation of the sea surface temperature seasonal cycle in the tropical Pacific Ocean, *J. Geophys. Res.*, 99, C10, 20345-359.
- Chereskin, T. K., E. Firing, and J. A. Gast, 1989: Identifying and screening filter skew and noise bias in acoustic Doppler current profiler measurements. *J. Atmos. Oceanic Technol.*, 6, 1040-1054.
- Cronin, M. F., M. J. McPhaden, 1997: The upper ocean heat balance in the western equatorial Pacific warm pool during September-December 1992, *J. Geophys. Res.*, 102, 8533-8553.

- Davis, R., 1976: Predictability of sea surface temperature and sea level pressure anomalies over the north Pacific ocean, *J. Phys. Oceanogr.*, *6*, 249-266.
- De Wet, T., and J. W. J. Van Wyk, 1986: Bootstrap confidence intervals for regression coefficients when the residuals are dependent, *J. Statist. Comput. Simul.*, *23*, 317-327.
- DeSzoeko, R. A., 1980: On the effects of horizontal variability of wind stress on the dynamics of the ocean layer, *J. Phys. Oceanogr.*, *10*, 9, 1439-54.
- Efron, B., and G. Gong, 1983: A leisurely look at the Bootstrap, the Jackknife, and Cross-Validation, *The American Statistician*, *37*, 36-48.
- Efron, B. and R. J. Tibishirani, 1993: "An Introduction to the Bootstrap", Chapman and Hall.
- Enfield, D. B., 1986: Zonal and seasonal variations of the near-surface heat balance of the equatorial Pacific Ocean, *J. Phys. Oceanogr.*, *16*, 1038-1054.
- Esbensen, S. K., and Y. Kushnir, 1981: The heat budget of the global ocean: An atlas based on estimates from surface marine observations, *Rep. 29*, Clim. Res. Inst. Oregon State Univ., Corvallis.
- Fairall, C., E. F. Bradley, D. P. Rogers, J. B. Edson, and G. S. Young, 1996: Bulk parameterizations of air-sea fluxes for TOGA COARE, *J. Geophys. Res.*, *101*, 3747-64.
- Feng M., P. Hacker, and R. Lukas, 1998, Upper Ocean Heat and Salt Balances in Response to a Westerly Wind Burst in the Western Equatorial Pacific during TOGA COARE, *J. Geophys. Res.*, *103*, 10289-10311.
- Freitag, H. P., M. J. McPhaden, C. S. Coho, and A. J. Shepherd, 1991: Equatorial wind, current and temperature data: 180° W to 140° W; April 1983 to October 1987. NOAA Data Report ERL PMEL-35, 116 pp.
- Godfrey, J. S., and E. J. Lindstrom, 1989, The heat budget of the equatorial western Pacific surface mixed layer, *J. Geophys. Res.*, *94*, No. C6, 8007-8017.

- Graham, N. E., and T. P. Barnett, 1987: Sea surface temperature, surface wind divergence, and convection over the tropical oceans, *Science*, 238, 657-659.
- Halpern, D., 1987: Comparison of upper ocean VACM and VMCM observations in the equatorial Pacific. *J. Atmos. Oceanic Technol.*, 4, 84-93.
- Halpern, D., and H. Paul Freitag, 1987: Vertical motion in the upper ocean of the equatorial Pacific, *Oceanologica Acta, Proc. Inter. Symp. On equatorial vertical motion*, 6, 19-26.
- Hamburg, M., (1977) "*Statistical Analysis for Decision Making.*" Harcourt Bruce Jovanich, New York.
- Horel, J. D., and J. M. Wallace, 1981, Planetary-Scale Atmospheric Phenomena Associated with the Southern Oscillation, *Monthly Weather Review*, 813-829.
- Huyer, A., P. M. Kosro, R. O'Malley and J. Fleischbein, 1993. *SEASOAR and CTD observations during a COARE Surveys cruise, W9211C, 22 January to 22 February 1993*, College of Oceanic and Atmospheric Sciences, Oregon State University, Data Report 154, Ref. 93-2. 325 pp.
- Huyer, A., P. Hacker, P. M. Kosro, J. Fleischbein, E. Antonissen and R. O'Malley, 1994. *SEASOAR and CTD observations during a COARE Surveys cruise, W9211A, 8 November to 8 December 1992*, College of Oceanic and Atmospheric Sciences, Oregon State University, Data Report 155, Ref. 94-1. 364 pp.
- Huyer, A., P. M. Kosro, R. Lukas and P. Hacker, 1997. Upper-ocean thermohaline fields near 2°S, 156°E during TOGA-COARE, November 1992 to February 1993. *J. Geophys. Res.*, 102, 12749-12784.
- Inall, M. E., K. J. Richards, and G. Eldin, 1997: The changing structure of the upper ocean in the western equatorial Pacific during TOGA COARE, *submitted to J. Geophys. Res.*
- Joyce, T. M., 1989: On in-situ "Calibration" of shipboard ADCP's: *J. Atmos. Oceanic Technol.*, 169-172.

- Kaneko, A., N. Gohda, H. Nakajima, T. Itoh, K. Kawatate, T. Nagahama and H. Fukukawa, Profiling measurement of the equatorial currents by an ADCP on themooring lines. In: *Preliminary report of the Hakuho Maru Cruise KH-92-5 (TOGA Cruise)*, edited by T. Asai, p.36-55, 1993.
- King, B. A. and E. B. Cooper, 1993: Comparison of ship's heading determined from an array of GPS antennas with heading from conventional gyrocompass measurements. *Deep Sea Research*, 40, 2207-2216.
- Kosro, P. M., 1985: Shipboard acoustic Doppler current profiling during the Coastal Ocean Dynamics Experiment. SIO Reference Series, 85-8, 119pp.
- Kundu, P. K., 1975. Ekman Veering Observed near the Ocean Bottom. *J. Phys. Ocean.*, 6, 238-242.
- Kundu, P. K., and J. S. Allen, Some Three Dimensional Characteristics of Low-Frequency Current Fluctuations near the Oregon Coast, *J. Phys. Oceanogr.*, 181-195, 1976.
- Kutsuwada, K., and H. Inaba, Year-long measurements of upper-ocean currents in the western equatorial Pacific by acoustic Doppler current profilers. *J. Meteorol. Soc. Japan*, 73, 399-409, 1995.
- Léger, C., D. N. Politis, and J. R. Romano, 1992: Bootstrap Technology and Applications, *Technometrics*, 34, 378-397.
- Lien, R., M. J. McPhaden, and D. Hebert, 1994: Intercomparison of ADCP Measurements at 0°, 140° W. *J. Atmos. Oceanic Technol.*, 11, 1334-1349.
- Lukas, R. and E. Lindstrom, 1991: The mixed layer of the western equatorial Pacific Ocean, *J. Geophys. Res.*, 96, (Suppl.) 3343-3358.
- McPhaden, M. J., F. Bahr, Y. Du Penhoat, E. Firing, S. P. Hayes, P. P. Niiler, P. L. Richardson, and J. M. Toole, 1992: The response of the western equatorial Pacific to westerly wind bursts during November 1989 to January 1990. *J. Geophys. Res.*, 97, 14289-14303.

- Meyer, G., J. R. Donguy, R. K. Reed, 1986: Evaporative cooling of the western equatorial Pacific Ocean by Anomalous winds, *Nature*, 323, 523-26.
- Moum, J. N., D. R. Caldwell and C. A. Paulson, 1989: Mixing in the equatorial surface layer and thermocline, *J. Geophys. Res.*, 94, 2005-21.
- Neter, J., W. Wasserman, M. H. Kutner, 1989: "*Applied Linear Regression Models*", 2nd edition, IRWIN.
- Newell, R. E., 1979: Climate and the ocean, *Amer. Sci.*, 67, 405-416.
- Niiler, P., and J. Stevenson, 1982: The heat budget of tropical ocean warm-water pools, *J. Marine Res.*, 40, (suppl.), 465-480.
- Ohlmann, J. C., D. A. Siegel, and L. Washburn, 1997: Radiant heating of the western equatorial Pacific during TOGA COARE, *accepted J. Geophys. Res.*
- O'Malley, R., P. M. Kosro, R. Lukas and A. Huyer, 1994. *Seasoar observations during a COARE Surveys cruise, W9211B, 12 December 1992 to 16 January 1993*. College of Oceanic and Atmospheric Sciences, Oregon State University. Data Report 156, Ref. 94-2, 426 pp.
- Osborn, T. R., 1980, Estimates of the Local Rate of Vertical Diffusion from Dissipation Measurements, *J. Phys. Oceanogr.*, 10, pp. 82-89.
- Peters, H., M. C. Gregg, and J. M. Toole, 1988: On the parameterization of equatorial turbulence, *J. Geophys. Res.*, 93, C2, 1199-1218.
- Pierce, S., J. A. Barth, and Robert L. Smith, 1995: ADCP Data Report: Coastal Jet Separation Project. Oregon State University. Corvallis, Oregon.
- Philander, G. S., 1990: "*El Niño, La Niña, and the Southern Oscillation.*", Academic Press. Princeton, 293pp.
- Plueddemann, A. J., R. P. Trask, W. M. Ostrom, R. A. Weller, B. S. Way, S. Anderson, N. Bogue, J. Shillingford, S. Hill, 1993. TOGA COARE Mooring Deployment, Mooring Check-out and Mooring Recovery Cruises. Woods Hole Oceanographic Inst. Tech. Rept., WHOI-93-30.

- Pollard, R. and Jane Read, 1989: A method for calibrating shipmounted/ acoustic Doppler Profilers and the limitations of gyro compasses., *J. Atmos. Oceanic Technol.*, 6, 859-865.
- Qiao, L., and R. H. Weisberg, 1997: The zonal momentum balance of the equatorial undercurrent in the central Pacific, *J. Phys. Oceanogr.*, 27, 1094-1118.
- Ramanathan, V., and W. Collins, 1991: Thermodynamic regulation of ocean warming by cirrus clouds deduced from observations of the 1987 El Niño, *Nature*, 351, 27-32
- Ramanathan, V., B. Subasilar, G. J. Zhang, W. Conant, R. D. Ces, J. T. Kiehl, H. Grass, and L. Shi, 1995: Warm pool heat budget and shortwave cloud forcing: a missing physics?, *Science*, Vol. 267, 499-503.
- Rasmusson, E. M., and T. H. Carpenter, 1982: Variations in tropical sea surface temperature and surface wind fields associated with the Southern Oscillation/El Niño, *Monthly Weather Review*, Vol. 110, 354-384.
- R. D. Instruments, 1989: Acoustic Doppler current profilers principles of operation: A practical primer.
- Reed, R. K., 1985: An estimate of the climatological heat fluxes over the tropical Pacific Ocean, *J. Climate, Appl. Meteorology.*, 24, 833-840.
- Reynolds, R. W., 1982: A monthly averaged climatology of sea surface temperature, NOAA Tech. Rep. NWS-13, 35pp.
- Rudnick, D. L., and R. E. Davis, 1988: Mass and heat budgets on the northern California continental shelf, *J. Geophys. Res.*, 93, 14013-24.
- Saunders, P. M., and B. King, 1995: Bottom currents derived from a shipborne ADCP on WOCE cruise A11 in the South Atlantic. *J. Phys. Oceanogr.*, 329-347.
- Schramm, R. E, 1989. Experiences with the KVH Compass in RD Instruments Acoustic Doppler Current Profilers. *Oceans.*, 1314-1317.

- Siegel, D. A., J. C. Ohlmann, L. Washburn, R. R. Bidigare, C. T. Nosse, E. Fields, and Y. Zhou, 1995: Solar radiation, phytoplankton pigments and the radiant heating of the equatorial Pacific warm pool, *J. Geophys. Res.*, Vol. 100, No. C3, 4885-4891.
- Short, D. A., P. A. Kucera, B. S. Ferrier, J. C. Gerlach, S. A. Rutledge and O. W. Thiele, 1996: Shipboard radar rainfall patterns within the TOGA COARE IFA. *Bulletin Am. Meteorol. Soc.*, submitted.
- Smyth, W. D., D. Hebert, and J. N. Moum, 1996a: Local ocean response to a multiphase westerly windburst. Part 1: Dynamic response., *J. Geophys. Res.*, 22495-512.
- Smyth, W. D., D. Hebert, and J. N. Moum, 1996b: Local ocean response to a multiphase westerly windburst. Part 2: Thermal and freshwater responses., *J. Geophys. Res.*, 22513-533.
- Stevenson, J. W., and P. P. Niiler, 1983: Upper ocean heat budget during the Hawaii-to-Tahiti shuttle experiment, *J. Phys. Oceanogr.*, 13, 1894-1907.
- Tennekes, H. and J. L. Lumley, 1972: "A First Course in Turbulence", The MIT Press, Cambridge, Mass.
- TOGA COARE International Project Office (TCIPO), 1993: Tropical Ocean - Global Atmosphere Coupled Ocean - Atmosphere Response Experiment Intensive Observing Period Operations Summary, UCAR, P.O. Box 3000, Boulder CO, 80307-3000.
- Waliser and Graham, 1993: Model onset of convection, *J. Geophys. Res.*
- WCRP, 1990: Scientific Plan for the TOGA Coupled Ocean-Atmosphere Response Experiment. WCRP Publications Series No. 3 Addendum, International TOGA Project Office, World Meteorological Organization, C. P. No. 2300, CH-1211 Geneva 2, Switzerland.
- Weare, B. C., P. T. Strub, and M. D. Samuel, 1981: Annual mean surface heat fluxes in the tropical Pacific Ocean, *J. Phys. Oceanogr.*, 705 - 717.

- Webster, P. and R. Lukas, 1992: TOGA COARE: The Coupled Ocean-Atmosphere Response Experiment, *Bull. American Met. Soc.*, 73, No. 9, 1377-1415.
- Weller, R. A. and S. P. Anderson, 1996: Surface meteorology and air-sea fluxes in the western equatorial Pacific warm pool during the TOGA Coupled Ocean-Atmosphere Response Experiment, *Journal of Climate*, 9, 8, 3056-3085.
- Wijesekera, H. W. and M. C. Gregg, 1996: Surface layer response to weak winds, westerly wind bursts, and rain squalls in the western Pacific Warm Pool. *J. Geophys. Res.*, Vol 101, No. C1., p 977-97.
- Zebiak, S.E., and M. A. Cane, 1987: A model El Niño-Southern Oscillation, *Monthly Weather Review*, 115, 2262-2278.

APPENDICES

Appendix A

Bootstrap Statistics

Following Efron and Gong (1983), we calculated bootstrap confidence intervals for the temperature and salinity gradients for each depth bin along the central Seasoar sections. Bootstrapping is a powerful technique used to obtain a non-parametric estimation of statistical error, mainly the bias and standard error of an estimator, or the error rate of a data based prediction rule. Parametric assumptions about the statistical distribution of the data, i.e. normal, log-normal, or chi-squared distributed, do not need to be made. In general, analytic expressions of the variance of a given statistic can be difficult if not impossible to obtain but bootstrapping provides a sample variance estimate of any statistic of interest using Monte Carlo computing methods. Standard parametric techniques for estimating confidence intervals for the linear regressed slope confidence intervals exist (Neter et al., 1989) but require a normality assumption about the statistical distribution of the data. The distribution of temperature and salt in the ocean will not generally follow a given statistical distribution but instead will be complex, nonstationary and in general correlated as dictated by time dependent forcing and turbulent flows.

In our case, the statistic of interest is the linear regressed slope of temperature and salinity along central Seasoar transects. We wish to construct an estimate of the uncertainty in the slope using bootstrapping. The bootstrapping procedure was completed as follows:

1. A bootstrap sample was drawn by independent random sampling, with replacement, from the 37 horizontal bins (4 km bins) along a section at a given depth. Note: Only 19 bins are used for the midscale gradient estimate.
2. Calculate the slope of the best-fit line through the sample points.
3. Repeat steps (1) and (2) to obtain 200 independent bootstrap replications.
4. Order the 200 replications by size.
5. Select the 5th and 195th estimates for the bounds of the 95% confidence limits.

An alternative bootstrapping technique (Efron and Tibshirani, 1993) involves bootstrapping only the residuals from the regression to determine the confidence intervals. This method is superior at estimating the true confidence limit when the data do have a significant linear trend but it can underestimate the confidence limit when a linear model is inappropriate and/or the data are correlated. Other bootstrapping techniques have been developed (De Wet and Van Wyk, 1986; Léger et al., 1992) for first-order and higher order correlated processes, so called autoregressive (AR) processes. Correlation coefficients must be appropriately selected to use these techniques but given the volume of data used in the gradient estimate calculations choosing the appropriate coefficient(s) for each depth bin for each section was prohibitive. The straightforward application of the bootstrapping procedure as we have done tends to be conservative relative to the other methods.

Appendix B

Advection Error Analysis

a. Vertical velocity error analysis

Error estimates of vertical velocity estimated from horizontal divergence have two components: the current measurement error at each platform and, the sampling uncertainty associated with the sparse sampling array. The measurement error can be handled in a straightforward way assuming a least squares error relationship,

$$\delta(\partial w / \partial z) = \{[\delta(\partial u / \partial x)]^2 + [\delta(\partial v / \partial y)]^2\}^{1/2}$$

where δ denotes the error or uncertainty in the quantity. If $u_1 = u_{1m} + \delta u_1$, $u_2 = u_{2m} + \delta u_2$ where u_{1m} and u_{2m} represent the measured currents then,

$$\delta(\partial u / \partial x) = [1 / (x_2 - x_1)] \delta(u_2 - u_1) = [1 / (x_2 - x_1)] \{\delta u_1^2 + \delta u_2^2\}^{1/2}$$

where we note that the relative position error is much less than the relative velocity error, $\delta x / x \ll \delta u / u$. Given a measurement uncertainty of 2 cm s^{-1} for the 32-hour low passed currents and that $\delta(\partial u / \partial x) \sim \delta(\partial v / \partial y)$ we get $\delta(\partial w / \partial z) \sim 0.04 / (x_2 - x_1)$ so that $\delta w \sim 0.04 z / (x_2 - x_1)$. Let $x_2 - x_1 = 1 \times 10^5 \text{ m}$, $dz = 10 \text{ m}$ and since the first bin is at 40 m we have an uncertainty at 40 m of $\delta w \sim 0.4 \text{ m day}^{-1}$. Integrating down to 70 m we have an uncertainty of 1.6 m day^{-1} . In the long-term mean this uncertainty reduces by a factor

$N^{-1/2}$. Given 32 hour filtering we have $N \sim 13$ so that at 70 m we have $\langle \delta w \rangle \sim 0.4 \text{ m day}^{-1}$.

Sampling uncertainty is a more difficult problem given the sparse array and our attempts to estimate it are given in the main text. Meanders in the large scale flow relative to the sampling array could lead to significant apparent vertical flow which would be an artifact of the sampling and not the flow itself. We have tried to estimate the sampling uncertainty by calculating w from different estimates of the horizontal divergence (Fig. 15b).

b. Complex empirical orthogonal functions (CEOF)

Following Kundu and Allen (1976) we calculated the Complex Empirical Orthogonal Functions (CEOF's) to construct the CEOF filtered currents and estimated vertical velocity from the horizontal divergence calculated from the CEOF-filtered currents.

For vector quantities, such as ocean current vectors, the dominant modes of variability may be expressed as CEOF's. In particular, we can write the individual zonal and meridional vectors in complex format,

$$w(x_j, t_k) = u(x_j, t_k) + iv(x_j, t_k),$$

where $k=1, \dots, K$ hours, and $j = 1, \dots, N$ locations. The correlation matrix is given by,

$$R(x_m, x_n) = \frac{1}{K} \sum_{k=1}^K w^*(x_m, t_k) w(x_n, t_k)$$

which is Hermitian so the eigenvectors are orthogonal and the eigenvalues are real. The eigenvectors or modes are obtained by solving the eigenvalue equation,

$$\sum_{i=1}^N R(x_i, x_j) \varphi_n(x_i) = \lambda_n \varphi_n(x_j)$$

where φ_n represents the eigenvector of the correlation matrix and λ_n is its eigenvalue. So then the original vector, w , may be expanded in terms of the eigenmodes,

$$w(x_i, t_k) = \sum_{n=1}^N E_n(t_k) \varphi_n(x_i) ,$$

and the complex amplitudes, $E_n(t_k)$, are obtained by,

$$E_n(t_k) = \sum_{i=1}^N \varphi_n(x_i) w(x_i, t_k)$$

One can then analyze the form or shape (orientation and magnitude) of the individual eigenmodes which may represent dynamical modes of the system. The individual components of the velocity vector may also be expressed in terms of the CEOF's, i.e. $u = Re(w)$, $v = Im(w)$. In our study, the vertical velocity estimates calculated from the CEOF filtered divergence estimates did not differ markedly from the first method and are discussed in the body of the text.

c. Error analysis for horizontal advection

The advection error estimates were calculated using linear error assumptions, i.e. the errors in the currents and gradients were assumed important only to first order in the Taylor series expansion. The total horizontal heat advection per unit depth can be written as follows, omitting density and specific heat:

$$\begin{aligned} u \partial T / \partial x + v \partial T / \partial y &\approx [u' + \delta u'][(\partial T / \partial x)' + \delta(\partial T / \partial x)'] + [v' + \delta v'][(\partial T / \partial y)' \\ &\quad + \delta(\partial T / \partial y)'] \\ &= u' (\partial T / \partial x)' + v' (\partial T / \partial y)' + u' \delta(\partial T / \partial x)' + v' \delta(\partial T / \partial y)' \\ &\quad + \delta u' (\partial T / \partial x)' + \delta v' (\partial T / \partial y)' + O(\delta^2) \end{aligned}$$

where the unprimed terms on the left represent the true ocean horizontal advection and the primed terms represent the constructed estimate. The first two primed terms on the left represent the horizontal advection estimate and the remaining four terms account for the uncertainty of that estimate. A similar result is obtained for salinity. The error in the gradient estimates calculated from bootstrap statistics is discussed in Appendix A. We estimate the measurement and sampling uncertainty in the low passed currents at 2 cm s⁻¹ based on a comparison of the central mooring current data and R/V Moana Wave ADCP data for W9211A and W9211B (Appendix E). Correlation and the EOF analysis suggests that the UOP mooring current data are reasonably representative of the butterfly domain and the horizontal temperature and salinity gradients from Seasoar data are therefore reasonable for estimating horizontal advection at the butterfly center. If the flow field was strongly horizontally structured the use of gradients on scales larger than the flow field structure would be

inappropriate since horizontal shears would tend to distort the thermohaline field as it advected. The instrumental measurement error of temperature and salinity, 0.01 °C and 0.01 psu, contributes to a gradient error of about an order of magnitude less than the uncertainty obtained from the bootstrap uncertainty in the gradient estimate.

The horizontal advection error bars accompanying the individual cruise mean estimates in Tables 2.3 and 2.4 were calculated by computing the average advection uncertainty for the entire cruise and dividing it by the square root of the number of occupations of the least occupied central transect line for which advection estimates could be made. The divisor was chosen as such since it nominally represents the square root of the degrees of freedom in the data set. For W9211A this divisor was 3 since the zonal transect was occupied 9 times. For W9211B and W9211C it was 3.3 and 3.2, respectively. The vertical advection uncertainty estimates are discussed in the text.

d. Sampling gaps and temporal-spatial aliasing of the diurnal signal and internal tide

On a few occasions the temporal gap between successive Seasoar occupations of a given transect was longer than 2 days. For these cases the advection estimate should be regarded cautiously because the advection time scale from the butterfly apices to the center, with a 40 cm s⁻¹ current, is $t \approx 65\text{km}/40\text{cm s}^{-1} = 1.9$ days. Low-passed zonal currents of stronger than 40 cm s⁻¹ are not uncommon in this region and even meridional currents occasionally had magnitudes as large as 40 cm s⁻¹. Feng et al. (1998),

however, used a three day averaging window to estimate advection and do not appear to have any difficulty resolving the dominant advective features so the 1.9 day criteria given above is probably too conservative for these data.

Sampling errors due to the synoptic diurnal surface heating signal and internal tide, which has a period of 12.5 hours and wavelength of about 100 km, present a serious aliasing problem for estimating the horizontal gradient with data from a moving platform, particularly when the surface mixed layer and the thermocline are shallow. Given the along transect sampling time and the strength of the diurnal heat cycle, significant aliasing of the synoptic diurnal signal into a spatial signal can occur and is given by, $\partial T(z)/\partial x = Q(z)/(\rho c_p u_{\text{ship}})$, where $Q(z)$ is the net synoptic flux, u_{ship} is the ship speed. Integrating over a mixed layer depth h we get, $\partial T/\partial x = [Q(0)-Q(-h)]/(\rho c_p u_{\text{ship}} h)$. For example, during the midday we could expect that, $Q(0)-Q(-h) \sim 400 \text{ Wm}^{-2}$ and $u_{\text{ship}} \sim 4 \text{ ms}^{-1}$ we get an apparent spatial gradient of $2.5 \times 10^{-5} \text{ }^\circ\text{C/h}$. For $h = 10 \text{ m}$, we find that the aliased gradient is $0.25 \text{ }^\circ\text{C}/100 \text{ km}$ which turns out to be about the same magnitude as the estimated linear regressed gradients. The aliasing becomes less important as the magnitude of Q decreases and/or h increases. Errors in the horizontal gradients due to thermocline motion may be large and our approach to minimize them is to try to keep the depth of integration above excursions of the thermocline.

To avoid the aliasing problems described above an alternative approach for calculating the gradients using data from two separated platforms was considered. Hourly binned temperature from the Wecoma and Moana Wave was used to construct two point differenced gradient estimates along the transect between the platforms. While these estimates

are free of temporal-spatial aliasing they are sensitive to small-scale spatial variability and subsequently too noisy to be useful.

Appendix C

Spectral Method for Estimating Heat and Salt Storage

The temperature and salinity time series of a given surface layer can have large variability on hour to several hour time scales (Fig. 3.2) and attempts to use finite differences to estimate temporal derivatives can substantially underestimate the true derivative. As an example, consider a layer temperature with sinusoidal variability of the form $A\sin(2\pi t/\tau)$. The ratio of the finite differenced derivative, $f'_D(t)$, to the analytic result, $f'(t)$, is given by,

$$f'_D(t) / f'(t) = \sin(2\pi\Delta t/\tau) / (2\pi\Delta t/\tau) \quad (C1)$$

where Δt is the time step (1 hour) and τ is the period of the process of interest (Haltiner and Williams, 1980). For $\tau = 2$ hours, the ratio is identically zero and for $\tau = 4, 6, 8, 12$ hours the finite differenced derivative equals respectively 63.6%, 82.6%, 90.0%, and 95.4% of the true derivative. Such errors in temporal derivatives are problematic for storage terms in variable depth layer calculations since $T(t)$ and $h(t)$, and by extension $\partial T / \partial t$ and $h(t)$, are usually correlated as are $S(t)$ and $h(t)$. Smoothing of the T and S data prior to differencing is appealing but doing so eliminates potentially significant correlation that may contribute to the storage term. Consider a Reynolds decomposition of one component of the heat storage term,

$$\langle h(t) \partial T_a / \partial t \rangle = \langle h \rangle \langle \partial T_a / \partial t \rangle + \langle h' (\partial T_a / \partial t)' \rangle \quad (C2)$$

where the angle brackets represent a time average and the primes represent deviations from that average. Clearly, if the temperature or salinity time series is "noisy" the discrete time derivatives will not be representative of the true derivative and the second term on the right hand side of Eqn. C2 will be poorly estimated. If high frequency correlations are known to be unimportant for the long term average then smoothing of the data prior to differencing could be used. In general, it is not clear if the high frequency components can be neglected unless one simply selects a level of smoothing that serves to balance the budget. Instead, we consider a novel approach employing spectral methods to avoid the spectral truncation imposed by time domain finite differences. As a note, for a fixed depth layer, errors associated with discretization are inconsequential in the long term mean since h is constant (i.e. $\langle h' (\partial T_a / \partial t)' \rangle = 0$) and only the two first and two last temperature or salinity data points survive the averaging summation.

For the variable depth layer problem we can recast the left hand side of (C2) by calculating the zero lagged cross-correlation between $h(t)$ and $\partial T_a / \partial t$ using spectral methods that avoid estimating an explicit discrete time derivative. The cross-correlation, $R_{xy'}(\lambda)$, where $x = h(t)$ and $y' = \partial T_a(t) / \partial t$, can be expressed in the frequency domain as,

$$R_{xy'}(\lambda) = [1/(N - \lambda)] \sum_{n=1}^{N-\lambda} h(t_n) \frac{\partial T_a(t_n + \lambda)}{\partial t} = \sum_{j=1}^{\frac{N-\lambda}{2}+1} G_{xy'}(\omega_j) \exp(2\pi i \omega_j \lambda) \Delta \omega_j \quad (C3)$$

where $G_{xy'}(\omega_j)$ is the cross spectral density at frequency ω_j and λ is the lag.

Noting that $G_{xy'} = 2\pi i \omega_j G_{xy}$ and $\lambda = 0$, we find,

$$\left\langle h(t) \frac{\partial T_a}{\partial t} \right\rangle = \sum_j^{\frac{N}{2}+1} \operatorname{Re}\{G_{xy'}(\omega_j)\} \Delta\omega_j + DC =$$

$$2\pi \sum_j^{\frac{N}{2}+1} \omega_j \operatorname{Re}\{iG_{xy}(\omega_j)\} \Delta\omega_j + DC = 2\pi \sum_j^{\frac{N}{2}+1} \omega_j \{-Q_{xy}(\omega_j)\} \Delta\omega_j + DC \quad (C4)$$

where Q_{xy} is the quadrature spectral density which is a function of the cross-spectral density of $h(t)$ and $T_a(t)$, and not $\partial T_a / \partial t$. When using the spectral method, a "DC" or zero frequency component must be added to the sum to account for the detrending of the time series that must be performed to compute the cross-spectral estimate. As an aside, the spectral approach gives us insight into the nature of the processes and we can readily calculate gain factors, $g(\omega_j) = Q(\omega_j) / \{\omega_j \{-Q_{xy}(\omega_j)\} \Delta\omega_j\} \rho_{CP}$, where $Q(\omega_j)$ is the spectral representation of a given process.

We can estimate the uncertainty in the spectral estimate noting that G_{xy} is a unbiased estimator and using the variance of $Q_{xy}(\omega_j)$ as a measure of the random error of Eqn. 4C1 (Biendat and Piersol, 1986). The variance is given by, $\operatorname{Var}(Q_{xy}(\omega_j)) = 0.5 (G_{xx} G_{yy} + Q_{xy}^2 - C_{xy}^2)$ where G represents the modulus of the power spectral density, Q_{xy}^2 is the quadrature spectral density, and C_{xy}^2 is the co-spectral density. To estimate the uncertainty in the storage term we replace the spectral estimate of $Q_{xy}(\omega_j)$ in 4C1 with the standard deviation of $Q_{xy}(\omega_j)$ calculated from the variance and sum the frequency series as before. The confidence intervals given in Tables 3.3a and 3.3b are 95% confidence bounds.

The phase lag between $h(t)$ and $T(t)$ is very important and is illustrated with a simple example given sinusoidal behavior for $h(t)$ and $T_a(t)$; given that, $T_a(t) = -T_o \sin(\omega t + \text{lag}) + \langle T \rangle$, $h(t) = h_o \sin(\omega t) + \langle h \rangle$ where the angle brackets refer to the time average the component of the storage

term $\langle h(t) \partial T_s / \partial t \rangle = -0.5\omega h_o T_o \sin(\text{lag})$, is readily calculated. The sign of the lag can change the sign of the storage term and if the lag is zero there is no heat storage change at that frequency. The lag between $h(t)$ and the derivative of T or S is fundamental to the process and must be non-zero to have a non-zero change in storage. The spectrally averaged phase lag between $h(t)$ and $T(t)$ at each spectral frequency can be calculated from the co-spectral and quadrature spectral estimates and is given by, $\theta_{xy}(\omega) = \tan^{-1}(Q_{xy}(\omega)/C_{xy}(\omega))$. A standard error estimate for the phase is obtained from the coherence and is given by, $\text{s.d.}[\theta_{xy}(\omega)] = (1-\gamma_{xy}^2)^{1/2} / (|\gamma_{xy}| (2n_d)^{1/2})$ where γ_{xy}^2 is the coherence-squared and n_d is the degrees of freedom given by the number of independent spectral ensembles used to estimate the spectral estimators. In our case n_d was equal to 6. The phase between $h(t)$ and $T(t)$ at each frequency is shown in Figures 3.8, 3.9, and 3.12 along with standard error estimates. For W9211A and W9211B the spectral estimates near the diurnal frequency indicate that heat was removed from the surface mixed layer because T and h are anti-correlated and h leads T by ~ 1 hour at the diurnal frequency; one plausible explanation is that during the heating phase the layer shoals concentrating the radiant energy in a smaller volume such that the temperature response may initially be relatively small compared to the change in depth. During the cooling phase the layer deepens by buoyancy inversion brought about by surface cooling such that as h increases warmer water is entrained from below. The spectral estimates, as calculated, cannot discern between day and night but time-lag correlation calculations of $h(t)$ and $T(t)$ for the 12 hour day time heating interval from 0600 to 1800 and the night time cooling interval from 1800 to 0600 are consistent with the description given above. During W9211C the spectrally averaged phase lag at the diurnal frequency was not significantly different than zero but the lag near the semi-diurnal frequency, where

there was a strong heat storage flux, was ~ 2 hrs. Interestingly, there is also a ~ 2 hr lag at the semidiurnal frequency for W9211A and W9211B but the heat storage flux is not as strong compared to the diurnal frequency. One speculation is that the semi-diurnal tide during W9211C was associated with soliton-like waves in the thermocline region that may have caused mixing near the SML base but it is not clear why there would be a 2 hour lag between $h(t)$ and $T(t)$. Another explanation may be that the diurnal response of $h(t)$ and $T(t)$ was strongly non-sinusoidal such that the spectral representation of the diurnal signal required higher mode components. This latter explanation would be consistent with the day time heating and night time cooling mechanism suggested above and explain the lagged response.

Spectral methods are valid for periodic stationary time series and as can be seen by reviewing the time series of h and T (Fig. 3.2) we are working marginally within these assumptions. Indeed, the problem of estimating the budget over a variable depth layer appears ill-posed given non-continuous non-stationary data. If the temperature and salinity time series are reasonably smooth regardless of stationarity, the time discretization approach is reasonable and when the time series are "noisy" but stationary, the cross-spectral method is applicable. Both the time domain and spectral domain approach give null results for variability at the Nyquist frequency, $(2 \text{ hrs})^{-1}$.

Appendix D

Heat and Salt Flux Error Analysis

In calculating the ocean budget we must investigate the expected contribution from sampling and measurement errors. We must also consider the error associated with the assumptions made in the theoretical formulation of the budget although these errors are in fact sampling errors (i.e. the data set may be insufficient to independently estimate all of the significant terms in the heat and/or salt balance).

Sampling errors

During periods of high spatial heterogeneity in the thermohaline field, such as W9211A, point estimates of the heat and salt storage terms as well as the other flux terms may not be a representative of the larger domain over which advection is estimated. The tidal structure can also strongly influence heterogeneity of the thermohaline and current field on semi-diurnal and diurnal time scales. An alternative estimate of the storage terms can be made using averaged Seasoar section data but averaging can smooth out important structure in the thermohaline field and substantially limit the temporal resolution. Similar considerations need to be made for the surface, penetrative radiant, and turbulent fluxes. Spatial surface flux variability can result from heterogeneity in cloud cover and wind stress for example. Spatial variability in the penetrative and turbulent fluxes can result from variations in the ocean stratification, current shear, wind forcing, and variability in surface fluxes. In the body

of the text and in tables we site the comparison of the fluxes and storage terms between the R/V Moana Wave, R/V Wecoma, and UOP mooring to assess the spatial inhomogeneity. In the case of turbulent flux there is only one estimate which is taken by definition to be representative. This may be a dangerous assumption given the time and space intermittency of oceanic turbulence. Spatial variability in the advection fluxes present an intriguing dilemma. Advection only occurs when there is spatial variability in the thermohaline field but if the thermohaline field is smoothly varying and the current field is relatively spatially uniform we expect that spatial variability of the advective flux is small. Errors associated with the advection estimates used in this work have been previously discussed and estimated in chapter 2.

Measurement errors

Typical measurement accuracy of the Seasoar 1.0 Hz temperature and salinity are, $\delta T = \pm 0.01$ °C and $\delta S = \pm 0.01$ psu, respectively (Huyer et al., 1996). Microstructure temperature and salinity measurements are somewhat more accurate. The vertically integrated heat content uncertainty is then $\delta H = \rho c_p h \delta T N^{-1/2}$ and the uncertainty in the average salt content is $\delta S N^{-1/2}$ where N is the number of samples of T and S in the water column, h. For a 50 m column $N \sim 25-50$ (1-2 m/sec ascent rate) so that $\delta H \sim \pm 0.29-0.4$ Mjoules. If we difference two casts separated by an hour to get the storage heat flux we get an error of $\delta \delta H / \delta t = \pm 80$ to 110 Wm⁻². In estimating fluxes this gives an unacceptably high error without additional averaging. We can improve the hourly uncertainty estimates by performing several casts/hour as was done. Given six

casts/hour we get a reduction of the error, $\delta\partial H/\partial t = \pm 33$ to 45 Wm^{-2} , which is still relatively large but not compared to the observed $\partial H/\partial t \sim \pm 100$ - 1000 Wm^{-2} estimated from hourly differences. Low-pass filtering of the rate of change of the heat and salt storage terms to remove high frequency variability and reduce the uncertainty is absolutely necessary to obtain interpretable results. In this work we applied a 32-hour FFT filter which gives a reduction of error by a factor of 1/4 so that the uncertainty in the low passed result is $\delta\partial H/\partial t \sim \pm 8$ to 12 Wm^{-2} which is reasonable. For a survey period of 20 days the measurement uncertainty reduces to $\sim \pm 2 \text{ Wm}^{-2}$ so the measurement error of the storage term is much smaller than the sampling error. For the 50 m rate of change of average salinity we have an uncertainty of less than $0.001 \text{ psu hr}^{-1}$ before low passing the data. To normalize this flux to a surface flux value we must multiply by 50 so the surface equivalent uncertainty in the flux is $0.05 \text{ psu hr}^{-1} \text{ m}^{-2}$. After filtering at 32 hours we get an equivalent uncertainty in the surface equivalent salinity flux of $\sim 0.012 \text{ psu hr}^{-1} \text{ m}^{-2}$ which amounts to an uncertainty of less than 4 cm in the 20 day accumulated storage term.

The accuracy of the surface flux measurements need to be considered for each type of measurements. Typical values of shortwave and longwave radiation measurement uncertainties are $\pm 10 \text{ Wm}^{-2}$ and Table 3.1 shows that the cruise average radiative flux from the three surface meteorology platforms used in this study agree from within a few Wm^{-2} (Moana Wave and UOP) to 15 to 20 Wm^{-2} (Wecoma). The differences between the Wecoma and the other platforms may be largely due to spatial variability in cloud cover over the butterfly pattern. Differences in the latent heat and sensible heat fluxes are relatively small, a few Wm^{-2} , except for the W9211C comparison when Moana Wave spent only 1 week in the butterfly domain. Differences in the net flux for each budget period range

from 1 to 15 Wm⁻² (Table 3.1). The uncertainty in the penetrative heat flux is a subject of current research but is probably less than ± 10 Wm⁻² below 30 m. For layer depths of 5 m or less, large uncertainties in the penetrative term are possible and is the subject of current research (C. Ohlmann, pers. comm.).

Surface precipitation measurement uncertainties vary widely depending on the type of instrument used. Shipborne Doppler radar estimates differ by a factor of 2 less than ship and mooring measurements which themselves differ by more than $\sim 30\%$ (Short et al., 1996; Bradley and Weller, 1996). Part of the differences are real and are associated with patchiness in the rainfall but some of the difference may attributable to measurement error in the estimated rainfall. As summarized in Table 3.2, the precipitation differed by as much as 50% for the rainfall estimates from the three platforms used in this study.

Budget formulation considerations:

The component of the entrainment term, $\rho c_p (T_a - T_h) \partial h / \partial t$, implicit in Eqn. 3.1 can dominate the UOL budget by 100's Wm⁻² but these fluxes are largely adiabatic in contrast to the SML where this term is small on average, $O(1 \text{ Wm}^{-2})$, and changes in h are largely due to non-adiabatic processes, ie. they change the average layer temperature and salinity. By time averaging we can reduce some of the adiabatic noise in the UOL budget. The term representing horizontal advection of layer depth,

$$\rho c_p (T_a - T_h) \left(u_{-h} \frac{\partial h}{\partial x} + v_{-h} \frac{\partial h}{\partial y} \right), \text{ in Eqn. 3.3 and implicit in Eqn. 3.1 can}$$

contribute $\sim 50 \text{ Wm}^{-2}$ given $T_a - T_h \sim 1^\circ\text{C}$, a current of $\sim 0.1 \text{ ms}^{-1}$, and a mean gradient in layer depth of 5m/100km, but we can only estimate this term as

a residual. In the SML, vertical velocity is $\sim 2 \text{ m day}^{-1}$ and $T_a - T_{s,h} \sim 0.03 \text{ }^\circ\text{C}$ so that the $w_{s,h}$ term contributes $O(3.0 \text{ Wm}^{-2})$ and if $u_{s,h} = 0.3 \text{ m s}^{-1}$ and assuming $\nabla_H h = 5.0 \text{ m/100 km}$, layer depth advection gives a heating rate of $O(2.0 \text{ Wm}^{-2})$. By comparison, $\partial h / \partial t \sim 40 \text{ m day}^{-1}$ in response to the diurnal cycle so that $\partial h / \partial t$ dominates the entrainment term which is driven by the competing effects of turbulent diffusion and buoyancy forcing.

Budget summary box plots

The remaining section of this appendix contains summary box plots of the heat and freshwater budgets. These box plots provide a graphic depiction of Tables 3.4 and 3.5 which contain all of the average heat and freshwater budget results for each of the survey cruises and for the three cruise average. Please see the main text for a discussion of each specific budget.



W9211A Average Heat Fluxes

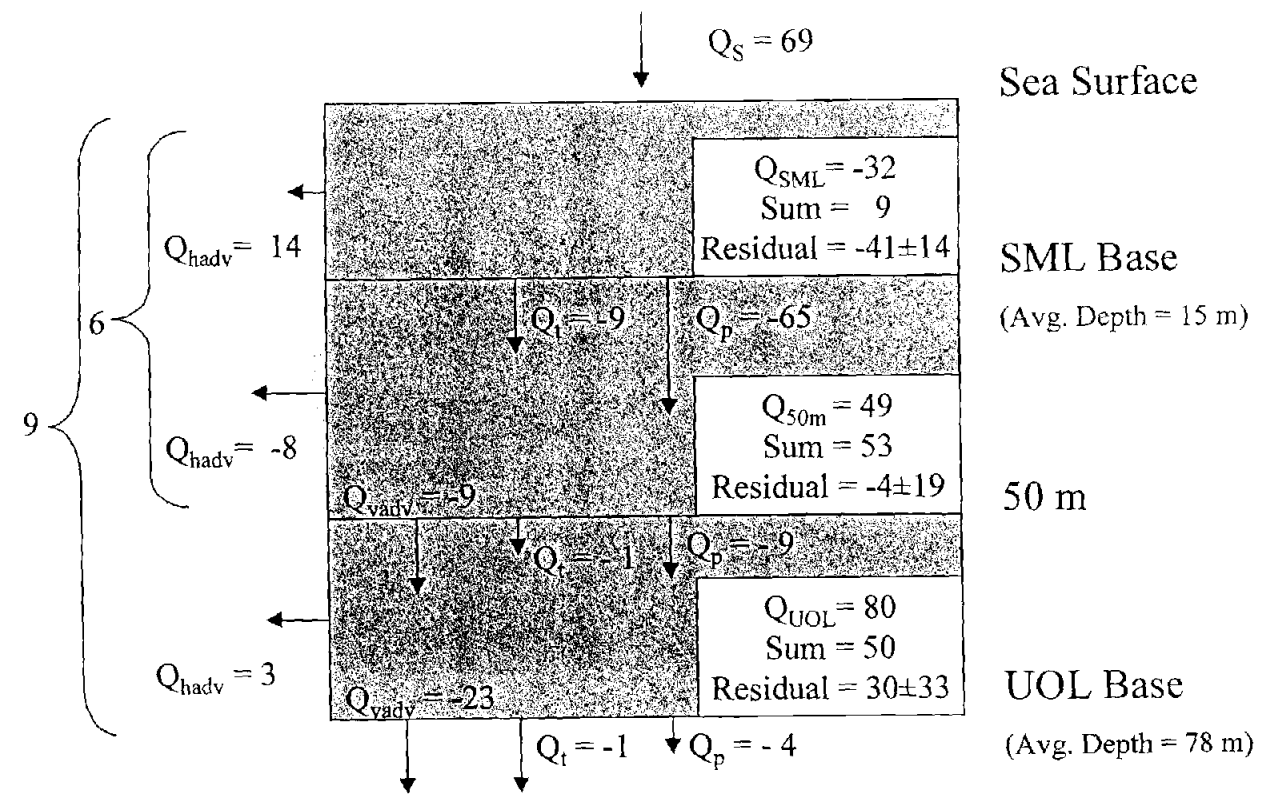


Figure D1. Summary heat budget box plot for W9211A.

W9211B Average Heat Fluxes

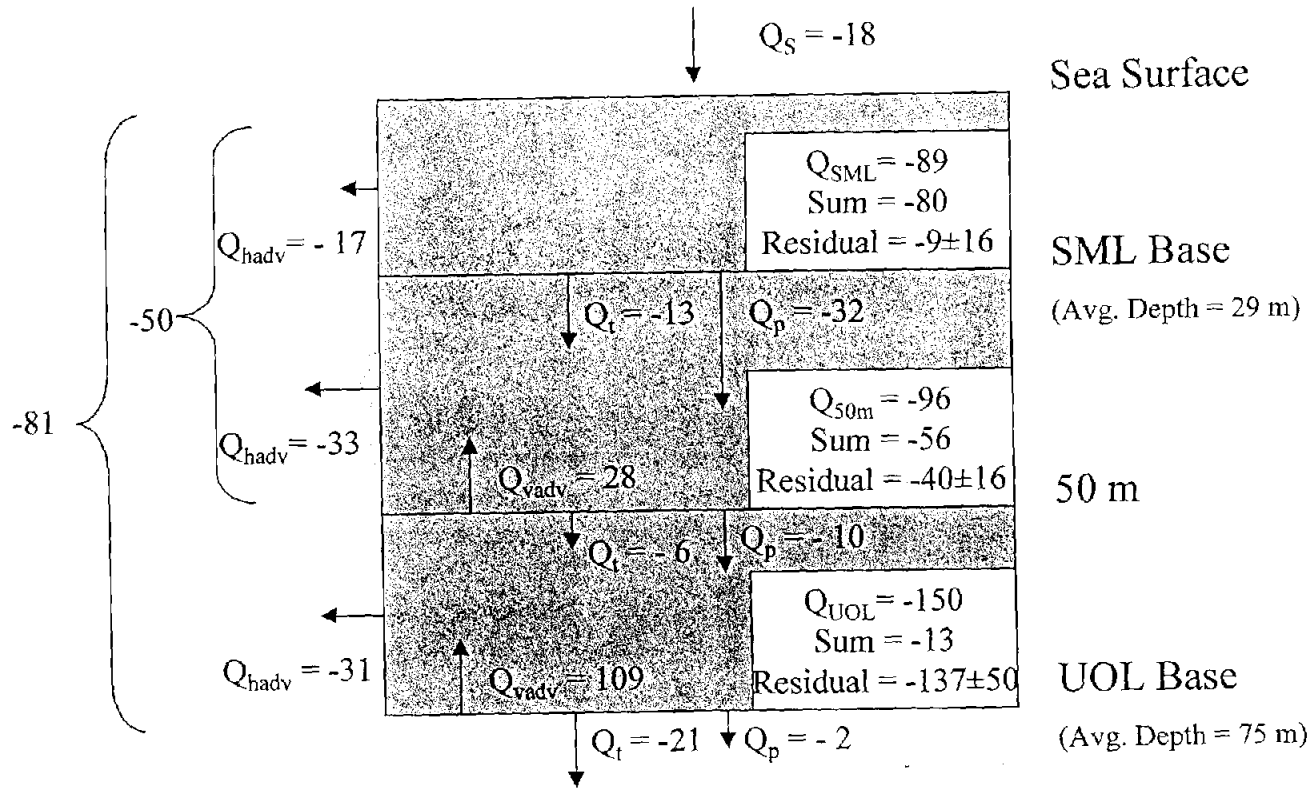


Figure D2. Summary heat budget box plot for W9211B.

W9211C Average Heat Fluxes

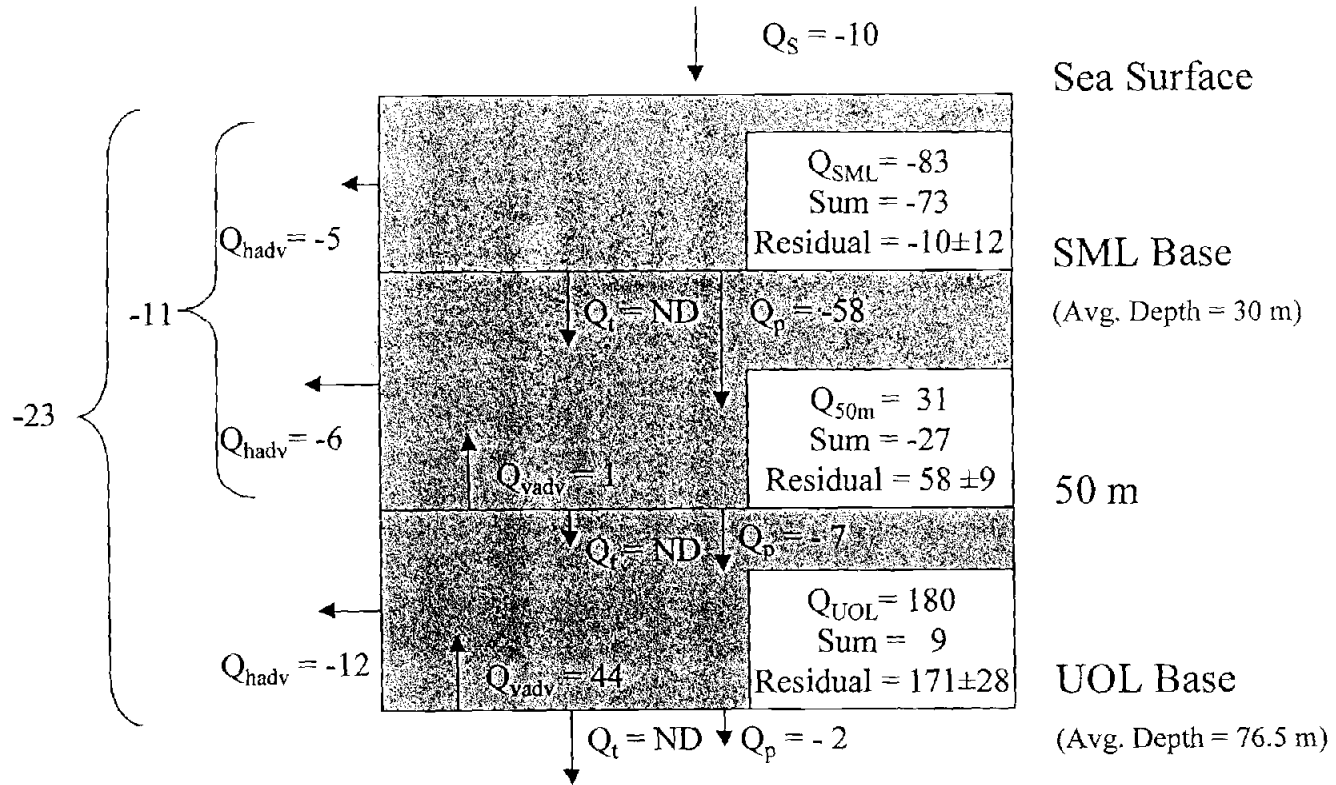


Figure D3. Summary heat budget box plot for W9211C.

Overall Average Heat Fluxes

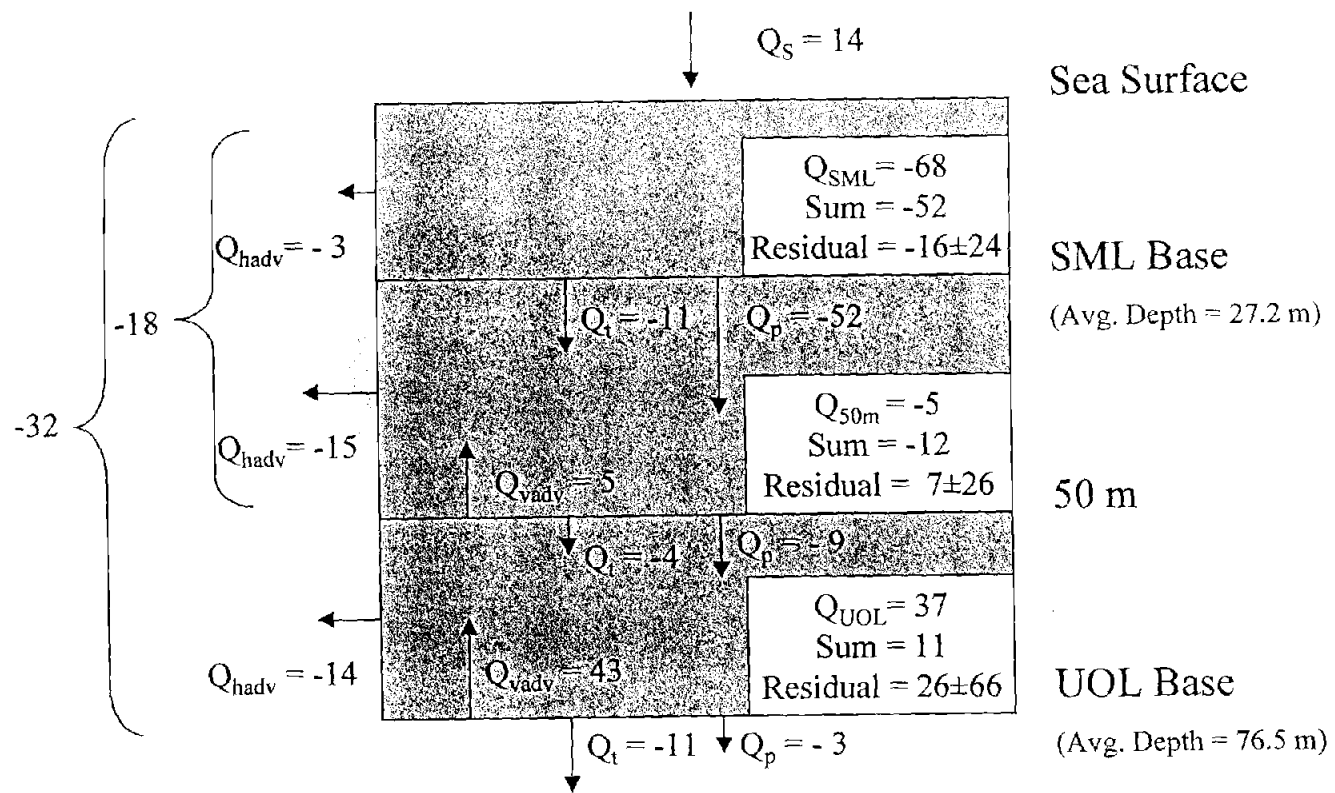


Figure D4. Summary heat budget box plot for three-cruise average.

Figure D5. Summary freshwater budget box plot for W9211A.

W9211A Cumulative Freshwater Fluxes (cm)

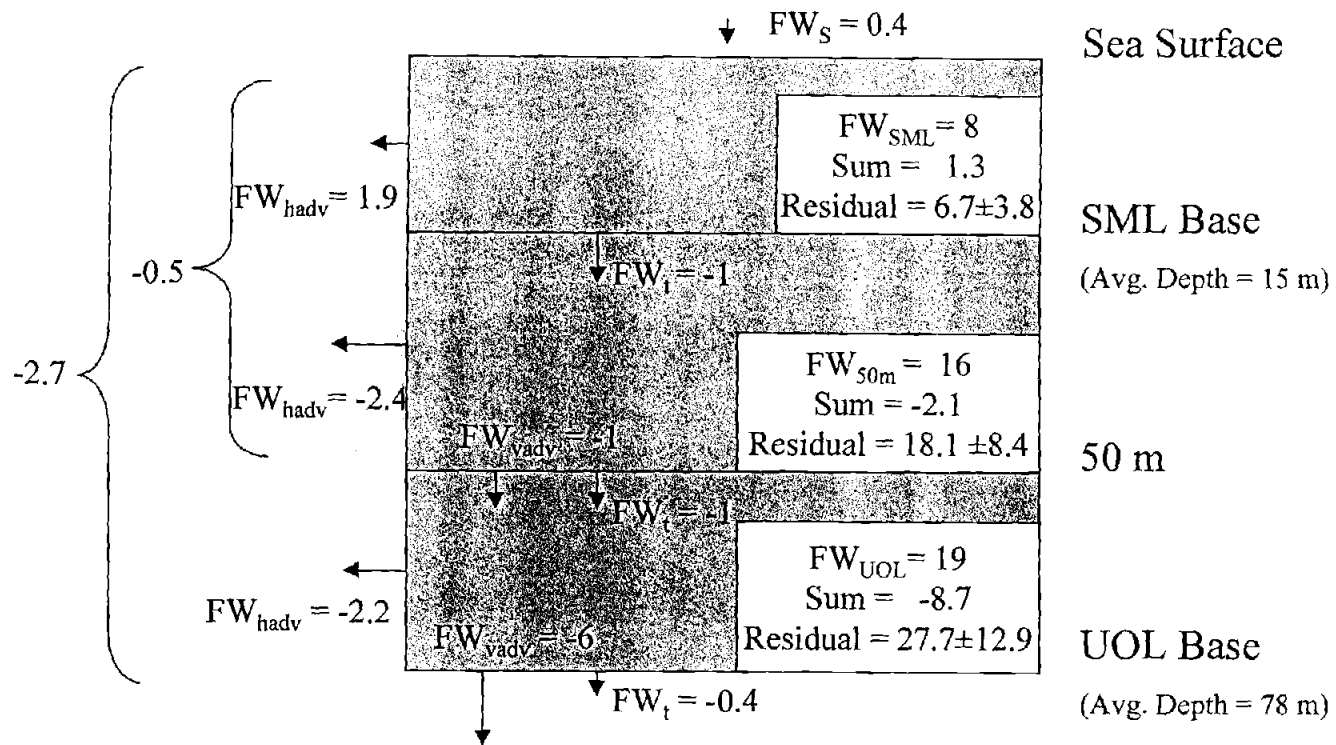
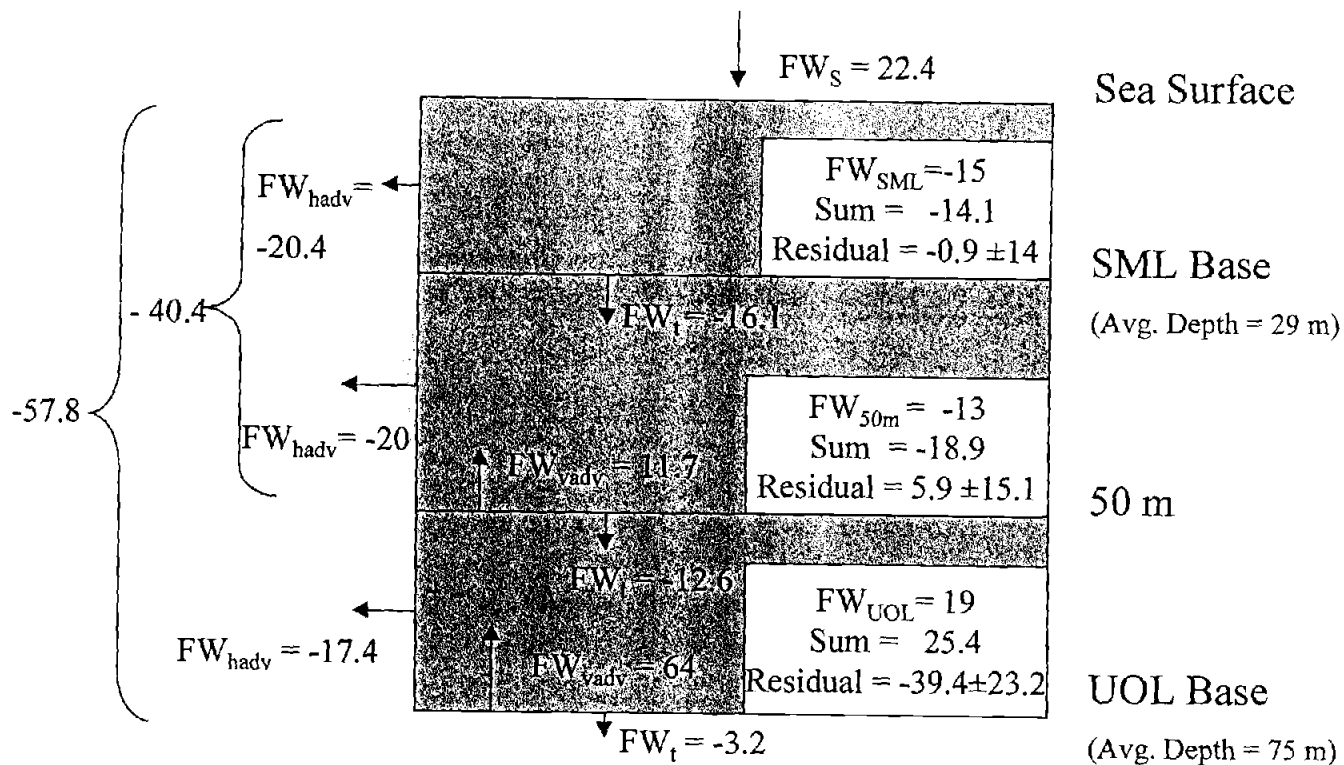


Figure D6. Summary freshwater budget box plot for W9211B.

W9211B Cumulative Freshwater Fluxes (cm)



W9211C Cumulative Freshwater Fluxes (cm)

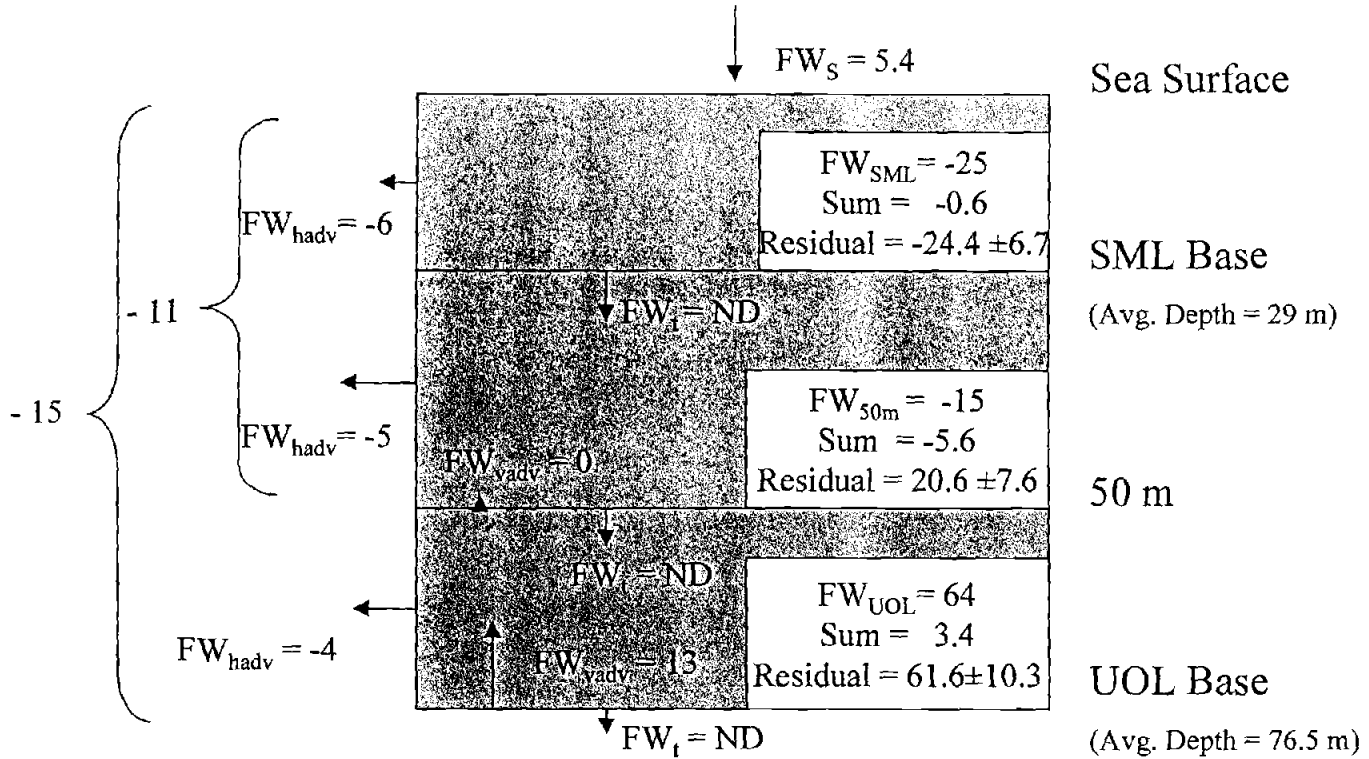
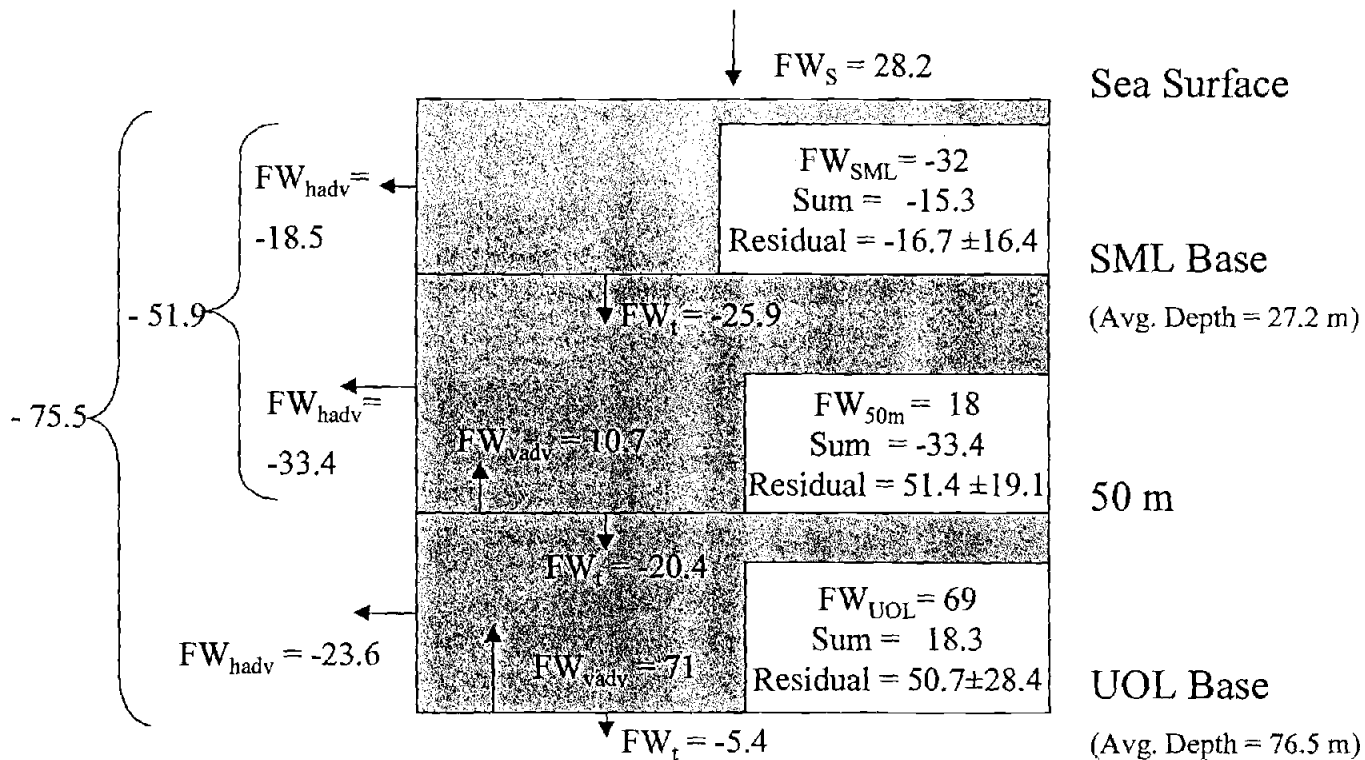


Figure D7. Summary freshwater budget box plot for W9211C.

Figure D8. Summary freshwater budget box plot for three-cruise average.

Overall Cumulative Freshwater Fluxes (cm)



Appendix E

Investigation of Shipborne ADCP Direction Accuracy: Comparison of Moana Wave and WHOI UOP Mooring Current Data for the TOGA COARE IOP

During the Intensive Observing Period (IOP) phase of the Tropical Ocean Global Atmosphere (TOGA) Coupled Ocean-Atmosphere Response Experiment (COARE) the R/V Moana Wave made a variety of measurements for two periods exceeding 20 days each while positioned within 10 km of the WHOI Upper Ocean Processes (UOP) mooring at 1.75 S, 156.0 E (Plueddemann, 1993). In particular, the Moana Wave acquired ocean current data with an RD Instruments (RDI) 153 kHz ADCP mounted in its hull. The WHOI UOP mooring was equipped with VMCM's and a downward looking RDI 153 kHz ADCP. A comparison of the current profiles between the platforms suggested that the magnitude of the differences warranted a systematic scrutiny of the two data sets to determine if the differences were within tolerable error. The purpose of this note is to present the results of the investigation of the differences between the measured current profiles from the two observation platforms.

Many researchers have investigated both the magnitude and directional accuracy of shipborne ADCP measurements and some have made comparisons with moored VMCM's and VACM's as well as moored ADCP measurements. The absolute directional accuracy of shipborne ADCP measurements and moored current meter measurements is reviewed along with a comparative analysis of the UOP mooring current data and Moana Wave current data. Based on the review, the robustness of the differences seen in the UOP and Moana Wave current velocity data

comparisons is determined and a corrective recommendation is offered for the WHOI UOP data set.

Background

During the COARE IOP the R/V Moana Wave maintained a position within about 10 km of the WHOI UOP mooring from November 11 to December 3 and from December 19 to January 11. The Moana Wave measured currents using an RDI 153 kHz ADCP operated with a 16 (8) meter pulse length and a 8 (4) meter bin during leg 1 (leg 2) giving an effective trapezoidal filter with a 24 (12) meter base. The Moana Wave data used in this study was provided by the NODC Hawaii Archive Center and was gridded in nominally 10 meter bins with the shallowest bin centered at 20 meters. The UOP mooring had VMCM's located at 13.0, 17.0, 31.5, 39.5, and 52.5 meters, and a downward looking 153 kHz RDI ADCP at 20.5 meters operating with a 16 meter pulse length and 16 meter bin giving an effective triangular filter with a 32 meter base. The UOP ADCP data provided for this study had its first bin center located at about 69 meters. The data bin lengths were scaled with a mean speed of sound correction of 1524.5 m/s using the factor $1524.5/1470$ thus giving a about a 16.4 meter bin for the UOP ADCP data. A comparison of the mean zonal and meridional current profiles for legs 1 and 2 suggested that the calculated ADCP currents from the UOP mooring were rotated relative to the Moana Wave data (Fig. E1). Note that the finer vertical structure seen in the Moana Wave data is due to the finer resolution of the shipborne ADCP. The difference profiles from 12 ADCP bins and the 5 VMCM bins are provided in figure 2.

Two methods were used to determine the directional correlation of the current vectors measured by the two platforms. The first method simply rotates the UOP mooring data by the following rotation operation:

$$u_{\text{rotated}} = u_{\text{uop}} \cos \theta + v_{\text{uop}} \sin \theta$$

$$v_{\text{rotated}} = -u_{\text{uop}} \sin \theta + v_{\text{uop}} \cos \theta$$

and then searches for the maximum angular correlation given by,

$$\max \langle u_{\text{rotated}} u_{\text{mw}} \rangle, \text{ and similarly for } v.$$

Using this approach we get two estimates, albeit not independent, of the relative rotation of one platform to the other. We averaged the two estimates to get a single relative rotation estimate for each depth bin. Further, the moored ADCP/Ship ADCP bin rotations were vertically averaged to get an estimate of the relative rotation of the moored ADCP to the ship's ADCP.

The second method, which follows Kundu (1975), calculates the average veering angle between the two platforms by using the complex correlation coefficient. If we define the two dimensional current velocity vector as,

$$w(t) = u(t) + iv(t),$$

the complex correlation coefficient between two vector series is given by,

$$\rho = \langle w_1^*(t) w_2(t) \rangle / (\langle w_1^*(t) w_1(t) \rangle^{1/2} \langle w_2^*(t) w_2(t) \rangle^{1/2}),$$

where the asterisk indicates the complex conjugate. The complex correlation coefficient has a squared magnitude and phase (veering angle) which are given by,

$$|\rho|^2 = \frac{(\langle u_1 u_2 + v_1 v_2 \rangle^2 + \langle u_1 v_2 - u_2 v_1 \rangle^2)}{(\langle u_1^2 + v_1^2 \rangle \langle u_2^2 + v_2^2 \rangle)},$$

and,

$$\alpha_{\text{avg}} = \tan^{-1}(\langle u_1 v_2 - u_2 v_1 \rangle / \langle u_1 u_2 + v_1 v_2 \rangle).$$

Using method 1, maximum angular correlations were calculated with hourly data for 9 ship and moored ADCP bins that were vertically separated by less than 4 meters. These correlations suggest that the UOP ADCP data has a mean rotation of about 7.4 degrees (leg 1) and 8.7 degrees (leg 2) which give a mean rotation of 7 to 8 degrees east of north relative to the Moana Wave data (Tables E1 and E2.). The standard deviations are fairly large for both legs 1 and 2 but the means are consistent between both legs. Using the method from Kundu (1975), we find similar results although difference between the ADCP vertical average from leg 1 (-6.0 degrees) and leg 2 (-9.3 degrees) is larger than that of method 1, eventhough the standard deviations are smaller. This rotation is of the same magnitude but wrong sign to be considered to be due to an omission of the magnetic variation correction in the moored data. In addition to the relative rotation of the moored ADCP data there are also relative rotations the VMCM's relative to the ship data ranging from 1 to 10 degrees. Using the angular correlation information, the mean current vectors of the UOP mooring were rotated for the 31.5m, 39.5m VMCM's and the moored

ADCP data by 6° East of North, 10.5° East of North and 7.7° West of North respectively. The rotated UOP and Moana Wave mean profile results are shown in figure 1, and the difference profiles are shown in Fig. E2. The correction is more robust for the leg 2 meridional current due to the larger zonal currents which when erroneously rotated into the meridional direction have a large effect relative to leg 1 when the zonal currents were not as strong. In particular, note the correlation of the difference in the meridional current profile for leg 2 and the vertical structure of the zonal current. The differences are large where the zonal current is strong.

Review of Errors

Moored ADCP and VMCM current direction is measured using magnetic compasses, which have a directional accuracy of about 2-3 degrees in the mean (Pluddemann, personal communication). Freitag (1991) suggests that the uncertainty may be as large as 5 degrees. Schramm (1989) found substantial compass errors associated with magnetic compasses mounted on RDI ADCP's. The errors showed a dependence on temperature, pitch and roll, time, as well as the magnetic fields generated by the ADCP itself. In one case study of the temperature dependence of one instrument, the heading error was as large as 8 degrees when the instrumental temperature was at 3.0 degrees Celsius. In conclusion he states that in some cases compass errors may greatly exceed the accuracy specifications of +/- 2 degrees for the sensor but some of the errors can be reduced through careful calibration.

There are many sources of error, as listed below, associated with shipborne ADCP measurements.

1. - Short term uncertainty (ping to ping noise)
2. - Skew and noise bias due to tracking filter alignment.
3. - Transducer misalignment with gyrocompass and ship-transducer trim mismatch.
4. - Other gyrocompass error (Schuler oscillation, manufacture's speed corrections, etc.).
5. - GPS navigation error in shiptrack/ship velocity.

Short Term Uncertainty:

Short term uncertainty, defined as the error in single ping ADCP data, is dominated by random error (RDI Primer, 1989). For this reason, ADCP data is ensemble averaged over something like 2 minutes or more in order to reduce the ping-to-ping noise level. The uncertainty is a function of the hardware and software configuration and reduces as one over root N where N is the number of individual ping returns from a given depth bin acquired over some suitable period of time, like 2 to 5 minutes. The expected residual error for a given 30 ping ensemble for a 153 kHz ADCP operating with an 8 meter pulse length is about 2 cm/sec while for 100 pings we get 1.3 cm/sec. This result comes from the equation,

$$\sigma = (1.6 \text{ E}+5) / (FDN^{1/2})$$

where,

σ is the standard deviation (m/s)

F is the Frequency of the ADCP(Hz)

D is the depth cell size assumed to be the same as the transmit pulse length.

N is the number of pings averaged together to get the velocity estimate.

The dependence on D results from the inverse relationship between spectral broadening and the duration of transmit pulse. After averaging over something like an hour this random error should be negligible as compared to other sources of errors and in particular bias errors.

Skew and noise bias:

Chereskin et al [1989] investigated the effect of tracking filter alignment on skew and noise bias and found that even after employing a high quality tracking filter design, which in fact was adopted by RDI corporation, an error in velocity of about 1.7 cm/sec remains (0.7 cm/sec due to noise bias and 1.0 cm/sec due to tracking misposition) in the effective profiling range. The source of skew and noise bias is due to a combination of hardware and software considerations. The tracking filter skews the amplitude of the Doppler shifted return signal if the tracking filter is not centered on the return frequency. Further, tracking filter misalignment biases noise into the estimated return signal at the center frequency of the tracking filter. As the signal to noise (S/N) amplitude decreases, noise bias becomes more problematic. The effective profiling range varies with signal to noise amplitude and for a ship mounted ADCP covers roughly the upper 200m. The errors get larger as the S/N decreases with depth. They found a directional dependence that depended on the S/N and, in particular for the equatorial region where they compared the ADCP with moored VMCM's, found that the zonal component showed

larger noise bias than the meridional component at the depth of the EUC. Above this region, the noise and skew bias was considered to be about 1.7 cm/sec. It should be kept in mind that while model results contributed to their findings they quantified the magnitude of the errors by comparing ADCP results with moored VACM's, which have their own associated errors.

Transducer alignment:

Joyce [1989] provides a calibration approach to minimize errors associated with compass and transducer misalignment as well as ship hull/transducer trim mismatch. By a least squares minimization of the kinetic energy, an estimate of the relative rotation and amplitude correction can be made. They found that even after applying this correction an unexplained error of about 2.5 cm/sec for either velocity component remains for a ship traveling at about 10 knots. This error estimate scales directly with ship speed and is due mostly to compass drift on short time scales (e.g. Schuler oscillation) and other sources of drift on longer time scales (days to weeks). In a similar study, Pollard and Read [1989] suggested that the short term error in heading for a ship occupying a survey pattern that requires significant changes in heading every few hours is "perhaps about 0.5 degrees" which gives an error of 5 cm/sec in the athwartship currents for a ship steaming at 10 knots. This error may also show a particular preferred direction in the final geophysical coordinate current estimate depending on ship track, speed, and the properties of the ship's compass heading system.

Gyrocompass/GPS heading:

King and Cooper [1993] and, Saunders and King [1995] compare GPS heading with gyrocompass heading and use the former to correct the latter. Both approaches correct for ship transducer misalignment and hull/transducer misalignment as well as short and long term gyrocompass drift that may depend on ship heading, speed and latitude. The inherent assumption in both of these reports is that the GPS heading estimate shows no bias associated with ship track or speed so that all significant differences between GPS heading and gyrocompass heading are attributed to gyrocompass errors. Both studies were done using commercially available GPS heading systems manufactured by Ashtech, Inc. which uses an array of four antennas to compute heading by differential carrier phase measurements. King and Cooper [1993] note that the cruise occurred under calm seas so that the effect of pitch and roll on GPS accuracy was not tested under rough weather. Information regarding sea-state during the Saunders and King [1995] study was not immediately available. For both studies, the overall at sea GPS heading accuracy is about 0.2 degrees for periods exceeding a few minutes. By comparison the gyrocompass errors are on the order of a degree over a similar time scale and may amount to 3 degrees when the ship's heading changes considerably. The magnitude of the current error scales with ship speed and the sine of the angle such that a 0.2 degree (King and Cooper, 1993) error at 10 knots would amount to an error in the cross track current of about 1.7 cm/sec due to heading error. Saunders and King [1995] suggest that over a 4 hour average the errors may be a little as 1 cm/sec. At 2 knots, a common speed for the Moana Wave during the IOP, the error would be about 0.3 cm/sec for an angular

error of 0.2 degrees. It should be noted that Moana Wave had GPS heading data for leg 1 but not leg 2.

GPS navigation/shiptrack:

While the GPS heading data can greatly enhance the directional quality of the current data, the GPS ship velocity is still subject to Selective Availability (SA) errors that can be large. To reduce this error, when bottom tracking is not available, a water reference layer is used [Kosro, 1985] to smooth out the navigational noise. The smoothing layer is typically chosen over a reasonably significant number of bins, like from 5 to 20 ADCP bins for example, and filtered using a filter with a half-power point at something like 30 minutes. Pierce et al. [1995] found that a random error of about 6 cm/sec in a given 30 minute average still remains after applying the reference layer smoothing. This barotropic error can be reduced since it is a random error so that averaging over something like 20 days we get a residual error of about 0.3 cm/sec attributable to ship track uncertainty.

How do all these errors stack up? What is the total residual error that can be expected for the Moana Wave data in particular. For leg 1, using GPS heading and ship speed on the order of 1-2 knots, we get an error of about 0.3 cm/sec for heading error, 0.3 cm/sec or less for random ping to ping error, 0.3 cm/sec for random ship fix error, and a skew and noise bias error of about 1.7 cm/sec. So the total uncertainty for the leg 1 Moana Wave data is about 1.8 cm/sec when adding the errors in a sum of squares manner. For leg 2 GPS heading was not available so short term errors could be as large about 5 cm/sec (3.0 degree gyrocompass error at 2

knots) but long-term errors would be substantially less, on the order of 1 cm/sec (0.5 degrees at 2 knots). Additionally the GPS heading information from leg 1 was used to correct for the ship/transducer alignment so that the compass/transducer and ship hull/transducer trim correction for leg 2 was likely of high quality. The total error for leg 2 data is then about 2.0 cm/sec.

Previous ship/mooring comparison studies

Kosro [1985] compared moored VMCM and VACM current measurements with shipborne ADCP measurements in shallow coastal waters off Northern California for ship-mooring separations as small as 1 km. He found that strong correlations existed between moored and shipborne current estimates. The mean differences between moored and ADCP data was 0.6 cm/sec for the cross-shore current and up to 1.6 cm/sec for the alongshore component, with the ADCP having consistently higher values than the VMCM's. The standard deviation of differences, attributed largely to uncertainty in ship fixes and to short scale variability in the currents, was about 4.1-5.4 cm/sec for the cross-shore component and 3.6-4.4 cm/sec in alongshore component. The position fixes were from the LORAN navigational system which gave a position uncertainty of less than 50 meters which is comparable to today's GPS fixes. As previously mentioned, Chereskin et al. (1989) compared data from moored VACM's with shipborne ADCP at 0N, 110W for ship-mooring separations of about 10 km. They cite Halpern's (1987) estimate of VACM errors of about 1 cm/sec outside of high current variability regions. The estimated current

differences (Chereskin et al., 1989) outside the strong shear zones are small, on the order of 1-2 cm/sec for both velocity components.

A recent study by Lien et al. (1994) compares ADCP data from the R/V Wecoma, R/V Moana Wave and a PMEL mooring located at 0N, 140W which was equipped with an ADCP and VMCM's at 3, 10, 45 and 80 m as well as two VACM's at 120 and 200 m. The Wecoma and PMEL mooring comparisons are from November 4-21, 1991 and the Moana Wave/PMEL comparisons are from November 25 to December 12, 1991. The direction and magnitude differences found in the comparisons at 0N, 140W provide a benchmark for our current review of the UOP/Moana Wave comparisons. GPS position fixes were used to get ship velocity but GPS heading is not mentioned so it is assumed that it was not available. The ship-mooring separations were on the order of 3 miles with the Wecoma steaming at speeds of less than 2 knots and the Moana Wave steamed at about 1 knot unless it had to reposition which it did at nominally 5 knots. The mean current component differences between Wecoma and the mooring over the profiling range is about 1 cm/sec. A similar result is found for the Moana Wave and mooring comparisons. The current direction differences are on the order of 2-3 degrees or less for both comparisons.

Discussion

The mean differences between shipborne ADCP data and moored ADCP data seen in Lien et al's study is about 1.0 cm/sec over the effective profiling range. This result is consistent with the preceding review of shipborne and moored current measurement estimates. Given Lien et al's

results and the estimated error for shipborne ADCP data, the differences found between the UOP mooring and Moana Wave greater than about 2-3 degrees appear significant. This assertion is based on a mean zonal current of 20 cm/sec being rotated by 3.0 degrees which would give an apparent meridional current of just over 1.0 cm/sec. The results of leg 1 and leg 2 are comparable, being more conspicuous for leg 2 due to stronger zonal currents than in leg 1, suggesting that the estimated differences are robust. While the shipborne data is clearly not free from error, ADCP errors tend to be barotropic except for filter skew and bias and hence it seems reasonable to use the shipborne data as a standard to adjust the UOP mooring data. Usually mooring data is used as the reference by which to judge the quality of shipborne data but given that the directional differences are not consistent between each moored instrument and the shipborne ADCP data it would be impossible to rotate the ship data to agree with all of the moored data. Another alternative would be to rotate all of the instruments including the ship to find the smallest residual mean profile error for the smallest possible rotations. While this approach would give good agreement between the two platforms it is not clear that it would improve our estimates of the actual currents. Additionally the magnitude of the errors after rotating the UOP data are about 2 cm/sec or less which is consistent with the previous studies cited herein as well as the expected uncertainty in shipborne ADCP data as determined in this note.

Based on our findings we felt it necessary to rotate the WHOI UOP mooring current data for making our advection estimates for the COARE IOP. The rotations were 6 and 10 degrees East of North for the 31.5 and 39.5 m VMCM's respectively, and 8 degrees West of North for the ADCP data.

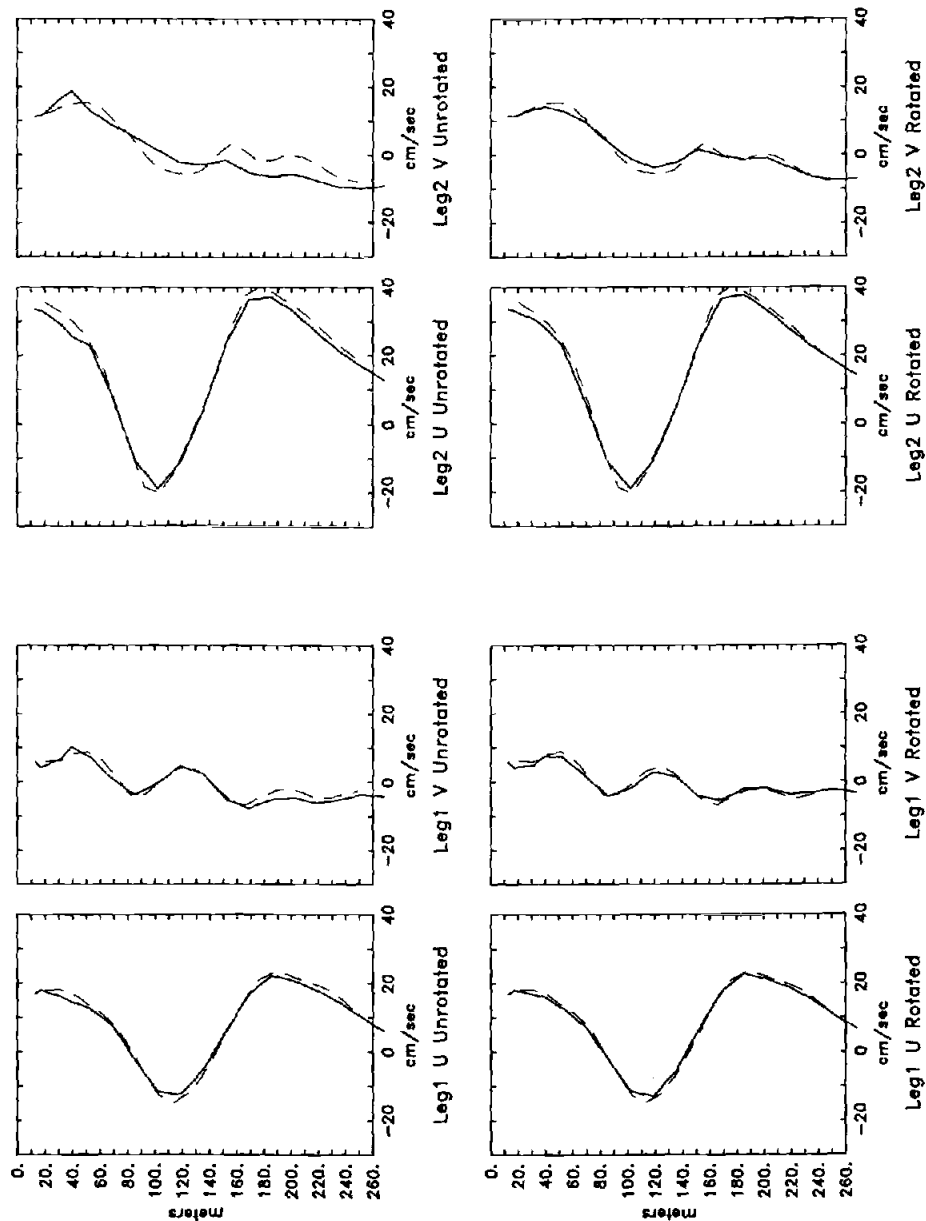


Figure E1. Profiles of average zonal (U) and meridional (V) currents from the UOP mooring (solid) and the R/V Moana Wave (dashed). Upper panels show directionally uncorrected profiles and lower panels show directionally corrected profiles. Note the improved agreement of the UOP and Moana Wave meridional profile for leg 2 after rotations were applied.

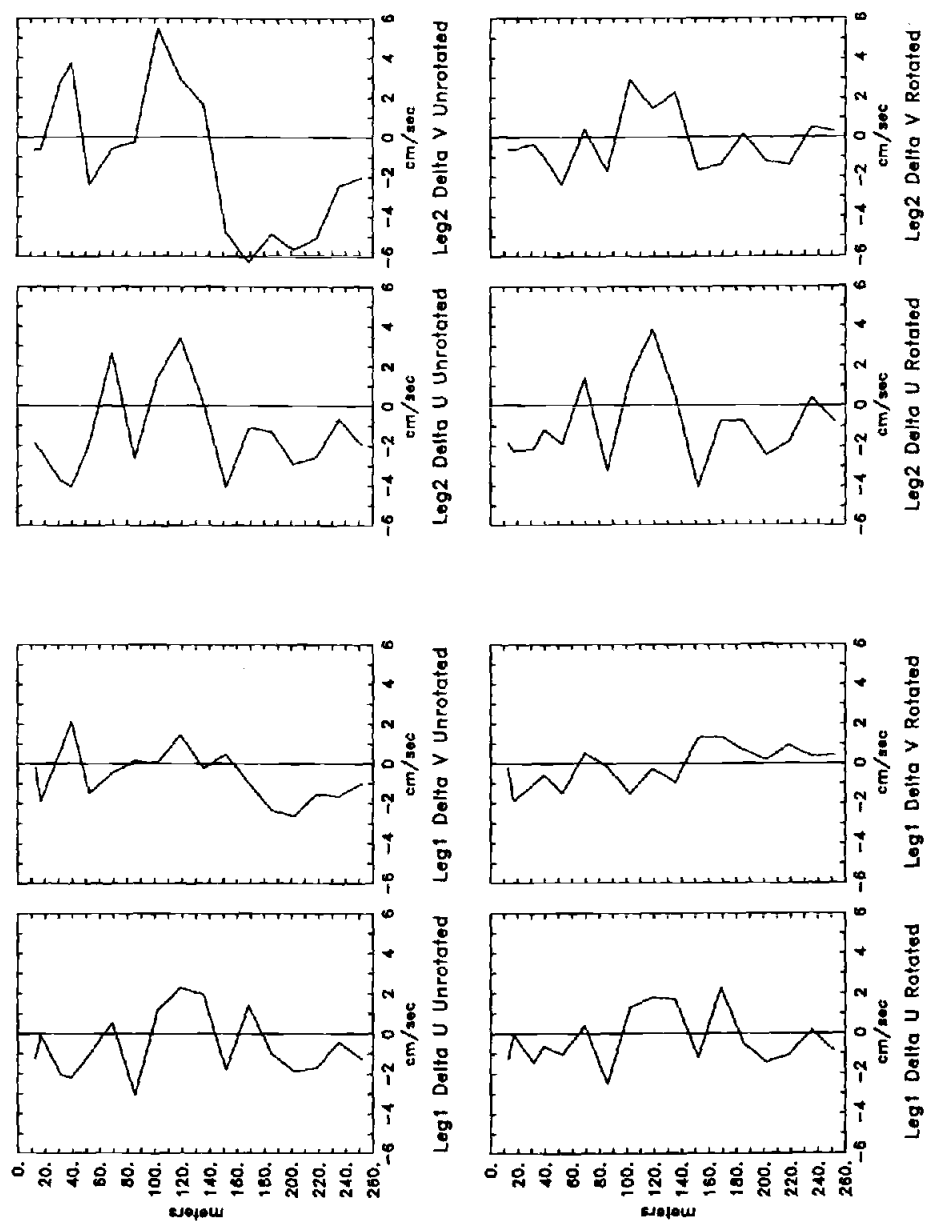


Figure E2. Profiles of average zonal differences (Delta U) and meridional differences (Delta V) for unrotated (upper panels) and rotated (lower panels) current vector components.

Table E1. Leg 1 moored ADCP/Ship ADCP Correlation.

Depth (m) UOP, MW	Max $\langle u_{rot} u_{mw} \rangle$	$\theta_{\langle uu \rangle}$	Max $\langle v_{rot} v_{mw} \rangle$	$\theta_{\langle vv \rangle}$	$\theta_{avg} =$ $(\theta_{\langle uu \rangle} + \theta_{\langle vv \rangle})/2$	$ \rho ^2$	α_{avg}
69.1, 72.4	0.84	-2	0.85	-5	-3.5	0.75	-2.5
102.3, 103.5	0.84	-3	0.78	-17	-10	0.77	-4.9
135.4, 134.5	0.75	-3	0.79	-6	-4.5	0.66	-5.1
152.0, 155.3	0.77	-7	0.82	-5	-6	0.71	-5.1
185.2, 186.4	0.86	-10	0.56	-6	-8	0.87	-7.6
201.8, 196.8	0.82	-12	0.64	-9	-10.5	0.87	-8.6
218.4, 217.5	0.84	-8	0.74	-9	-8.5	0.87	-6.9
235.0, 238.3	0.86	-9	0.72	-7	-8	0.84	-7.1
251.6, 248.6	0.85	-9	0.70	-6	-7.5	0.79	-6.5
ADCP _{avg}		-7.0		-7.8	-7.4		-6.0
ADCP _{std}		3.5		3.8	2.3		1.7

Table E2. Leg 2 moored ADCP/Ship ADCP Correlation.

Depth (m) UOP, MW	Max $\langle u_{rot} u_{mw} \rangle$	$\theta_{\langle uu \rangle}$	Max $\langle v_{rot} v_{mw} \rangle$	$\theta_{\langle vv \rangle}$	$\theta_{avg} =$ $(\theta_{\langle uu \rangle} + \theta_{\langle vv \rangle})/2$	$ \rho ^2$	α_{avg}
69.1, 72.4	0.91	-9	0.92	-14	-11.5	0.85	-11.5
102.3, 103.5	0.93	-8	0.92	-9	-8.5	0.91	-11.3
135.4, 134.5	0.93	-9	0.89	-7	-8	0.82	-6.6
152.0, 155.3	0.94	-12	0.84	-14	-13	0.92	-10.8
185.2, 186.4	0.92	-9	0.86	-5	-7	0.96	-7.6
201.8, 196.8	0.90	-4	0.83	-7	-5.5	0.95	-9.2
218.4, 217.5	0.88	-12	0.81	-4	-8	0.94	-10.8
235.0, 238.3	0.88	-7	0.80	-9	-8	0.92	-6.9
251.6, 248.6	0.86	-7	0.79	-10	-8.5	0.91	-8.9
ADCP _{avg}		-8.6		-8.8	-8.7		-9.3
ADCP _{std}		2.5		3.5	2.3		1.8

Table E3. Leg 1 moored VMCM/Ship ADCP Correlation.

Depth (m) UOP, MW	Max $\langle u_{rot} u_{mw} \rangle$	$\theta_{\langle uu \rangle}$	Max $\langle v_{rot} v_{mw} \rangle$	$\theta_{\langle vv \rangle}$	$\theta_{avg} =$ $(\theta_{\langle uu \rangle} + \theta_{\langle vv \rangle})/2$	$ \rho ^2$	α_{avg}
13.0, 20.6	0.95	1	0.97	-3	-1	0.95	-0.3
17.0, 20.6	0.95	2	0.97	-5	-1.5	0.95	-2.3
31.5, 30.9	0.96	6	0.97	6	6	0.95	6.6
39.5, 41.3	0.95	12	0.97	11	11.5	0.95	11.8
52.5, 51.7	0.90	3	0.95	-7	-2	0.91	-1.7

Table E4. Leg 2 moored VMCM/Ship ADCP Correlation.

Depth (m) UOP, MW	Max $\langle u_{rot} u_{mw} \rangle$	$\theta_{\langle uu \rangle}$	Max $\langle v_{rot} v_{mw} \rangle$	$\theta_{\langle vv \rangle}$	$\theta_{avg} =$ $(\theta_{\langle uu \rangle} + \theta_{\langle vv \rangle})/2$	$ \rho ^2$	α_{avg}
13.0, 20.6	0.93	0	0.90	-5	-2.5	0.95	-1.3
17.0, 20.6	0.93	-1	0.90	-6	-3.5	0.95	-1.1
31.5, 30.9	0.93	6	0.92	7	6.5	0.96	6.8
39.5, 41.3	0.93	6	0.88	13	9.5	0.93	7.9
52.5, 51.7	0.94	-2	0.91	1	-0.5	0.93	-2.7